RUHR-UNIVERSITÄT BOCHUM

Qian Gu

On the effects of grain shape, gradation, fabric and stress state on the small-strain stiffness of granular soils

Bochum 2025

Heft 86

Schriftenreihe des Lehrstuhls für
Bodenmechanik, Grundbau und Umweltgeotechnik

Herausgeber: Torsten Wichtmann

ISSN 2699-1020

On the small-strain stiffness of granular soils

Qian Gu

86

ISSN 2699-1020

Ruhr-Universität Bochum
Schriftenreihe Bodenmechanik, Grundbau und Umweltgeotechnik
Heft 86

Herausgeber:
Prof. Dr.-Ing. habil. Torsten Wichtmann
Ruhr-Universität Bochum
Fakultät für Bau- und Umweltingenieurwissenschaften
Lehrstuhl für Bodenmechanik, Grundbau und Umweltgeotechnik
44801 Bochum
Telefon: 0234/ 3226135
Internet: www.bgu.ruhr-uni-bochum.de

ISSN 2699-1020

On the effects of grain shape, gradation, fabric and stress state on the small-strain stiffness of granular soils

Dissertation

as a requirement of the degree of
Doktor-Ingenieur (Dr.-Ing.)

at the Faculty of
Civil and Environmental Engineering
Ruhr-Universität Bochum

submitted by
Qian Gu
from Sichuan, China

Reviewers
Prof. Dr.-Ing. habil. Torsten Wichtmann
Prof. Dr.-Ing. Jan Laue
Assist. Prof. Dr.-Ing. Felipe Prada

Bochum, August 2025

This work is dedicated to my beloved grandparents and parents

Preface of the Editor

The stiffness of soil depends on the magnitude of strain. At very small strains the soil behaviour is elastic and the stiffness takes its maximum value. At intermediate strain levels nonlinear elastic behaviour is observed accompanied by a gradual decrease in stiffness, followed by a pronounced reduction of stiffness and plastic deformations at larger strain levels. Advanced constitutive models for soils take into account this strain-dependent stiffness, in particular the maximum elastic stiffness at very small strains, in order to allow reliable predictions of deformations of geotechnical structures. Furthermore, information on the stiffness at small to intermediate strain levels is needed for analyses in the fields of soil dynamics and geotechnical earthquake engineering, e.g. in the design of machine foundations or for studies of wave propagation problems.

The doctoral thesis of Qian Gu concentrates on the elastic stiffness at very small strains. This small-strain stiffness depends on several parameters like soil density, fabric, stress state, loading history and soil type. The most widely used methods to investigate the small-strain stiffness in the laboratory are resonant column tests and wave velocity measurements using piezoelectric elements. In most previous studies, however, these measurements were restricted to the shear wave velocity propagating in the vertical direction, or the corresponding shear modulus. The anisotropy of the small-strain stiffness and its dependence on the various parameters has been rarely studied so far.

Qian Gu has investigated the small-strain stiffness of granular soils with a special focus on the influence of various factors on its anisotropy. A triaxial device was extended by piezoelectric elements. Two couples of bender and compression elements were incorporated into the end plates, allowing the measurement of shear and compression waves in the vertical direction. Two further pairs of bender elements could be mounted on the sides of the specimen, enabling measurements of shear waves with different polarization in the horizontal direction, as well as along inclined paths. The extended device was carefully calibrated and validated.

In his experiments Qian Gu has investigated the influences of the initial fabric, generated by two different sample preparation methods (air pluviation or moist tamping), the isotropic or anisotropic stress state, the previous loading history (drained or undrained triaxial loading paths), grain shape and grain size distribution on the small-strain stiffness of granular soils and its anisotropy. While the effects of fabric and stress state were

investigated on Hostun sand, three materials with significantly different grain shape were prepared each with two different uniformity coefficients in order to study the influence of the particle characteristics. The tested materials were round glass beads, subangular natural Rhine sand and angular crushed glass. The results show that samples prepared by moist tamping show a higher stiffness anisotropy than samples prepared by air pluviation. The small-strain stiffness was found rather isotropic under isotropic stress conditions, while an anisotropy was induced by anisotropic loading. This stress-induced anisotropy was more pronounced under drained than under undrained triaxial compression loading. Furthermore, the grain shape has a significant influence on the development of stiffness anisotropy under deviatoric stress paths, with higher anisotropy observed for the materials with rounder particles. For constant void ratios and stress levels, the more angular materials showed higher small-strain stiffness compared to the round glass beads in all measured directions. Additionally, the more well graded mixtures exhibited lower shear moduli in all directions, independently of the grain shape. Qian Gu discusses his experimental results in the context of extended empirical equations for the small-strain stiffness.

The experimental data set gathered in the framework of the doctoral research of Qian Gu may be used to further develop and calibrate formulations for the anisotropic small-strain stiffness in advanced constitutive models for granular soils. Furthermore, the results may be also useful for comparative numerical studies with the discrete element method to shed some more light on the micromechanics behind the experimental observations.

Bochum, August 2025 Prof. Dr.-Ing. habil. Torsten Wichtmann

Acknowledgements

This research was carried out in the Chair of Soil Mechanics, Foundation Engineering and Environmental Geotechnics, Ruhr-Universität Bochum. First and foremost, I would like to thank my supervisor Prof. Torsten Wichtmann who kindly accepted me under his supervision to continue my study in the chair after Prof. Schanz's life was taken prematurely, and gave me a lot of scientific support during my research work.

I would like to gratefully thank Prof. Tom Schanz who provided me the chance to start my research work in RUB. The memory of him will remain with me always.

I would like to gratefully thank Prof. Jan Laue (Lulea University of Technology, Sweden) and Prof. Felipe Prada (University Aarhus, Denmark) for acting as reviewers of my thesis. Their critical and constructive comments significantly improved this work.

I would like to express my sincerest gratitude to Dr. Meisam Goudarzy and Dr. Diethard König for their assistance and numerous constructive suggestions during my research work, which has guided me through the long academic puzzlement to a sudden enlightenment.

I would like to thank the laboratory technicians, Mr. Michael Skubisch, Mr. Joachim Blazytko, and Mr. Werner Müller who helped with the devices when I performed the tests in the laboratory. I also thank the other colleagues in RUB who provided me so much help in both my professional and personal life.

Last, but not least, I would like to thank my parents and friends for their continuous support and motivation in my journey from a Master to a Doctor.

Bochum, August 2025 Qian Gu

Abstract

The behavior of soils, in particular stiffness, exhibits a significant dependency on the strain level. At the small strain level ($< 10^{-5}$), soils display elastic behavior, taking maximum stiffness values. This maximum elastic stiffness, e.g., maximum shear modulus $G_{\max}$, is crucial in several geotechnical engineering problems and a key parameter in diverse advanced constitutive models, e.g. the Hardening Soil Small Strain model that is frequently adopted by practitioners in finite element simulations for soil-structure interaction problems. Over the past few decades, numerous studies have focused on evaluating the impact of various factors on the maximum elastic stiffness, primarily $G_{\max}$, leading to the development and continuous refinement of empirical equations proposed to predict $G_{\max}$. However, accurately quantifying the combined effects of initial soil fabric, particle shape, grain size distribution curve and isotropic or anisotropic stress state on the elastic stiffness matrix of granular soils remains a complex challenge in this field. Addressing this challenge is the primary goal of this doctoral thesis.

The measurement of the elastic characteristics of soils at very small strain levels ($< 10^{-6}$) requires methods that minimally disturb the soil, preserving its 'constant fabric' properties during experiments. Geophysical laboratory techniques, utilizing piezoelectric elements to propagate low amplitude waves, provide a simple option for assessing the elastic stiffness ($G_{\max}$ and $E_{\max}$) of soils at small strains. This study incorporated this technique into a triaxial apparatus to systematically investigate the outlined objectives. The modified triaxial apparatus included both multidirectional bender and compression elements for measuring shear and compression wave velocities in various configurations to determine shear moduli (G_{vh}, G_{hh}, and G_{hv}) in different directions, as well as the elastic modulus (E_v) in the vertical direction of the specimen. Extensive efforts were conducted to calibrate and validate the modified device using aluminum and plastic dummies, and comparative experiments on sands. Afterwards, the modified device was used to assess the impact of the initial fabric (by adopting different sample preparation methods), isotropic and anisotropic stress states, particle shape and grain size distribution curve on the small-strain stiffness under both drained and undrained conditions.

As it was apparent from the experimental results, the method of sample preparation significantly affected the initial fabric of the specimens. The analysis of results indicated that the inherent stiffness anisotropy in samples prepared using the air pluviation method was less than that in samples prepared using the moist tamping method. For the specimens

subjected to anisotropic stress, it was found that $G_{vh} \neq G_{hh}$ and the increase in the stress ratio led to an increase in the stiffness anisotropy. The results demonstrated the significant effect of the mean effective stress and deviatoric stress on maximum shear modulus. Based on the experimental data, the combined influence of grain shape and grading on G_{ij}, $E_{\max}$, and Poisson's ratio (ν) was also analyzed. The results showed that in the sand with medium density under anisotropic loading, the stiffness of samples with rounded particles was higher than that of samples with angular particles. The analysis of the experimental results also revealed that Poisson's ratio increased slightly with increasing void ratio, while the effect of particle shape on Poisson's ratio was negligible. As was obvious from the experimental results, the maximum G_{ij} and $E_{\max}$ were generally larger for uniformly graded sands ($C_u = 1.25$) compared to well-graded materials ($C_u = 5$).

Additionally, experimental data were adopted to develop empirical equations in the space of p', q, and e to estimate $G_{\max}$, $E_{\max}$, and Poisson's ratio (ν). The constants of the developed equations were also correlated to particle shape descriptors. The regression analysis further revealed that the exponent of the term considering p' in the equations is larger than the exponent of q, confirming the dominant effect of mean effective stress on maximum moduli compared to deviatoric stress.

Zusammenfassung

Das Verhalten von Böden, insbesondere die Steifigkeit, hängt in hohem Maße von der Größe der Dehnung ab. Bei geringen Dehnungen ($< 10^{-5}$) verhalten sich Böden elastisch und die Steifigkeit ist maximal. Diese maximale elastische Steifigkeit, z. B. der maximale Schubmodul $G_{\max}$, ist für viele geotechnische Problemstellungen von Bedeutung und eine wichtige Komponente verschiedener fortgeschrittener Stoffmodelle für Böden. Sie wird beispielsweise im "Hardening Soil Small Strain" Modell berücksichtigt, das in der Praxis häufig in Finite-Elemente-Simulationen für Problemstellungen mit Boden-Bauwerk-Interaktion eingesetzt wird. In den letzten Jahrzehnten haben sich zahlreiche Studien mit der messtechnischen Erfassung und Bewertung des Einflusses verschiedener Faktoren auf die maximale elastische Steifigkeit - vor allem $G_{\max}$ - befasst, was zur Entwicklung und kontinuierlichen Verbesserung empirischer Gleichungen zur Vorhersage von $G_{\max}$ geführt hat. Die Quantifizierung der kombinierten Auswirkungen der Struktur des Bodens, der Kornform, der Korngrößenverteilungskurve sowie des isotropen oder anisotropen Spannungszustands auf die elastische Steifigkeitsmatrix von granularen Böden stellt jedoch nach wie vor eine Herausforderung dar. Die Quantifizierung dieser gekoppelten Einflüsse auf Basis detaillierter experimenteller Untersuchungen ist daher das Hauptziel dieser Doktorarbeit.

Die Messung der elastischen Eigenschaften von Böden bei sehr geringen Dehnungen ($< 10^{-6}$) erfordert Methoden, die den Boden nur minimal stören und seine Struktur während der Versuche bewahren. Geophysikalische Verfahren, bei denen piezoelektrische Elemente zur Messung der Ausbreitung von Wellen mit geringer Amplitude verwendet werden, bieten eine einfache Möglichkeit zur laborativen Ermittlung der elastischen Steifigkeit ($G_{\max}$ und $E_{\max}$) von Böden bei geringen Dehnungen. In der vorliegenden Dissertation wurde dieses Messverfahren in ein Triaxialversuchsgerät integriert. Das modifizierte Triaxialgerät wurde mit multidirektionalen Biegeelementen (engl. Bender Elements) sowie Kompressionselementen ausgestattet, um Scher- und Kompressionswellengeschwindigkeiten in verschiedenen Konfigurationen zu messen. Aus den Wellengeschwindigkeiten wurden die Schubmoduln (G_{vh}, G_{hh} und G_{hv}) in verschiedenen Richtungen sowie der Elastizitätsmodul (E_v) in der vertikalen Richtung der Probe berechnet. Das modifizierte Gerät wurde unter Verwendung von Aluminium- und Kunststoffdummys sowie durch Vergleichsexperimente mit Sand umfangreich kalibriert und validiert. Anschließend wurde das Gerät verwendet, um den Einfluss der Anfangsstruktur (durch Anwendung verschiedener Probenpräpara-

tionsmethoden), isotroper und anisotroper Spannungszustände, der Kornform sowie der Korngrößenverteilungskurve auf die Steifigkeit bei kleinen Dehnungen unter dränierten und undränierten Bedingungen zu untersuchen.

Die Versuchsergebnisse zeigen, dass die Art der Probenvorbereitung einen erheblichen Einfluss auf die Anfangsstruktur der Proben hat. Bei Proben, die durch trockenes Rieseln hergestellt wurden, war die inhärente Anisotropie der Steifigkeit geringer als bei Proben, die durch feuchtes Einstampfen präpariert wurden. Bei Proben, die einer anisotropen Spannung ausgesetzt waren, wurde festgestellt, dass $G_{vh} \neq G_{hh}$ gilt und eine Erhöhung des Spannungsverhältnisses zu einer Zunahme der Anisotropie der Steifigkeit führte. Die Ergebnisse demonstrieren zudem den signifikanten Einfluss der mittleren effektiven Spannung und der Deviatorspannung auf den maximalen Schubmodul. Desweiteren wurde auf der Grundlage der experimentellen Daten der kombinierte Einfluss von Kornform und Korngrößenverteilung auf die Steifigkeiten G_{ij} und $E_{\max}$ sowie die Querdehnzahl (ν) analysiert. Bei mitteldicht gelagertem Sand unter anisotroper Belastung wurde für Proben mit abgerundeten Partikeln eine höhere Steifigkeit beobachtet als für solche mit eckigen Partikeln. Die Analyse der experimentellen Ergebnisse ergab auch, dass die Querdehnzahl mit zunehmendem Porenanteil leicht anstieg, während der Einfluss der Kornform auf die Querdehnzahl vernachlässigbar klein war. Die maximalen Werte von G_{ij} und $E_{\max}$ waren bei gleichförmigen Sanden ($C_u = 1,25$) zudem generell größer als bei ungleichförmigen Materialien ($C_u = 5$).

Die experimentellen Daten wurden weiterhin verwendet, um empirische Gleichungen mit den Variablen p', q und e zu entwickeln, um $G_{\max}$, $E_{\max}$ und die Querdehnzahl (ν) zu prognostizieren. Die Konstanten der entwickelten Gleichungen wurden mit Parametern korreliert, die die Kornform beschreiben. Eine Regressionsanalyse ergab ferner, dass der Exponent des Terms, der p' in den Gleichungen berücksichtigt, größer ist als der Exponent von q, was den dominanten Einfluss der mittleren effektiven Spannung auf die maximalen Moduln im Vergleich zur Deviatorspannung demonstriert.

Contents

Preface of the Editor i

Acknowledgements iii

Abstract v

Zusammenfassung vii

1 Introduction 1

1.1 Strain-dependent stiffness in geotechnical engineering 1

1.2 Cross-anisotropic small-strain stiffness 3

1.3 Measurement of small-strain stiffness with piezoelectric elements 4

1.4 Objectives of the research 5

1.5 Organization of the thesis 6

2 Literature review 9

2.1 Empirical equations for the elastic stiffness 9

2.2 Influence of void ratio 10

2.3 Influence of sample preparation method 14

2.4 Influence of boundary conditions 19

2.4.1 Isotropic stress state 20

2.4.2 Anisotropic stress state 21

2.4.3 Saturation 24

2.5 Influence of grain size distribution and particle characteristics 26

2.5.1 Mineralogy of particles 26

2.5.2 Shape of particles 26

2.5.3 Particles size and gradation 29

3 Materials, experimental methods and testing program 33

3.1 Adopted materials 33

3.1.1 Hostun sand (Hs) 34

3.1.2 Round Glass beads (Gr) . . . 36
3.1.3 Crushed glass (Gc) . . . 37
3.1.4 Rhine sand (Rs) . . . 38
3.1.5 Summary of the adopted materials . . . 39
3.2 Test devices adopted . . . 40
3.2.1 Triaxial device . . . 41
3.2.2 Measuring system using piezoelectric element technique . . . 44
3.2.2.1 Manufacturing of bender elements . . . 44
3.2.2.2 Measuring system . . . 46
3.2.2.3 Determination of the delay time t_{delay} . . . 47
3.2.2.4 Signal analysis . . . 49
3.2.2.5 Modification of the triaxial device for wave velocity measurements . . . 50
3.3 Sample preparation . . . 52
3.3.1 Air pluviation (AP) method . . . 54
3.3.2 Moist tamping (MT) method . . . 54
3.4 Testing procedure . . . 54
3.5 Testing program . . . 55
3.5.1 Experiments on the effect of the sample preparation method . . . 55
3.5.2 Experiments on the effect of stress-induced anisotropy . . . 56
3.5.3 Experiments on the effect of particle shape . . . 56

4 Experimental results 61
4.1 Effect of sample preparation method . . . 61
4.1.1 Effect of sample preparation method at the small-strain level . . . 62
4.1.2 Effect of sample preparation method at the large-strain level . . . 66
4.2 Effect of stress state . . . 70
4.2.1 Isotropic stress state . . . 71
4.2.2 Anisotropic stress state . . . 72
4.3 Effect of particle shape and gradation . . . 81
4.3.1 Shape of particles . . . 81
4.3.1.1 Influence on small-strain shear modulus G_{max} . . . 81
4.3.1.2 Influence on small-strain Young's modulus E_{max} . . . 90
4.3.1.3 Influence on Poisson's ratio ν . . . 93
4.3.2 Grain size distribution . . . 94

5 Empirical equations **99**
5.1 Effect of sample preparation method 100
5.1.1 Void ratio function 100
5.1.2 Stress function 100
5.2 Effect of stress state 104
5.2.1 Isotropic stress states 105
5.2.2 Anisotropic stress states 106
5.3 Effect of grain shape and gradation 109

6 Conclusions and outlook **115**
6.1 Conclusions 115
6.1.1 Instrumentation of triaxial device 115
6.1.2 Effect of sample preparation method 117
6.1.3 Effect of anisotropic stress states 118
6.1.4 Combined effect of grain shape and grading 119
6.2 Future research 120

Bibliography **123**

1 Introduction

1.1 Strain-dependent stiffness in geotechnical engineering

The stiffness of soil is a key parameter in constitutive models used in both numerical simulations and analytical approaches to assess the deformations of soils and geotechnical structures subjected to various types of loadings (e.g., static, cyclic, and dynamic). The Young's modulus, E, defines stiffness under normal loading, while the shear modulus, G, describes stiffness under shear loading. The shear modulus is the primary soil property utilized in seismic analysis to predict the response to dynamic loading.

It is well known, that the soil behaviour, in particular stiffness, depends on the strain level. The relationship between strain and stiffness reflects the complex nature of soil behavior under different loading conditions (Atkinson, 2000). Under cyclic loading, the secant shear modulus G and the secant Young's modulus E derived from the stress-strain hysteresis degrade nonlinearly with increasing strain amplitude. An analogous stiffness degradation is also observed for monotonic loading processes. The stiffness at a certain strain level is often normalized to the corresponding values at very small strains, termed $G_{\max}$ and $E_{\max}$, expressed as a ratio, $G/G_{\max}$ or $E/E_{\max}$, providing a dimensionless curve in dependence of strain (Figure 1.1).

As shown in Figure 1.1 (Wong et al., 2021), the normalized modulus reduction curve, $G/G_{\max}(\gamma)$ in this figure, can be divided into three main sections, separated by threshold shear strain values:

1. Very small strains ($\gamma < 0.001\%$), where the shear modulus is generally constant and at its maximum.
2. Small to medium strains ($0.001\% < \gamma < 0.1\%$), where the shear modulus begins to degrade in a nonlinear fashion.

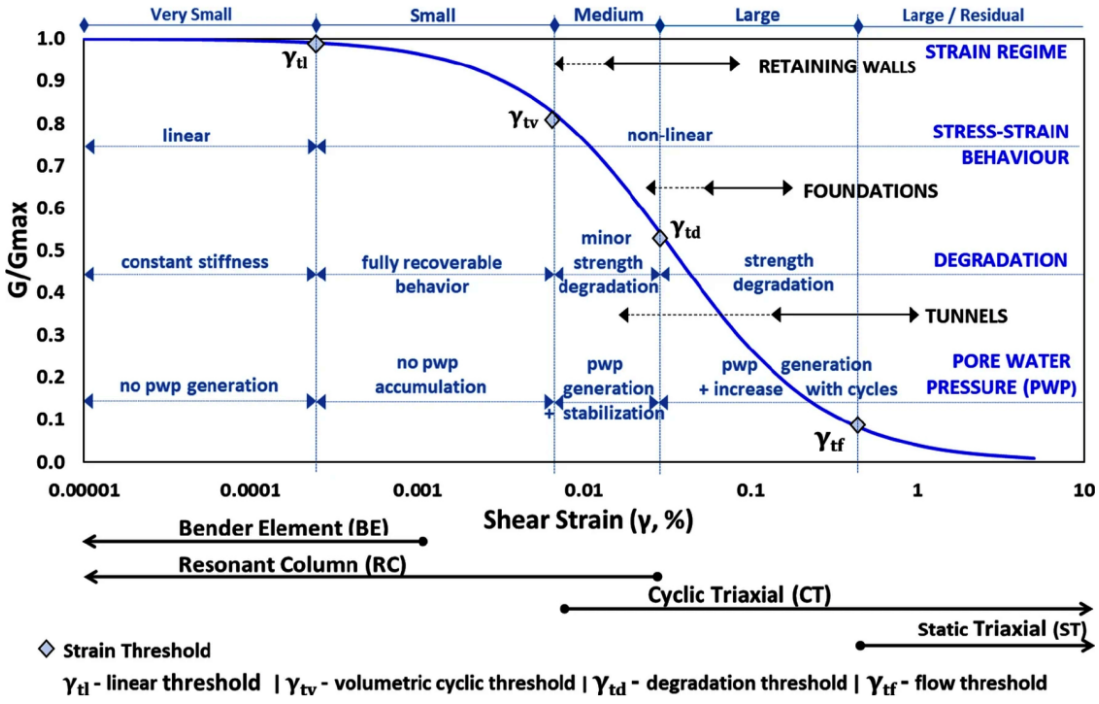

Figure 1.1: Schematic sketch of normalized shear modulus $G/G_{\max}$ versus shear strain γ (after Wong et al. 2021).

3. Large strains ($\gamma > 0.1\%$), where stiffness and strength degradation is non-recoverable, and the soil eventually reaches failure.

The main focus of the research described in this thesis is on the elastic characteristics of granular soils at very small strains. In this strain range, soil behavior is fully recoverable and the shear and Young's moduli take their maximum values, commonly denoted as $G_{\max}$ or G_0 and $E_{\max}$ or E_0.

The small-strain stiffness is a key parameter in soil-structure interaction models, seismic response analysis, and ground vibration assessments. The importance of $G_{\max}$ stems from its role in ensuring that many geotechnical structures, such as foundations, retaining walls, and embankments, operate predominantly within the small-strain regime, where soil maintains its highest stiffness and thus offers the greatest resistance to deformation. Therefore, accurately determining and estimating elastic stiffness in the small-strain range is essential for reliable predictions of soil behavior in both analytical approaches or numerical simulations using advanced constitutive models, e.g. the Hardening Soil Small Strain model.

1.2 Cross-anisotropic small-strain stiffness

Equation 1.1 shows the general form of the elastic constitutive model, where σ_i and ε_j are the stress and strain vector (or tensor), respectively, and E_{ij} is the elastic stiffness matrix (or tensor).

$$\sigma_i = E_{ij}\varepsilon_j \tag{1.1}$$

In homogeneous and isotropic materials, stiffness is identical in all directions. However, this is commonly not the case in natural soils. The fabric of soils, formed by the arrangement of particles during deposition in the field or by preparation in the laboratory and further changed during loading, can lead to a significant anisotropy of soil behaviour. Several previous studies came to the conclusion that cross-anisotropy should be considered in the analysis of experimental data and geotechnical design (Lee & Rowe, 1989; Stark & Eid, 1998; Yimsiri & Soga, 2002; Abdoun & Dobry, 2002; Mitchell & Soga, 2005). In case of cross-anisotropy it is assumed that the soil behaviour is the same in both horizontal directions, but differs in the vertical direction.

The constitutive relationship in case of a cross-anisotropic elastic stiffness is given in Equation 1.2.

$$\begin{pmatrix} \Delta\sigma'_{xx} \\ \Delta\sigma'_{yy} \\ \Delta\sigma'_{zz} \\ \Delta\tau'_{xy} \\ \Delta\tau'_{yz} \\ \Delta\tau'_{zx} \end{pmatrix} = \begin{pmatrix} E_h & -\frac{E_h}{\nu_{hh}} & -\frac{E_v}{\nu_{vh}} & 0 & 0 & 0 \\ -\frac{E_h}{\nu_{hh}} & E_h & -\frac{E_v}{\nu_{vh}} & 0 & 0 & 0 \\ -\frac{E_h}{\nu_{hv}} & -\frac{E_h}{\nu_{hv}} & E_v & 0 & 0 & 0 \\ 0 & 0 & 0 & G_{hh} & 0 & 0 \\ 0 & 0 & 0 & 0 & G_{hv} & 0 \\ 0 & 0 & 0 & 0 & 0 & G_{vh} \end{pmatrix} \begin{pmatrix} \Delta\varepsilon_{xx} \\ \Delta\varepsilon_{yy} \\ \Delta\varepsilon_{zz} \\ \Delta\varepsilon_{xy} \\ \Delta\varepsilon_{yz} \\ \Delta\varepsilon_{zx} \end{pmatrix} \tag{1.2}$$

Therein, E_v and E_h represent the Young's moduli in the vertical and horizontal directions, respectively, while G_{vh}, G_{hv}, and G_{hh} represent the shear moduli in different planes. ν_{vh}, ν_{hv}, and ν_{hh} are Poisson's ratios. In this context, the subscripts h and v represent the horizontal and vertical directions, respectively. Figure 1.2 provides a schematic representation of the shear moduli in different directions, along with the corresponding coordinate

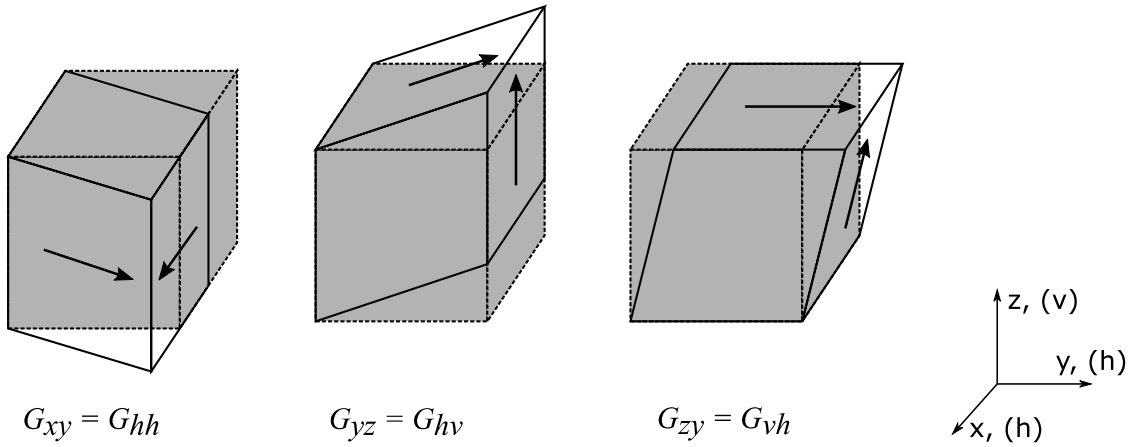

Figure 1.2: Schematic sketches for shear moduli in different directions with a corresponding coordinate system.

system, where the z-axis represents the vertical direction, and the x- and y-axes represent the horizontal directions. The stiffness matrix considering cross-anisotropy is fully defined by five independent parameters (Love, 1944). Due to the symmetry of the compliance matrix and the isotropy in the horizontal plane, $\frac{E_v}{\nu_{vh}} = \frac{E_h}{\nu_{hv}}$ and $G_{hh} = \frac{E_h}{2(1+\nu_{hh})}$ and $G_{vh} = G_{hv}$ hold. For homogeneous and isotropic materials, the moduli and Poisson's ratios are considered to be identical in the different directions, i.e. $E_v = E_h = E$, $G_{vh} = G_{hv} = G_{hh} = G$ and $\nu_{vh} = \nu_{hv} = \nu_{hh} = \nu$.

1.3 Measurement of small-strain stiffness with piezoelectric elements

The stiffness of a material at very small strains (less than 10^{-5}) can be measured during conventional laboratory tests using piezoelectric elements. Piezoelectric elements generate a deformation if an electrical signal is applied, or produce an electrical signal in case of mechanical stressing. Depending on the type of the piezoelectric element, shear (S) or compression (P) waves are emitted and received. The most popular elements for the measurement of shear waves are the bender elements, which penetrate into the soil samples and bend when an electrical signal is applied. The use of bender elements in geotechnics began in the late 1970s with Shirley & Hampton (1978), and became popular later with the work of Dyvik & Madshus (1985), who demonstrated a very good agreement between results obtained from bender elements and resonant-column tests. Nowadays,

this technique is widely used in laboratories to generate elastic waves with small strain amplitudes in soil samples. The relatively small piezoelectric elements can be installed in various devices, such as triaxial devices (Kuwano, 1999; Fioravante, 2000; Ezaoui & Di Benedetto, 2009; Ng et al., 2009), oedometer devices (Zeng & Ni, 1999; Zhao et al., 2020), calibration chambers (Lo Presti & O'Neill, 1991; Stokoe et al., 1991), and resonant column devices (Goudarzy et al., 2016a). By measuring waves in different directions, the piezoelectric element technique can be used to investigate the anisotropic features of small-strain stiffness.

From the measured compression wave velocity, v_p, and shear wave velocity, v_s, the small-strain values of the constrained modulus, $M_{\max}$, Young's modulus, $E_{\max}$, and shear modulus, $G_{\max}$, can be calculated taking into account soil density, ρ, as shown in Equations 1.3, 1.4, and 1.5.

$$M_{\max} = \rho \, v_p^2 \tag{1.3}$$

$$G_{\max} = \rho \, v_s^2 \tag{1.4}$$

$$E_{\max} = G_{\max} \, \frac{3M_{\max} - 4G_{\max}}{M_{\max} - G_{\max}} = \rho \, v_s^2 \, \left(\frac{3v_p^2 - 4v_s^2}{v_p^2 - v_s^2} \right) \tag{1.5}$$

1.4 Objectives of the research

Numerous experimental studies have been conducted in the past decades to evaluate the effect of various parameters on elastic stiffness using the piezoelectric element technique. Most studies have considered stiffness in a single direction, such as G_{vh}, with only a few evaluating the cross-anisotropy in soil specimens. Furthermore, empirical equations have been developed to estimate maximum stiffness, with some studies arguing that the effect of stress anisotropy on elastic stiffness is negligible. The experiments of Roesler (1979), however, demonstrated the effect of anisotropic stress states on the elastic stiffness in various directions, leading to the development of an empirical equation in terms of the individual stress components to estimate elastic stiffness.

However, the effects of boundary conditions, initial states, and soil characteristics, along with anisotropic stress states, on the small-strain stiffness and its cross-anisotropy, as well as the development of appropriate correlations and equations to predict stiffness in different directions, remain areas of interest. Therefore, the main objectives of this research can be summarized as follows:

1. **Boundary conditions:** Investigation of the effect of an isotropic or anisotropic stress state under drained and undrained conditions on small-strain stiffness. To achieve this objective, a triaxial device combined with bender and compression elements was designed, manufactured and applied in the framework of this research.
2. **Initial conditions:** Evaluation of the effect of sample preparation on the cross-anisotropy of the prepared samples. In that context the two most popular preparation methods in geotechnical laboratories, air pluviation and moist tamping, are compared.
3. **Grain size distribution and particle shape:** Assessment of the effect of grain size distribution and particle shape in combination with stress state (isotropic and anisotropic) on the cross-anisotropy of sand specimens. For that purpose, mixtures of three materials with significantly different grain shape - round glass beads, sub-angular natural sand and angular crushed glass - were tested with two different gradations.
4. **Empirical relations:** Description of the experimental observations by extended empirical equations for small-strain stiffness.

1.5 Organization of the thesis

The thesis is organized in six chapters as described in the following.

- **Chapter 1: Introduction** - The current first chapter introduces the motivation, objectives, and organization of the thesis.
- **Chapter 2: Literature review** - This chapter provides a review of previous experimental and numerical studies on the effects of material characteristics, boundary conditions, and soil fabric on wave velocities and elastic stiffness.
- **Chapter 3: Materials, experimental methods and testing program** - In this chapter the materials and devices used in the current research are described. Beside the three materials with significantly different grain shape mentioned above, also Hostun sand was used in the current experiments. The determination of grain shape is explained, and the shape descriptors of all materials are presented. The extension of a triaxial device by piezoelectric elements is detailed, including bender elements and compression elements incorporated in the end plates, as well as bender elements attachable to the boundaries of the specimens. This technique allowed

the measurement of shear and compression wave velocities in different directions during a conventional triaxial test. The calibration, optimization and validation of the measurements with the piezoelectric elements is outlined. The applied sample preparation methods are described. Furthermore, the program of the various test series performed is presented.

- **Chapter 4: Experimental results** - This chapter presents and discusses the results of the wave propagation measurements. The first test series investigates the influence of the sample preparation method on the small-strain stiffness of Hostun sand and its anisotropy, under both isotropic and anisotropic stress states, the latter achieved after a drained shearing phase. The second test series is dedicated to the effect of the anisotropic stress state, whereby a drained and undrained loading on Hostun sand are compared. Finally, the third test series studies the effect of the particle shape and grain size distribution, utilizing the mixtures of the three materials with significantly different particle shapes and two different gradations. These six materials were tested under drained conditions, step-wise applying the same stress path comprising an initial isotropic loading followed by a deviatoric loading.
- **Chapter 5: Empirical equations** - In this chapter the experimental results are used to calibrate and refine empirical equations for predicting the small-strain stiffness. In particular, the effects of stress anisotropy and particle shape on the constants in the empirical equations are studied.
- **Chapter 6: Conclusions and outlook** - The last chapter summarizes the most important conclusions of the research reported herein and gives an outlook on possible future research on this field.

2 Literature review

Numerous experimental studies have been conducted to evaluate the effect of various factors (e.g., the void ratio, e, stress states, mean grain size, particle gradation, fines content, and particle shape) on the elastic stiffness at small strains or the corresponding wave velocities of soils in the laboratory, using the piezoelectric element technique (e.g. Bellotti et al., 1996; Zeng & Ni, 1998; Fioravante, 2000; Sadek et al., 2007; Wang & Mok, 2008; Ng et al., 2009; Ezaoui & Di Benedetto, 2009; Goudarzy et al., 2016a) or resonant column devices (e.g. Hardin & Black, 1966; Yanagisawa, 1983; Yu & Richart, 1984; Ishibashi & Agarwal, 1991; Santamarina & Cascante, 1996; Wichtmann & Triantafyllidis, 2009, 2013; Payan et al., 2016a; Goudarzy et al., 2016b, 2017).

Some of these studies, related to the objectives of this research, are considered in more detail below. These studies, and thus this chapter, are divided into:

1. Studies on the formulation of empirical equations for the elastic stiffness
2. Studies on the effect of sample preparation
3. Studies on the effect of boundary conditions
4. Studies on the effect of material characteristics

Also numerical studies using the discrete element method (DEM) are addressed to shed some lights on the micromechanics behind the experimental observations.

2.1 Empirical equations for the elastic stiffness

Numerous previous studies have revealed that the small-strain shear modulus $G_{\max}$ is highly affected by the stress state and void ratio, e. To characterize this relationship, Hardin & Black (1966) proposed an empirical equation, which has been widely used in the previous studies:

$$G_{\max} = A\ p_a\ f(e) \left(\frac{p'}{p_a}\right)^n \tag{2.1}$$

where

- A is a dimensionless elastic stiffness coefficient for a material adopted (Hardin & Black, 1966), also termed material constant (Mitchell & Soga, 2005). It may reflect the soil structure or fabric (Hardin & Blandford, 1989; Jamiolkowski et al., 1991; Stokoe et al., 1991) and particle characteristics (Bui, 2009; Wichtmann & Triantafyllidis, 2010);
- p_a is a reference stress and is usually assumed to be the atmospheric pressure, $p_a =$ 100 kPa;
- $f(e)$ is a void ratio function which may also be affected by the fabric induced by deposition (Hardin & Blandford, 1989) and the type of soils (Jamiolkowski et al., 1991);
- p' is the mean effective stress and is generally calculated with the principle effective stresses, $p' = (\sigma'_1 + \sigma'_2 + \sigma'_3)/3$;
- n is a stress exponent that may depend on particle shape, particle size and gradation.

Previous studies on the formulation of the void ratio function $f(e)$ are discussed in more detail in the following section.

2.2 Influence of void ratio

Void ratio, e, is generally defined as the ratio of the pore (voids) volume V_P to the volume of the solid particles V_S, and is directly related to the density, ρ, of soils. As it is obvious from previous studies an increase of void ratio leads to a reduction of the wave velocities and consequently of the elastic stiffness (e.g. Hardin & Black, 1966; Yanagisawa, 1983; Yu & Richart, 1984; Ishibashi & Agarwal, 1991; Santamarina & Cascante, 1996; Wichtmann & Triantafyllidis, 2009, 2013; Payan et al., 2016a; Goudarzy et al., 2016b, 2018). Two examples of respective experimental data published by Hardin & Richart (1963) and Wichtmann & Triantafyllidis (2004*b*) are provided in Figure 2.1.

In empirical equations for the small-strain stiffness, the effect of void ratio has been taken into account by using a void ratio function, $f(e)$. Various equations for $f(e)$ in Equation 2.1 were proposed in the literature, a summary of which is presented in Table 2.1. Two

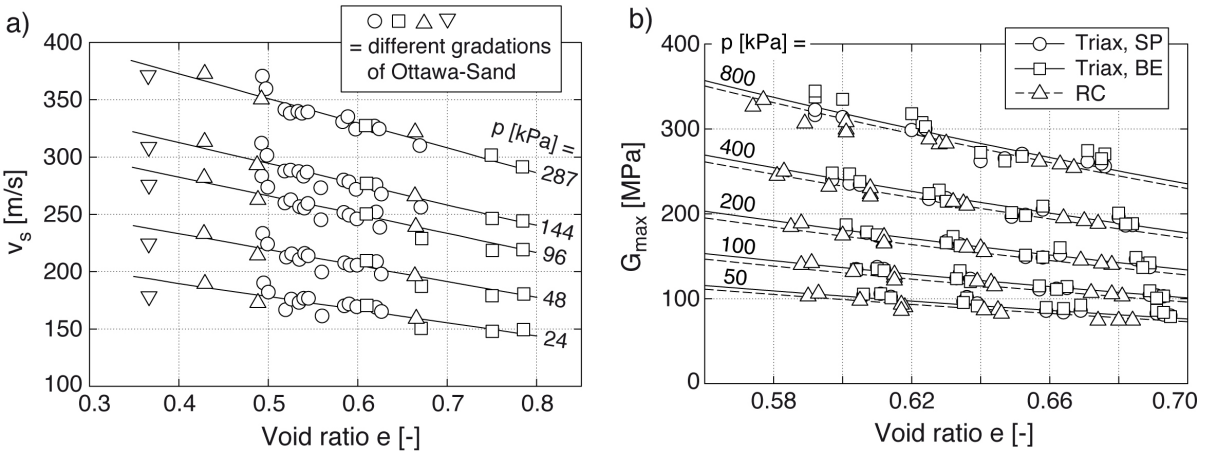

Figure 2.1: Decrease of shear wave velocity v_s or small-strain shear modulus $G_{\max}$ with increasing void ratio at different isotropic stress levels p': tests of a) Hardin & Richart (1963) and b) Wichtmann & Triantafyllidis (2004*b*) (RC = resonant column tests, BE = bender elements, SP = shear plate elements) (modified from Hardin & Richart (1963) and Wichtmann & Triantafyllidis (2004*b*)).

forms of $f(e)$, which have been widely adopted in previous studies and are also applied in the current research, have been proposed by Hardin & Black (1966) and Jamiolkowski et al. (1991). The equation of Hardin & Black (1966) is given in Equation 2.2.

$$f(e) = \frac{(c-e)^2}{1+e} \tag{2.2}$$

where c is a constant value for a certain material, and is related to the roundness of particles by Hardin & Black (1966) ($c = 2.97$ for angular sands and $c = 2.17$ for rounded sands). The void ratio function of Jamiolkowski et al. (1991) is presented in Equation 2.3.

$$f(e) = e^{-x} \tag{2.3}$$

where x is a constant value depending on the type of soils.

From a micro-mechanical perspective, the effect of void ratio could be understood in terms of the change in the number of contacts per particle in the specimens. The number of contacts is commonly quantified by the coordination number, N_c, which is defined as the number of contacts divided by twice the number of particles in the granular packing. Experimental and theoretical studies have been performed on spheres to investigate the relationship between e and N_c (e.g. Smith et al., 1929; Field, 1963; Gray, 1968; Yanagisawa, 1983). Graton & Fraser (1935) analysed the effect of various regular packings of

Table 2.1: Various void ratio functions and stress exponents compiled from the literature (modified from Mitchell & Soga, 2005)

References	Soils	Void ratio	$f(e)$	n
Hardin & Black (1966)	Ottawa sand	0.37-0.78	$\frac{(2.174-e)^2}{1+e}$	0.5
	Crushed quartz	0.63-1.26	$\frac{(2.973-e)^2}{1+e}$	0.5
Hardin & Black (1968)	NC Kaolinite	0.76-0.9	$\frac{(2.973-e)^2}{1+e}$	0.5
Marcuson & Wahls (1972)	Kaolinite	1.1-1.31	$\frac{(2.973-e)^2}{1+e}$	0.5
	Bentonite	1.61-2.48	$\frac{(4.4-e)^2}{1+e}$	0.5
Kokusho et al. (1982)	NC clay (Japan)	1.73-3.86	$\frac{(7.32-e)^2}{1+e}$	0.6
Athanasopoulos & Richart (1983)	Kaolinite clay	0.9-1.2	$(0.3+0.7e^2)^{-1.361}$	0.49
Pincus et al. (1993)	Ticino sand	0.61-0.80	$\frac{(2.27-e)^2}{1+e}$	0.43
Jamiolkowski et al. (1995)	Panigalia clay	1.4-1.8	$e^{-1.3}$	0.5
	Pisa clay	0.8-1.8	$e^{-1.43}$	0.44
	Garigliano	0.9-1.2	$e^{-1.11}$	0.58
	Fucino clay	1.6-3.0	$e^{-1.52}$	0.40
	Montalvo di Castro	0.6-0.8	$e^{-1.33}$	0.40
	Avezzano	1.0-1.8	$e^{-1.27}$	0.46
Shibuya & Tanaka (1996)	Insitu slight OC clay	1.3-4.5	$e^{-1.5}$	0.5
Shibuya et al. (1997)	Natural sediment	1.0-6.0	$(1+e)^{-2.4}$	0.5
Lo Presti et al. (1997)	Toyoura sand	0.81-0.98	$e^{-1.3}$	0.45
	Quiou sand	0.84-1.18	$e^{-1.3}$	0.62
Fioravante (2000)	Ticino sand	0.578-0.927	$e^{-0.8}$	0.44
	Kenya sand	1.282-1.776	$e^{-0.8}$	0.452
Wichtmann & Triantafyllidis (2004a)	Fine and medium sands	0.57-0.76	$\frac{(1.46-e)^2}{1+e}$	0.42
Zhou & Chen (2005)	Fine sand	0.593-1.096	$\frac{(2.973-e)^2}{1+e}$	0.51
	Medium sand	0.432-0.788		0.505
Yang & Gu (2013)	Glass beads A, B, and C	0.558-0.595	$\frac{(2.17-e)^2}{1+e}$	0.4
Yang & Liu (2016)	Toyoura sand	0.791-0.937	$\frac{(2.17-e)^2}{1+e}$	0.37
Goudarzy et al. (2016b)	Hostun sand	0.671-1.023	$\frac{(2.12-e)^2}{1+e}$	0.441

single-sized spheres on void ratio and coordination number. The results are presented in Table 2.2, showing an increase of N_c with decreasing void ratio.

Table 2.2: Void ratio, e, and coordination number, N_c, of four regular packings of spheres with a single size (after Graton & Fraser, 1935)

Packing	e	N_c
Cubic	0.910	6
Ortho-rhombic	0.654	8
Tetragonal	0.433	10
Rhombohedral	0.350	12

Several empirical equations correlating N_c with e have been proposed in the literature, as summarized in Equations 2.4 to 2.9. Therein the asterix * after the authors indicates that the equation has been modified by replacing porosity, n, with void ratio, e, based on the relationship $n = e/(1 + e)$.

Smith et al. (1929):

$$N_c = 26.4858 - 10.7262(1 + e) \tag{2.4}$$

Filep (1936)*:

$$N_c = 3.1 \left(\frac{1 + e}{e} \right) \tag{2.5}$$

Field (1963):

$$N_c = \frac{12}{1 + e} \tag{2.6}$$

Meissner (1964)*:

$$N_c = 2 \exp \left(\frac{12.4e}{1 + e} \right) \tag{2.7}$$

Ridgway and Turback (1969)*:

$$N_c = 1.072 - 0.1193 \left(\frac{e}{1 + e} \right) + 0.00432 \left(\frac{e}{1 + e} \right)^2 \tag{2.8}$$

Yanagisawa (1983):

$$N_c = 3.183^{(2.469 - e)} \tag{2.9}$$

Field (1963) proposed an empirical equation (Equation 2.6) to predict N_c in a random packing of round stones having various grain size and gradation. Oda (1977) conducted a series of tests on random assemblies of spheres with a single size and with various sizes, respectively. The results are shown in Figure 2.2a compared to those from the

aforementioned study. Although the predicted curve does not match the experimental results well, all results show that the N_c decreases with an increase in void ratio of the specimens.

Yanagisawa (1983) studied the distribution of contact points in a random packing of three materials having particles of different shape but similar size of about 20 mm. Their results were compared with those from Oda (1977) and the aforementioned empirical equations, as seen in Figure 2.2b. They concluded that for the gravel particles tested in their study Equation 2.5 could approximately characterize the relation between N_c and e.

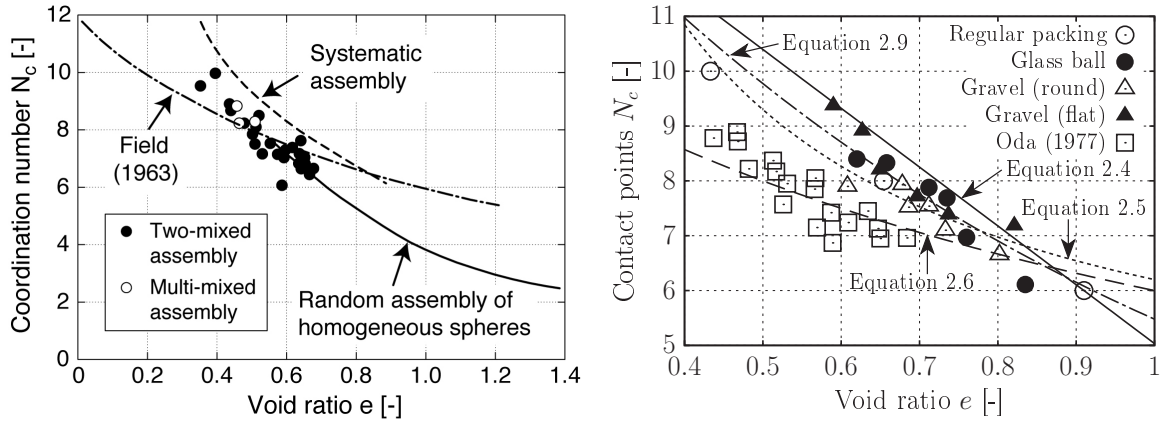

(a) (b)

Figure 2.2: Relation between coordination number and void ratio in: (a) specimens of spherical particles with various sizes (modified from Oda, 1977), (b) specimens of granular materials with different particle shape (modified from Yanagisawa, 1983).

The previous studies have shown the same tendency that N_c decreases with an increase in e, although N_c varies at the same e due to particle shape, particle size and gradation etc. Santamarina & Cascante (1996) suggested that the specimen keeps stable as long as the N_c is lager than the minimum N_c for stable configurations, and the higher N_c the more stable the specimen is. This may explain why also $G_{\max}$ increases with decreasing void ratio.

2.3 Influence of sample preparation method

Numerous efforts have been made to assess the effect of the method of sample preparation on the mechanical behaviour of granular materials under monotonic (e.g. Oda, 1972; Miura

& Toki, 1982; Kuerbis & Vaid, 1988; Juneja & Raghunandan, 2010) and cyclic loading (e.g. Mulilis et al., 1977; Miura & Toki, 1982; Tatsuoka et al., 1986; Ghionna & Porcino, 2006; Sze & Yang, 2014). These previous studies reported that the mechanical behaviour of a certain material prepared at the same void ratio was highly affected by the preparation methods adopted, and considered that the effect of sample preparation is due to the initial fabric and its anisotropy induced by different preparation methods. This finding is consistent to the suggestion by Santamarina & Cascante (1996) that the change in e may not reflect the real change in coordination number in the specimens with anisotropic fabric. Based on the performed literature review, the effect of sample preparation on soil behaviour at the small and large strain level will be discussed.

The effect of fabric on soil behaviour may not only reflect the anisotropy of the fabric (Yimsiri, 2001), but also the contact number and the coordination number (Magnanimo et al., 2008; Goudarzy, 2015). Yimsiri (2001) performed discrete element simulations of drained triaxial tests conducted on three-dimensional specimens composed of equal-sized spheres. Three specimens prepared with similar void ratio (e = 0.75 - 0.76) but with different orientations of the contact normals were considered. The variations of stress ratio, q/p', and fabric anisotropy described by the parameter A proposed by Radjai (1999) are shown with respect to axial strain in Figure 2.3a and b, respectively. Figure 2.3a shows that the specimen A having more contact normals in the vertical direction showed a stiffer response during compression testing whereas the specimen C having more contact normals in the horizontal direction showed a softer response. Also during triaxial extension testing the specimen A showed a stiffer response during extension than the specimen C. The specimen B which has an isotropic fabric, was always between the other two specimens. The results of the simulations agree to the experimental findings by Oda (1972).

Using DEM simulations Magnanimo et al. (2008) and Goudarzy (2015) showed that different sample preparation procedures can lead to different numbers of contacts and coordination numbers in the specimens with the same density. This yields samples with the same density but different shear stiffness.

Tatsuoka et al. (1979) conducted a series of resonant column and torsional shear tests on Toyoura sand. The specimens in their experiments were prepared by different methods with various initial water contents and relative densities ranging from 40.6 to 100%. The $G_{\max}$ values were measured under isotropic stresses of 20, 50, 100, 200 and 400 kPa. Tatsuoka et al. (1979) reported that the measured shear modulus is insensitive to the sample preparation method after the second cyclic loading (see Figure 2.4). However, in their study, the specimens tested under the fully dry or saturated conditions had relative

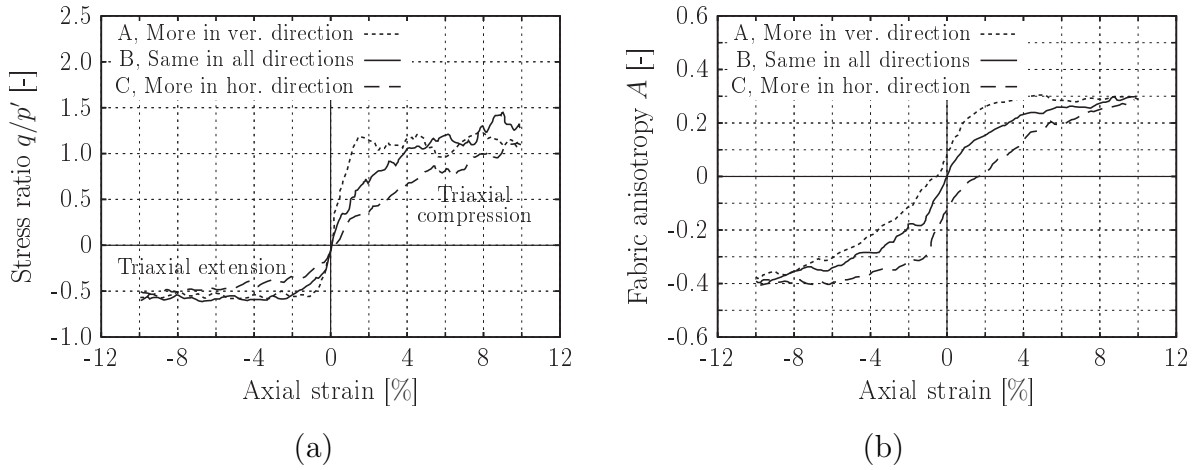

Figure 2.3: Discrete element simulations of drained triaxial compression and extension tests of particle assemblies prepared at different initial fabrics: (a) stress-strain relationships and (b) evolution of fabric anisotropy parameter A (modified from Yimsiri, 2001).

densities in the range between 75 and 100%. In other studies the different mechanical behaviour was mostly observed for loose specimens with relative densities less than 40%.

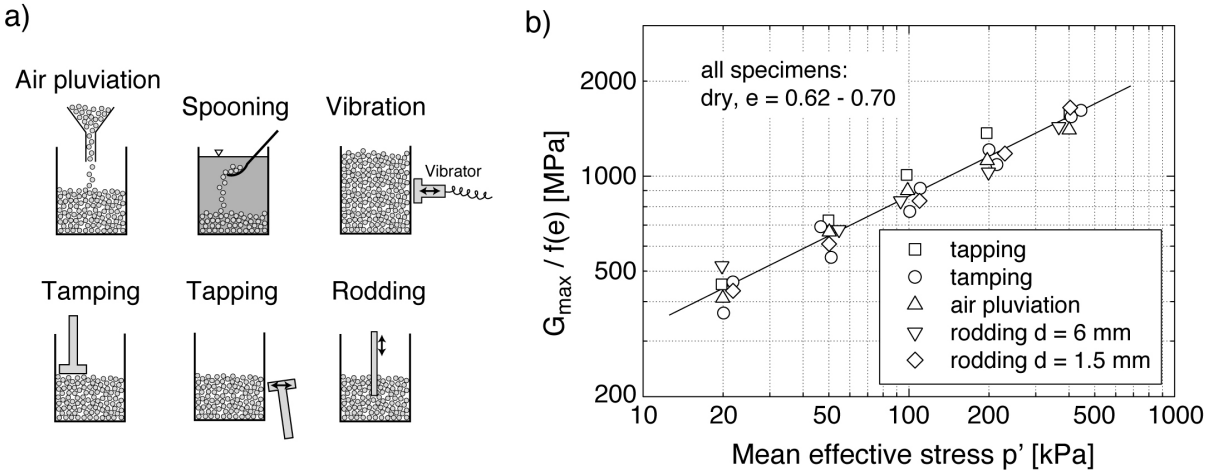

Figure 2.4: Only moderate influence of the specimen preparation method on small-strain shear modulus $G_{\max}$ normalized with void ratio function $f(e)$ and plotted versus mean effective stress p' (modified from Tatsuoka et al., 1979).

Yang et al. (2008) reported that loose specimens prepared with the dry deposition method possess obviously inherent anisotropy in the vertical plane, whereas loose samples formed with the moist tamping method tend to be more isotropic, based on the analysis of images taken with a scanning electron microscope (SEM), as shown in Figure 2.5a. In this figure, the axes with the values ranging from -180 to 180 denote particle orientation with

respect to the horizontal axis (0 and 180), while the scale shows the percentage of the number of particles with that orientation. It can be seen that the particle orientations are concentrated in the horizontal direction for loose specimens prepared with the dry deposition method (denoted as filled bars), while for loose specimens prepared with the moist tamping method the orientation of particles (denoted as dashed bars) is more randomly distributed. Figure 2.5b shows that the orientation of the particles is similar in the horizontal section of the specimens prepared by both methods.

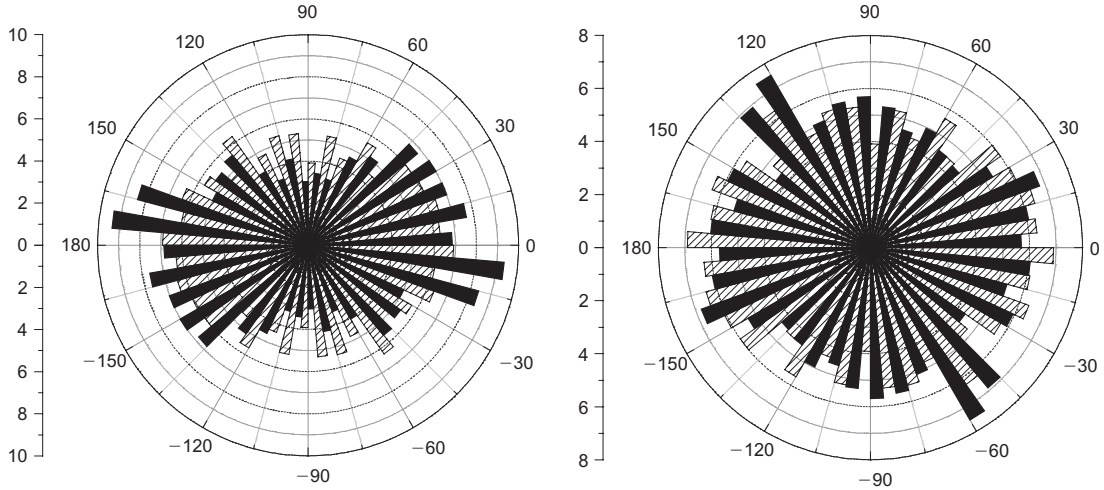

Figure 2.5: (a) Characterisation of inherent fabric anisotropy of Toyoura sand with preferred particle orientations represented in rose diagrams: (a) for vertical sections, (b) for horizontal sections (Yang et al., 2008). Filled bars: dry deposition method; dashed bars: moist tamping method.

Aris et al. (2012) measured the shear wave velocities, v_{hv} and v_{hh}, with horizontal propagation direction but different polarization directions in specimens prepared with different methods, including moist tamping, air pluviation and water pluviation. They concluded that the moist tamping method leads to a higher degree of initial anisotropy compared to the air and water pluviation methods. The results obtained from the specimens with a relative density of $D_r = 3\%$ are summarized in Table 2.3. In contrast, Shi et al. (2021) reported that the specimens prepared by the moist tamping method have less anisotropy ratio, G_{hh}/G_{hv}, than those prepared by the other methods. For instance, Figure 2.6a shows that the anisotropy ratio for the specimen prepared by the moist tamping method is less than 0.9, and almost 20% less than those for the specimen prepared under dry conditions.

Table 2.3: Comparative v_{hh} and v_{hv} measurements for different preparation methods (after Aris et al., 2012).

Methods	D_r [%]	v_{hh} [m/s]	v_{hv} [m/s]	v_{hh}/v_{hv} [-]
Moist tamping	3	203.4	190.0	1.07
Dry pluviation	3	213.2	217.4	0.98
Water pluviation	3	218.5	220.4	0.99

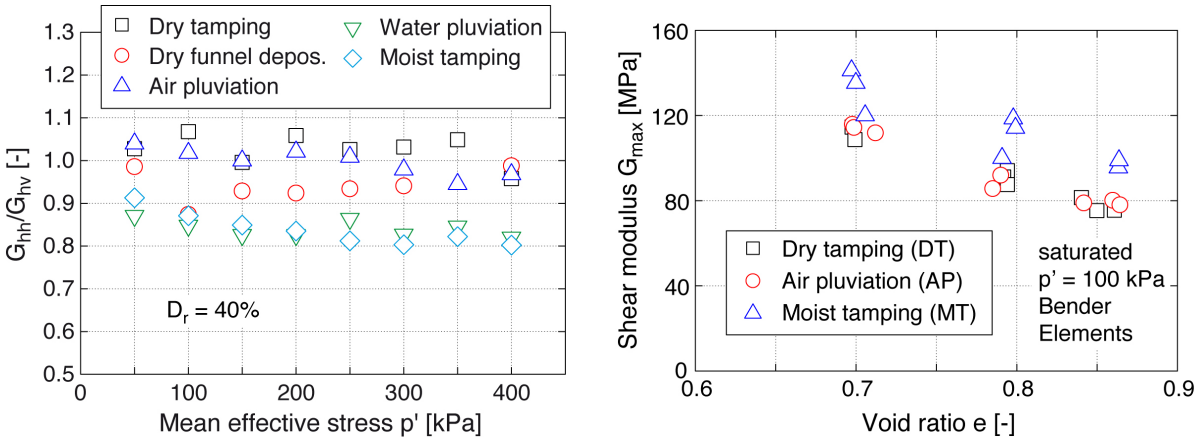

(a) (b)

Figure 2.6: (a) Ratio of G_{hh} to G_{hv} obtained from specimens prepared by various methods with an identical relative density of 40%, with respect to mean effective stress (modified from Shi et al., 2021); (b) $G_{\max}$ obtained from bender element measurements for specimens prepared by various methods (modified from Gu et al., 2015).

Gu et al. (2015) measured the maximum shear modulus, $G_{\max}$, of Toyoura sand using bender elements (BE), a resonant column device (RC) and a torsional shear device (TS). The specimens were prepared using three different methods, namely the dry air pluviation (AP) method, the dry tamping (DT) method and the moist tamping (MT) method, respectively. They reported that the G_{max} obtained from the specimens prepared with the AP and DT methods are consistent to each other in the three devices adopted in their study, but are always less than the $G_{\max}$ measured from the specimens prepared by the MT method. For instance, Figure 2.6b presents the $G_{\max}$ data from the bender element measurements, showing that the values from the specimens prepared by the MT method are about 14% larger than those from the specimens prepared with the AP and DT methods.

Generally, studies on the effect of the sample preparation method on the wave velocities as well as the fitting parameters of empirical relationships are rare. This motivates the further research undertaken in the framework of the current thesis. Furthermore, the impact of the initial water content used in the moist tamping method on the fabric of samples should be studied. Such investigations can give hints which sample preparation method provides specimens with a more isotropic fabric for a certain adopted sand.

2.4 Influence of boundary conditions

This section focuses on the effect of the isotropic and anisotropic stress conditions and the saturation state on the small-strain stiffness and the wave velocities of granular materials.

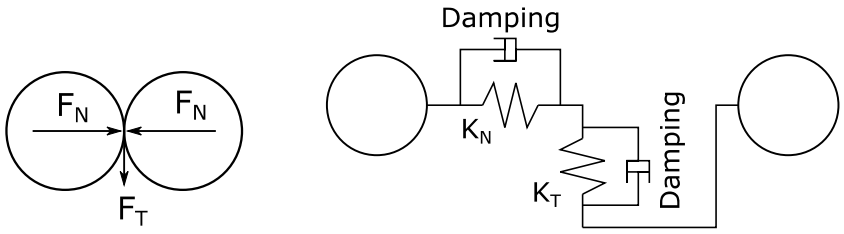

(a) (b)

Figure 2.7: Schematic sketch for: (a) contact forces and (b) contact model between two particles

From a micromechanical perspective, the stiffness of granular materials is dominated by the micro-structure which is mainly related to a coupling of particle and contact properties (seen in Figure 2.7). In the Hertz-Mindlin's theory, the normal and tangential contact stiffness, K_N and K_T, are defined as shown in Equation 2.10 (Mindlin & Deresiewicz, 1953) and Equation 2.11 (Bowden & Tabor, 1964; Johnson, 1985), respectively.

$$K_N = L_1 F_N^{\Omega} \tag{2.10}$$

$$K_T = L_2 K_N \left[1 - \frac{F_T}{F_N \tan\phi}\right]^{\varsigma} \tag{2.11}$$

Therein L_1 and L_2 depend on the particle properties (e.g. the Poisson's ratio and shear modulus of soil particles), Ω and ς are material constants ($\Omega = \varsigma = 1/3$, Yimsiri & Soga (2002)), ϕ is the friction angle between two particles, and F_N and F_T are the normal and tangential contact forces. It was found that for a given material the distribution

of contact forces within the granular packing has a major contribution to the overall stiffness. Previous studies (e.g. Petrakis et al., 1988; Rothenburg & Bathurst, 1989; Ng & Petrakis, 1996; Wang & Mok, 2008; Goudarzy, 2015) reported that the effective stress conditions have a large impact on the distribution and magnitude of the contact forces. In the following sections, the effects of isotropic and anisotropic stress conditions on the small-strain stiffness are discussed separately. Both types of stress boundary conditions have been investigated in the present thesis.

In addition, all specimens tested in the present thesis were fully water-saturated in order to determine the change in specimen volume under different stress paths. The saturated specimens should have the same mechanical characteristics as dry specimen under the identical effective stress conditions. However, it has been reported by theoretical (Biot, 1956*a*,*b*) and experimental (e.g. Hardin & Richart, 1963; Qiu & Fox, 2008; Gu et al., 2015) studies that the pore fluid can have a significant impact on the wave velocity depending on the frequency of the wave. The effect of saturation on the wave velocity and the calculation of the small-strain stiffness with the wave velocity obtained in the saturated specimens are thus discussed in another section.

2.4.1 Isotropic stress state

The increase of the shear wave velocity or the small-strain shear modulus with increasing isotropic effective stress has been demonstrated by numerous studies in the literature. It is also visible in the experiments by Hardin & Richart (1963) and Wichtmann & Triantafyllidis (2004*b*) shown in Figure 2.1.

Studies using the discrete element method (e.g. Petrakis et al., 1988; Ng & Petrakis, 1996; Goudarzy, 2015) reveal that the variation of the isotropic effective stress does not change the micro-structure (e.g. contact normal distribution, coordination number and particle orientations) of the specimens but causes a change in the magnitude of the contact forces. Petrakis et al. (1988) calculated the coordination number of the specimens prepared using the random packing method under three isotropic stresses, and pointed out that there is no significant change in the coordination number and in the contact normal distribution of each specimen due to the varying isotropic stress. In the study from Ng & Petrakis (1996), nine specimens that are isotropically consolidated with nine stresses at the same void ratio were found to have a similar coordination number. Goudarzy (2015) compared the contact properties (e.g. coordination number, tangential contact force, normal contact force, and contact normal distribution) in specimens prepared at a void ratio of 0.58 under

various isotropic stresses. The results indicate that only normal contact force corresponds significantly to the varying isotropic stress, and the other properties increase slightly with the increasing stress, which is consistent to the aforementioned studies.

To define the relation between the isotropic stress and the small-strain stiffness, several studies were carried out on spheres. Gassmann (1951) and Brandt (1955) calculated the velocities of elastic waves propagated in a packing of spheres. Their calculations indicate that elastic wave velocities are proportional to $(p')^{1/6}$. Based on the physical relation between shear wave velocities and the maximum shear modulus, $G_{\max} = \rho {v_s}^2$, it can be concluded that the maximum shear modulus should be proportional to $(p')^{1/3}$. This was confirmed by the studies from Duffy & Mindlin (1957) and Duffy (1959) on the tangential stiffness of a packing of spheres. Similar studies carried out on regular packings (e.g. Petrakis & Dobry, 1987) and random packings (e.g. Walton, 1987; Liao et al., 2000) also reported that the stress exponent for the isotropic stress condition is equal to 1/3. However, the materials adopted in the aforementioned studies were spheres which have an isotropic shape. The stress exponent as an indicator for the contact condition can range from 1/3 for spherical contacts to 1/2 for cone-plane contacts (Cascante & Santamarina, 1996). The stress exponents, n, reported by the previous studies are summarized in Table 2.1. This table shows that the stress exponent determined from the most previous experiments varies from 0.37 to 0.51 except NC clay (Kokusho et al., 1982), Gariglianno (Jamiolkowski et al., 1995) and Quiou sand (Lo Presti et al., 1997) having stress exponents much higher than 0.55. In sum, there is a linear relation between $G_{\max}$ and $(p')^n$ for a given void ratio.

2.4.2 Anisotropic stress state

Hardin & Black (1966) believed that the effect of anisotropic loading can be neglected. However, their study was restricted to stress ratios σ_1/σ_3 less than about 2.0. Drnevich (1978) proposed to use the average stress in Equation 2.1 to capture the effect of anisotropic loading. Following these pioneer investigations, several other studies evaluated the effect of stress components on the elastic stiffness (e.g. Roesler, 1979; Yanagisawa, 1983; Yu & Richart, 1984).

Roesler (1979) compared the shear wave velocities obtained from cubical specimens under isotropic and anisotropic stress states. He reported that the shear wave velocity mainly depends on the stress components in the directions of wave propagation and polarization, and the stress component in the directions of wave propagation shows a higher impact on

the shear wave velocity than the one in the direction of wave polarization. In contrast, the stress component acting orthogonal to the plane of wave propagation was found to have almost no effect on the shear wave velocity. Selected results of Roesler (1979) confirming these conclusions are provided in Figure 2.8.

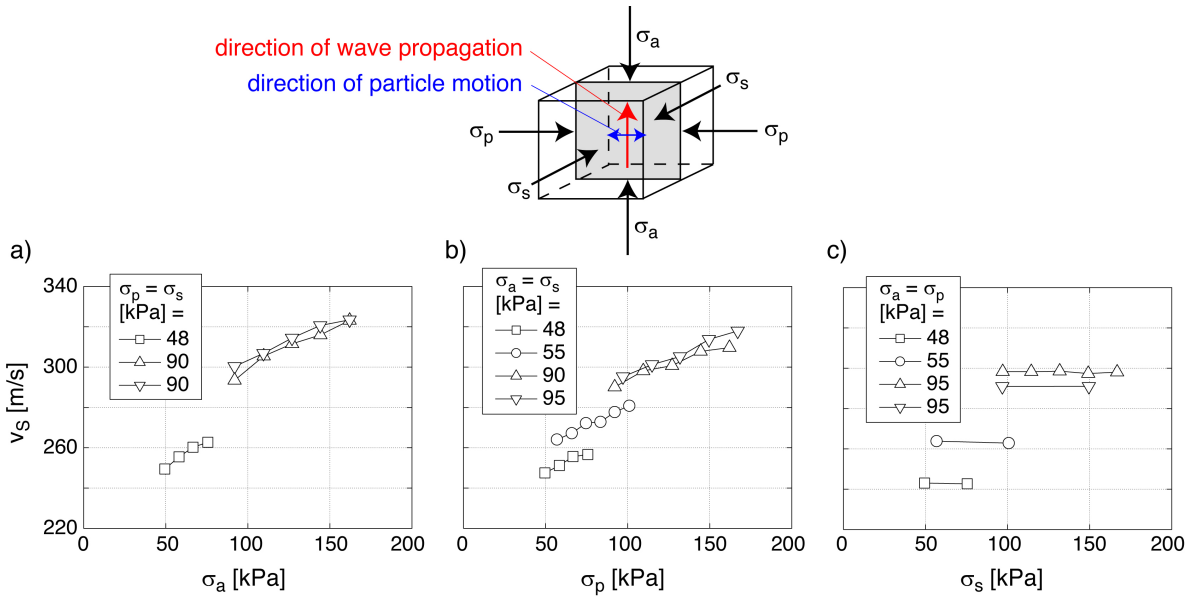

Figure 2.8: Variation of shear wave velocity v_s with an increase of the stress components σ_a (in wave propagation direction), σ_p (in polarization direction) or σ_s (orthogonal to plane of wave propagation and polarization), respectively (modified from Roesler, 1979).

Yanagisawa (1983) measured the small-strain stiffness of Toyoura sand under three compressional stress paths, and showed the experimental results normalized with predictions from Equation 2.1 in Figure 2.9a with respect to the stress ratio, σ'_1/σ'_3. It can be seen that the measured $G_{\max}$ agrees well to the one predicted with the empirical equation at the isotropic stress as $\sigma'_1/\sigma'_3 = 1.0$. Then, the measured value became larger than the predicted one with an increasing σ'_1/σ'_3 up to 2.0. When σ'_1/σ'_3 is beyond 3, a clear drop of the measured value can be observed.

The influence of stress anisotropy was also tested by Yu & Richart (1984) in resonant column tests. The ratio σ'_1/σ'_3 of the largest and the smallest principal stresses was increased along different stress paths, some of them with triaxial compression and others with triaxial extension. A reduction of the small-strain shear modulus with increasing ratio σ'_1/σ'_3 was observed which does not significantly depend on the stress path (Figure 2.9b). Only 10 % decrease was measured up to a stress ratio of $\sigma_1/\sigma_3 = 2.5$. Therefore, the effect of a stress anisotropy becomes significant particularly for stresses near failure.

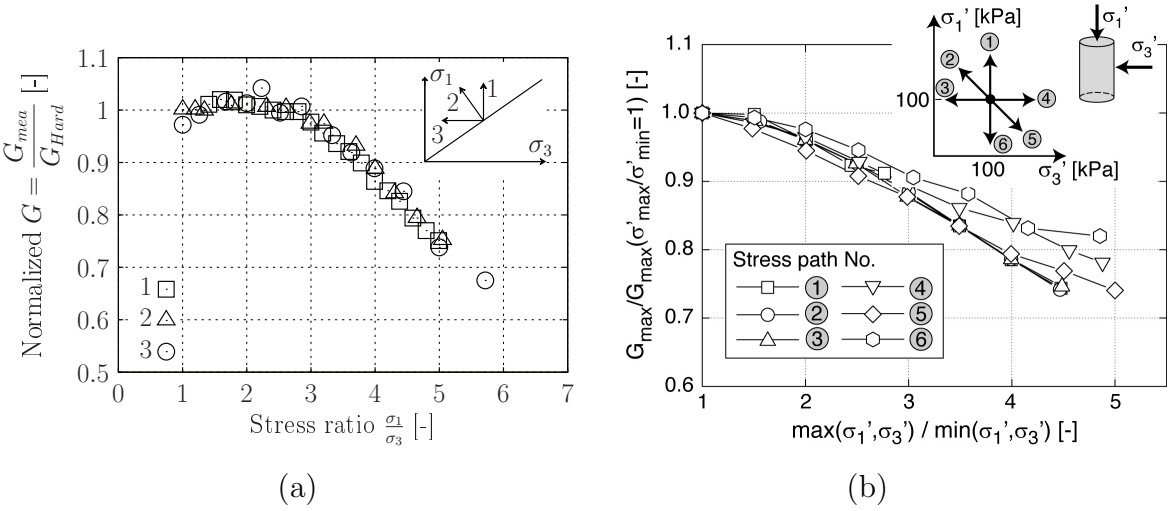

(a) (b)

Figure 2.9: Measured $G_{\max}$ normalized with values calculated from Hardin's equation versus the stress ratio under different stress paths (a) modified from Yanagisawa (1983), (b) modified from Yu & Richart (1984).

Bellotti et al. (1996) performed studies in a large calibration chamber on dry Ticino sand by sending shear as well as compressional waves through the soil specimens. They concluded that the stress ratio causes significant stress-induced anisotropy of the small strain stiffness of the Ticino sand. Hoque & Tatsuoka (2004) conducted cyclic triaxial tests on dry specimens of sands to investigate the effect of the stress ratio on the small-strain stiffness and estimated $E_{\max}$ or $G_{\max}$ values indirectly from the unloading-reloading cycle using a modified expression of Equation 2.1. No direct measurement of the small-strain stiffness was made in that study. Payan et al. (2016b) looked into the effect of stress anisotropy on the small-strain stiffness of saturated sand specimens by performing bender element tests at different stress ratios but constant mean effective stress while allowing volume change of the specimen (drained conditions). They consider a modification of Equation 2.1 for an estimation of $G_{\max}$ and suggest the need for decoupling the effects of void ratio and stress state.

Additionally, Figure 2.3b shows that the fabric anisotropy parameter of the three specimens having different inherent fabric reaches the same value at large strains, indicating a similar fabric at the critical state. Based on bender element tests on Toyoura sand, Guo & Yang (2017) proposed Equation 2.12 which links shear wave velocity with the state parameter $\Psi = e - e_c$, with e_c denoting critical void ratio:

$$v_s = (B - C\Psi)\left(\frac{p'}{p_a}\right)^m \tag{2.12}$$

Therein B, C and m are fitting parameters. From this equation, it can be concluded that at the critical state ($\Psi = 0$), the v_s can be predicted as a function of p', only. Additional experimental evidence for this hypothesis is needed, investigating the effect of the sample preparation method on the wave velocity at the critical state line.

2.4.3 Saturation

It is generally accepted that the stiffness of dry and fully water-saturated granular materials is the same under an identical effective stress. However, Hardin & Richart (1963) reported a difference of the wave velocities measured in Toyoura sand before and after saturation, as shown in Figure 2.10a. This difference is caused by the relative movement between the pore water and the particles due to the higher viscosity of water compared to air. It is clear that for water-saturated specimens the dry density should not be used to calculate the maximum shear modulus, $G_{\max}$, from the measured shear wave velocity, v_s. Biot (1956*a*) performed a mathematical analysis on the velocity of shear waves propagated in porous media and proposed an equation to correlate v_s and $G_{\max}$ as follows:

$$v_s = \sqrt{\frac{G_{\max}}{\frac{E_r + (E_r^2 + E_i^2)^{1/2}}{2}\ \rho_{\text{sat}}}} = \sqrt{\frac{G_{\max}}{\zeta\ \rho_{\text{sat}}}} \tag{2.13}$$

where E_r and E_i are two dimensionless parameters, ρ_{sat} is the total density of the saturated soil, and ζ is a density coefficient indicating the percentage of saturated density involved in the shear wave propagation. Biot (1956*a*) defined the characteristic frequency as shown in Equation 2.14:

$$f_c = \frac{n\ g}{2\pi\ k} \tag{2.14}$$

where n is the porosity, g is the gravity, and k is the hydraulic conductivity. Based on this definition, Gu et al. (2015) presented a relation between ζ and the frequency ratio, f/f_c, for Toyoura sand which is shown in Figure 2.10b. When the excitation frequency is in the range $f < 0.1 f_c$, ζ becomes one which indicates that the pore fluid and the particles move together in the shear wave propagation. When $f > 10 f_c$, ζ is significantly decreased and

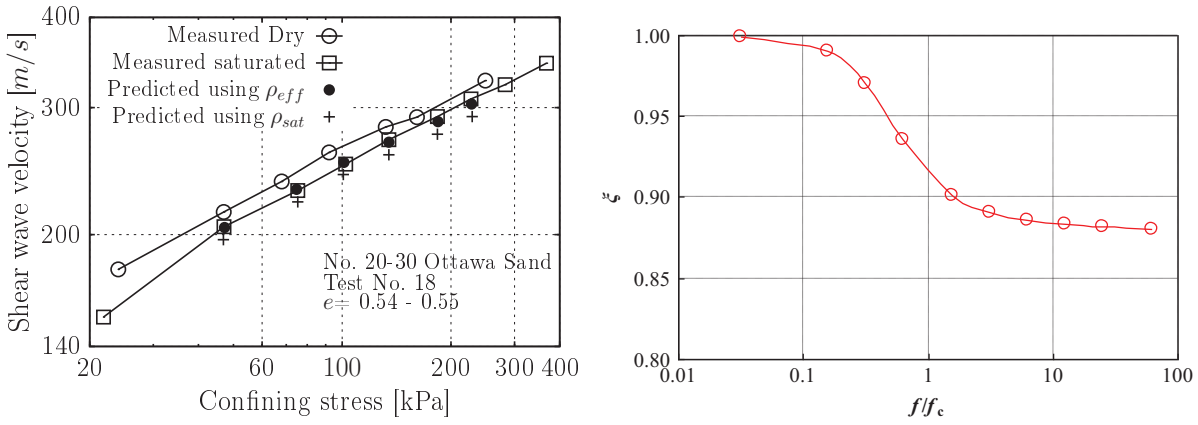

(a) (b)

Figure 2.10: (a) Measured and predicted values of shear-wave velocity for Ottawa sand (measured data points digitized from Fig. 7 of Hardin & Richart (1963), and predicted values calculated by Qiu & Fox (2008) considering the additional mass); (b) Dispersion curve of the density coefficient for Toyoura sand.

thus the relative movement between the solid and the fluid phase has to be taken into consideration in the calculation of $G_{\max}$.

The density coefficient ζ is difficult to determine, and was replaced by Biot (1962) with the following expression:

$$\zeta \ \rho_{\text{sat}} = \rho_d + n \ \rho_f \ (\delta - 1) \tag{2.15}$$

where ρ_d is the dry density of the soil, ρ_f is the density of the pore fluid, and δ is a structural factor representing the additional mass caused by tortuosity of the pore space (Stoll & Bryan, 1970). Sen et al. (1981) proposed a power relationship to assess the value of δ:

$$\delta = n^{-\beta} \tag{2.16}$$

where $\beta = 0.5$ for a random array of spheres, and $\beta > 0.5$ for a random array of platy particles. Qiu & Fox (2008) predicted the wave velocities in saturated Toyoura sand based on the additional mass and the stiffness of the dry specimen, and compared the calculated to the measured values from Hardin & Richart (1963), as shown in Figure 2.10b by the curve denoted $\rho_{\text{eff}} = \zeta \rho_{\text{sat}}$, showing an overall good agreement.

In the current thesis, $\beta = 0.5$ is used to approximate the mass coupling between fluid and solid phases, for calculating $G_{\max}$ based on v_s. The calculated results for Hostun sand are

consistent to those obtained in the previous studies (Ezaoui & Di Benedetto, 2009; Sadek et al., 2007; Azeiteiro et al., 2017; Goudarzy et al., 2016b). The details will be presented in Section 5.1.2.

2.5 Influence of grain size distribution and particle characteristics

Granular soils are assemblies of particles. The properties of the single particles and the assembly, such as mineralogy of particles, particle shape, size and gradation, significantly affect the mechanical behaviour of the soils. The influences of these parameters are discussed separately in the following.

2.5.1 Mineralogy of particles

Mineral composition of a particle determines the physical and mechanical properties of the particle. For instance, the mineral composition is directly related to the specific gravity (Terzaghi et al., 1996), and affects the elastic moduli (Mitchell & Soga, 2005) of a particle. In turn, the elastic moduli of particles are important to assess the mechanical properties (e.g. contact surface area, normal and tangent contact factor, etc.) at the contact between particles. Many researchers (e.g. Horn & Deere, 1962; Skinner, 1969; Koerner, 1970; Procter & Barton, 1974; Frossard, 1979) have also suggested that the mineral composition of particles has a significant influence on the inter-particle coefficient of friction.

2.5.2 Shape of particles

The particle shape of granular soils mainly reflects the history of their transportation and deposition. Longer transportation usually leads to more rounded particles.

Experiments have been conducted to investigate the effect of particle shape on the small-strain stiffness of granular soils. In several studies (e.g. Lo Presti et al., 1997; Bui, 2009; Senetakis et al., 2012; Payan et al., 2016a) at a given void ratio and confining pressure, the measured small-strain shear moduli of rounded sands were generally found higher than in their subangular or angular counterparts.

Hardin & Richart (1963) reported that the material constant c of the void ratio function defined by Equation 2.2 is significantly affected by particle shape, with a higher c value

for rounded materials. The relation between the pressure exponent n and grain shape is discussed controversially. Some studies found a decreasing trend of n with increasing roundness (e.g. Cho et al., 2006; Payan et al., 2016a) while some others encountered the opposite (e.g. Liu & Yang, 2018; Goudarzy & Wichtmann, 2019; Sarkar, 2022). Altuhafi et al. (2016) observed that n varies randomly.

For investigations on the influence of particle shape on the mechanical behaviour, the particle shape must be quantified by meaningful descriptors. Generally, the particle shape characteristics of soils can be categorized on three different scales, the macro, medium and micro scale. Numerous grain shape descriptors have been proposed for the various scales. An overview is provided e.g. by Sarkar et al. (2022). In the current thesis the three scales are represented by the descriptors sphericity, S, roundness, R, and roughness, respectively. Sphericity, S, is a parameter for the global form of a particle, and is considered as the similarity of the particle dimensions in different directions. Roundness, R, describes the major surface features of a particle. Roughness reflects the surface texture of a particle, and was not involved in this study.

Figure 2.11 shows a schematic sketch of a particle. Equation 2.17 presents the definition of sphericity. Sphericity, S, is quantified as the ratio of the radius of the largest inscribed circle, r_{ins}, to the radius of the smallest circumscribed circle, r_{cir}.

$$S = \frac{r_{\mathrm{ins}}}{r_{\mathrm{cir}}} \tag{2.17}$$

Equation 2.18 shows the definition of roundness. Roundness, R, is defined as the ratio of the average value of the radii, r_i, of the curvature of the corners of a particle, $\sum_{i=1}^{n} \frac{r_i}{n}$, to r_{ins}.

$$R = \frac{\sum_{i=1}^{n} \frac{r_i}{n}}{r_{\mathrm{ins}}} \tag{2.18}$$

Previous studies (e.g. Wadell, 1932; Powers, 1953; Krumbein & Sloss, 1963; Cho et al., 2006) revealed that there is no proportional relation between sphericity and roundness although they are both impacted by the environment of transportation and sedimentation. Figure 2.12 shows that angular particles can be equal dimensional, and non-spherical particles can have a well rounded shape. Similar findings have been also reported by Krumbein & Sloss (1963), leading to the development of a chart for particle shape determination as shown in Figure 2.13. In this chart, particles are categorized two-dimensionally with sphericity and roundness. The particles with the same roundness can show different sphericity, and vice versa.

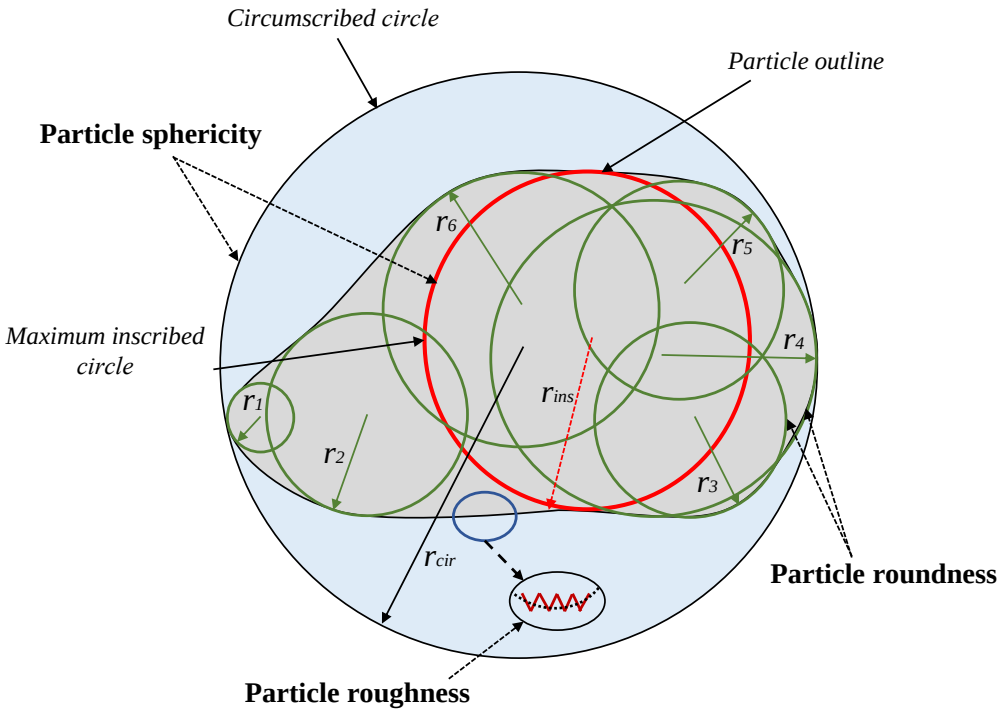

Figure 2.11: Schematic sketch showing the geometrical quantities needed for the determination of the particle shape parameters, sphericity S and roundness R. r_{cir} is the radius of the smallest circumscribed circle; r_{ins} is the radius of the largest inscribed circle; r_i (e.g. i = 1,...,6) is the radius of curvature of the i-th corner of a particle (Sarkar et al., 2020).

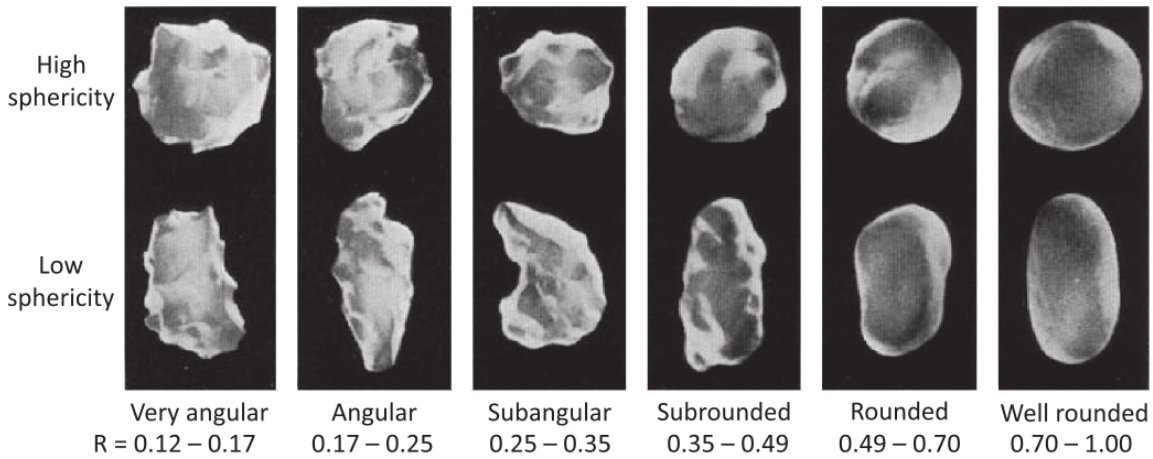

Figure 2.12: Comparison of the sphericity of the particles at different levels of the roundness. Image was scanned and roundness was calculated by Hryciw et al. (2016).

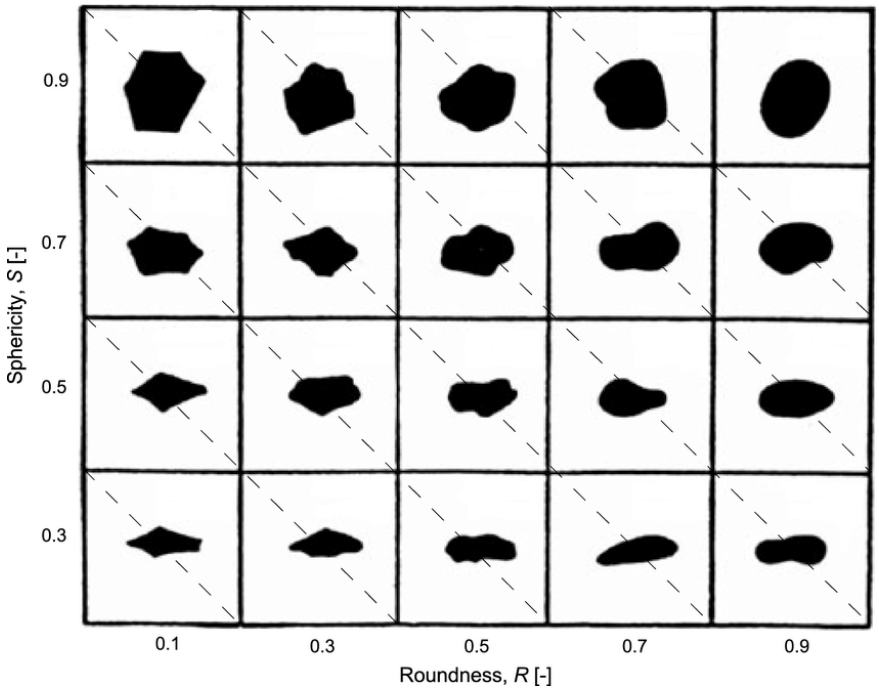

Figure 2.13: Chart for particle shape determination, quantitatively describing sphericity, S, and roundness, R (modified by Cho et al. (2006) from Krumbein & Sloss (1963)).

As either sphericity or roundness alone is not sufficient to describe grain shape adequately, the regularity factor, ρ, was introduced by Cho et al. (2006) to capture both features in one parameter. ρ is calculated as the mean value of S and R of a particle as shown in Equation 2.19:

$$\rho = \frac{R + S}{2} \tag{2.19}$$

While grain shape analysis was originally based on a visual comparison of particles with charts as that shown in Figure 2.13, image analysis is usually applied nowadays. Such analysis of images taken with scanners, microscopes or cameras provide a more objective evaluation of the grain shape parameters, which can consider also larger numbers of particles. However, as described in more detail in Chapter 3, high-quality images and a careful further processing of these images are needed to obtain reliable grain shape descriptors.

2.5.3 Particles size and gradation

Several studies demonstrated the significant effect of the grain size distribution on elastic stiffness. The available studies were restricted to G_{vh} and E_v, however.

The influence of mean grain size, d_{50}, is still debatable. Some studies (e.g. Iwasaki & Tatsuoka, 1977; Wichtmann & Triantafyllidis, 2009; Yang & Gu, 2013; Sarkar et al., 2024) suggest that d_{50} does not influence the small-strain stiffness of granular materials (see also Figure 2.14) while others (e.g. Menq & Stokoe, 2003; Hardin & Kalinski, 2005) found an increase in stiffness with increasing mean grain size. In addition, Liu et al. (2020) proposed that the influence of d_{50} on the small-strain stiffness is related to uniformity coefficient, C_u. Their study showed that the small-strain stiffness of poorly graded materials (C_u = 1.45) is insensitive to d_{50} ranging from 1.5 to 15 mm, while the small-strain stiffness of the well graded materials increases with d_{50}. However, there was only one material with d_{50} less than 2 mm for each set of materials adopted in their study.

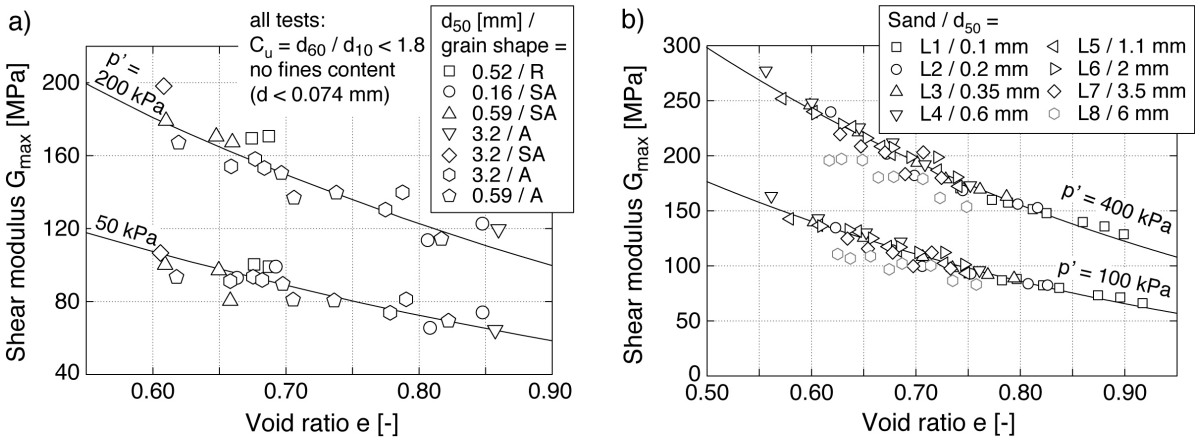

Figure 2.14: No influence of mean grain size d_{50} on small-strain shear modulus $G_{\max}$ according to experimental data of a) Iwasaki & Tatsuoka (1977) (grain shape: A = angular, SA = subangular, R = rounded) and b) Wichtmann & Triantafyllidis (2009) (modified from Iwasaki & Tatsuoka (1977) and Wichtmann & Triantafyllidis (2009)).

Furthermore, most authors (e.g. Iwasaki & Tatsuoka, 1977; Wichtmann & Triantafyllidis, 2009; Payan et al., 2016a; Sarkar, 2022) have reported that the small-strain shear stiffness decreases with increasing uniformity coefficient, $C_u = d_{60}/d_{10}$, at constant void ratio. Respective experimental data is provided in Figure 2.15. However, Menq & Stokoe (2003) found the opposite trend when considering similar relative density, with slightly higher $G_{\max}$ values for dense specimens with $C_u = 10$ compared to $C_u = 1.2$.

A fines content FC can also influence the small-strain stiffness (Iwasaki & Tatsuoka, 1977; Randolph et al., 1994; Salgado et al., 2000; Sahaphol & Miura, 2005; Wichtmann et al., 2015). The effect depends on the nature of the fines (plastic or non-plastic), on the host sand, and on the basis of comparison with respect to the density state (void ratio, equivalent void ratio, relative density). Figure 2.16a shows a compilation of relationships

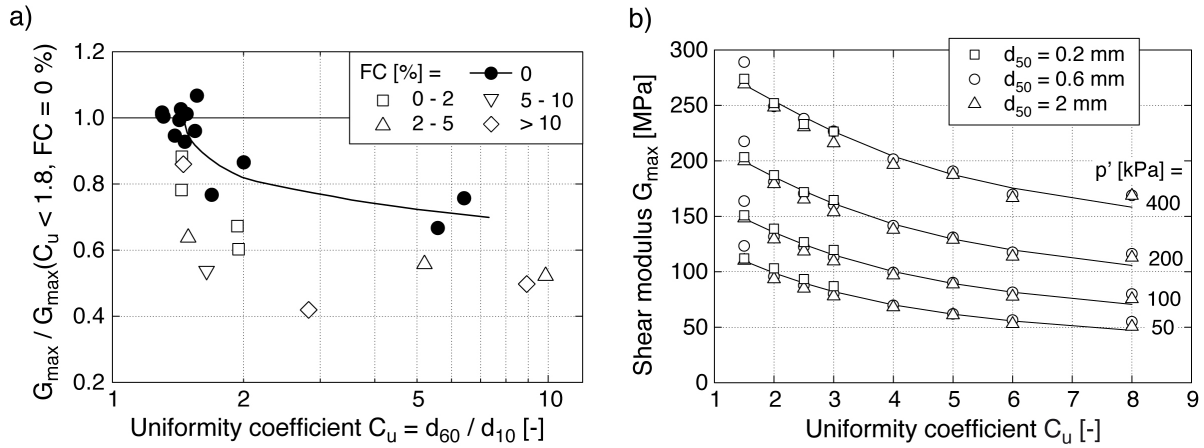

Figure 2.15: Decrease of small-strain shear modulus $G_{\max}$ with increasing uniformity coefficient C_u measured by a) Iwasaki & Tatsuoka (1977) for sands with different fines content and b) Wichtmann & Triantafyllidis (2009) at a constant void ratio $e = 0.55$ (modified from Iwasaki & Tatsuoka (1977) and Wichtmann & Triantafyllidis (2009)).

of the small-strain shear modulus versus silty fines content for a constant void ratio. All these studies demonstrate a significant decrease of $G_{\max}$ with FC. Such decrease for silty fines is also confirmed by the data from the studies of Iwasaki & Tatsuoka (1977) in Figure 2.15a and of Wichtmann et al. (2015) shown in Figure 2.16b.

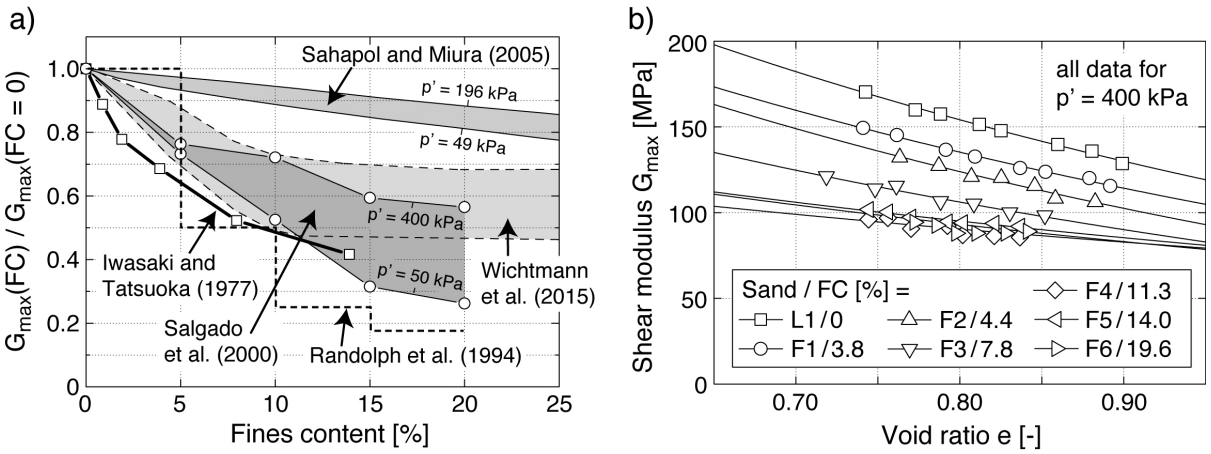

Figure 2.16: Decrease of small-strain shear modulus $G_{\max}$ with increasing fines content FC: a) results from the literature compiled by Wichtmann et al. (2015), b) data from resonant column tests of Wichtmann et al. (2015) for sands with different silty fines content (modified from Wichtmann et al., 2015).

3 Materials, experimental methods and testing program

This chapter presents the tested materials, test devices, experimental methods and the testing program used to assess the influences of the initial fabric (sample preparation method), stress anisotropy, particle shape and grain size distribution curve on the small-strain stiffness of granular soils.

The adopted soils are described along with their particle characteristics and index properties.

A conventional triaxial cell was utilized to apply both isotropic and anisotropic stress states under both drained and undrained conditions. This cell was further modified to accommodate piezoelectric elements for measurements of wave velocities in both vertical and horizontal directions within the specimens. A measuring system was established to record the travel times of compression and shear waves. Prior to conducting the tests, calibration and validation of the apparatus were performed to ensure measurement accuracy.

Subsequently, the experimental procedures will be detailed. The two applied sample preparation methods, each resulting in distinct initial fabric conditions, will be outlined.

Finally, the experimental program including tests with different initial and loading conditions will be presented.

3.1 Adopted materials

Four granular materials with different particle shape were used in this study: 1) Hostun sand, Hs; 2) round glass beads, Gr; 3) crushed glass beads, Gc; and 4) Rhine sand, Rs. The latter three materials were tested with two different specially mixed grain size distribution curves, with uniformity coefficients of $C_u = 1.25$ or 5, respectively. All tested materials had a similar mean grain size d_{50}.

The physical properties and the particle characteristics of the materials adopted are presented in the following sections. The grain size distribution curves, the specific gravities, G_s, and the minimum and maximum void ratios, $e_{\min}$ and $e_{\max}$, of the materials adopted were determined in accordance with the German standard codes DIN 18123, DIN 18124 and DIN 18126.

3.1.1 Hostun sand (Hs)

Hostun sand, Hs, is a quartz sand that has been also tested in several previous studies (Fioravante, 2000; Schanz & Vermeer, 1996; Doanh et al., 1997; Ezaoui & Di Benedetto, 2009; Sadek et al., 2007; Goudarzy et al., 2016b; Azeiteiro et al., 2017). Figure 3.1a shows a microscopic image of randomly selected particles of this sand. It can be seen that it is composed of sub-angular to angular grains. The determined grain size distribution curve of the adopted sand is presented in Figure 3.1b in comparison with the distributions from previous studies on this sand. As can be seen, it is a uniform sand with the mean grain size, d_{50}, ranging from 0.30 mm to 0.38 mm. The uniformity coefficient of the sand adopted in this study is $C_u = 1.68$. The specific gravity has been determined as $G_s = 2.65$ and the minimum and maximum void ratios as $e_{\min} = 0.67$ and $e_{\max} = 1.02$.

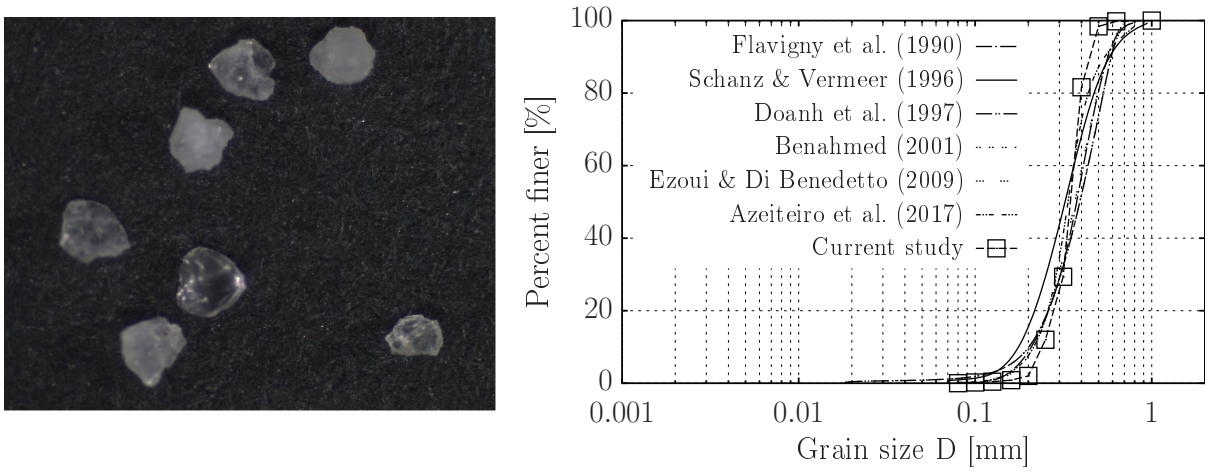

(a) (b)

Figure 3.1: Particle characteristics of Hostun sand: (a) microscope image for the analysis of particle shape; (b) grain size distribution curves in comparison with previous studies.

The physical characteristics of the adopted sand are presented in Table 3.1 in comparison with those from the previous works. It can be concluded that the Hostun sand adopted in this study has similar properties as those used in the previous works.

Table 3.1: Comparison of the properties of Hostun sand used in various studies

Reference	G_s [-]	d_{50} [mm]	C_u [-]	$e_{\min}$ [-]	$e_{\max}$ [-]
Flavigny et al. (1990)	2.65	0.30-0.35	1.70-1.90	0.62	0.96
Schanz & Vermeer (1996)	2.65	0.36	1.42	0.65	1.04
Doanh et al. (1997)	2.65	0.38	1.90	0.62-0.65	0.96-1.04
Benahmed (2001)	2.65	0.33-0.38	1.60-1.90	0.62	0.96
Sadek et al. (2007)	2.65	0.34	1.50	0.62	0.96
Ezaoui & Di Benedetto (2009)	2.65	0.36	1.42	0.62	0.96
Goudarzy et al. (2016b)	2.65	0.35	1.68	0.67	1.02
Azeiteiro et al. (2017)	2.64	0.33	1.40	0.66	1.00
Hostun sand (current study)	2.65	0.35	1.68	0.66	1.02

To determine the particle shape parameters of the Hostun sand, 100 particles were randomly selected for the image analysis. It is well known that the accuracy of the analysis is related to the quality of the images. For this reason, a microscope (Leica S6D, available at the Faculty of Mechanical Engineering, Ruhr-Universität Bochum) was adopted to take the images with a high quality. Figure 3.2a shows an original microscope image with four particles of Hostun sand. It is necessary to keep the individual particles apart from each other to prevent errors in the calculation of the shape parameters. A suitable color was chosen as the background in order to obtain the clear outline of the particles. The noise was erased through the open-source software ImageJ (e.g. Kumara et al., 2012; Ferreira & Rasband, 2012) before converting the image into the binary form, as seen in Figure 3.2b. The grain shape analysis was performed by using a MatLab script (code modified after Zheng & Hryciw, 2015).

The parameters sphericity, S, and roundness, R, of each particle were determined. It can be seen in Figure 3.2c that the four particles were individually analyzed. The software can export a file containing the shape parameters of each particle. The average values of the shape parameters, $S = 0.75$ and $R = 0.40$, were calculated based on the data obtained for the 100 particles. The regularity factor according to Cho et al. (2006), ρ, which is the mean value of S and R, is $\rho = 0.58$ for the Hostun sand. Although S and R should

generally be determined in terms of three dimensions, two-dimensional definitions were adopted in the current study due to the limitation of the microscope that can only take a top view on particles. The same procedure of grain shape analysis was also carried out on the other tested materials, i.e. the round glass beads, the crushed glass and the Rhine sand.

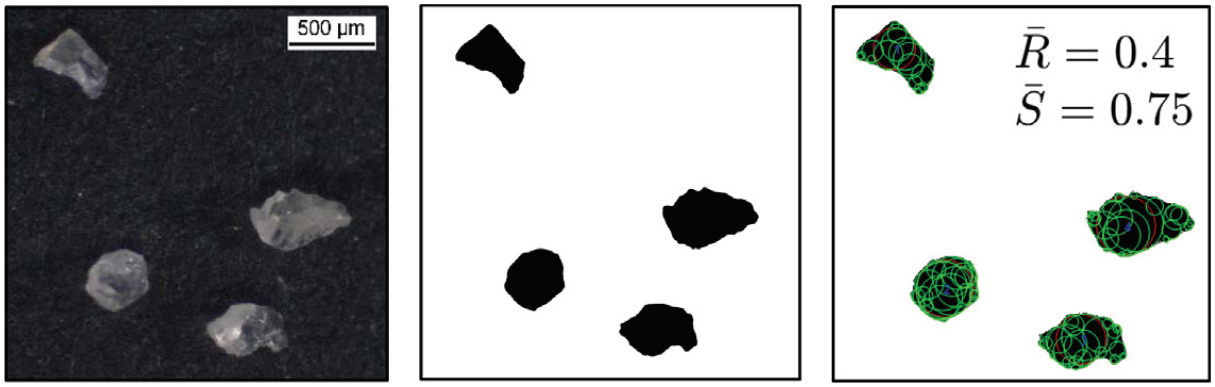

(a) Original image (b) Binary image (c) Analyzed image

Figure 3.2: Processing of microscopic images of Hostun sand to determine the particle shape parameters, S and R; (a) original image of Hostun sand obtained through the microscope, (b) conversion into binary form, (c) image after analysis procedure was applied (Sarkar et al., 2020).

3.1.2 Round Glass beads (Gr)

The round glass beads with grain sizes ranging from 0.12 mm to 6.50 mm were purchased from a local company (Mühlmeier GmbH). The main minerals of the glass beads are silica, sodium oxide, calcium oxide, aluminum oxide, and magnesium oxide. The specific gravity, G_s, of this material is 2.54.

The purchased glass beads were separated by particle size using sieves with the mesh sizes of 0.063, 0.12, 0.2, 0.25, 0.32, 0.4, 0.5, 0.63, 0.71, 0.8 and 1.0 mm. After sieving, the glass beads of each grain size were thoroughly washed over the sieve for separating the finer particles and oven-dried at 105°C. Then two mixtures with the same mean grain size of $d_{50} = 0.45$ mm, but two different uniformity coefficients of $C_u = 1.25$ and 5.0, respectively, were prepared. Figure 3.3b shows the grain size distribution curves of the mixtures determined from a final sieve analysis, with the solid and dashed lines corresponding to

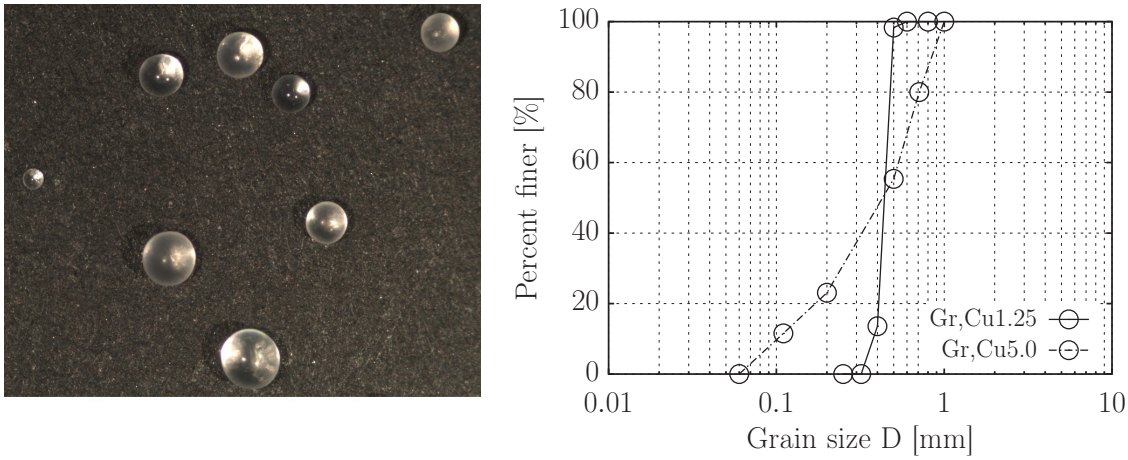

(a) (b)

Figure 3.3: Particle characteristics of the round glass beads adopted: (a) microscope image; (b) grain size distribution curves of the two mixtures.

the mixtures with $C_u = 1.25$ and 5.0, respectively. The two curves intersect at the point of mean grain size, $d_{50} = 0.45$ mm.

The minimum and maximum void ratios, $e_{\min}$ and $e_{\max}$, were determined as 0.58 and 0.74 for the mixture with $C_u = 1.25$, and as 0.38 and 0.53 for the mixture with $C_u = 5.0$. It can be seen that the $e_{\min}$ and $e_{\max}$ values of the mixture with $C_u = 1.25$ are both about 0.2 higher than those of the mixture with $C_u = 5.0$.

Finaly, 100 particles randomly picked up from each mixture were photographed with the microscope. An example for the particles with different sizes is shown in Figure 3.3a. The microscopic images were analyzed following the procedure introduced in Section 3.1.1 to determine the shape characteristics of the two mixtures. The average roundness, R, and sphericity, S, are 0.90 and 0.90, respectively. Thus, also regularity is $\rho = 0.90$.

3.1.3 Crushed glass (Gc)

To obtain angular particles, the round glass beads supplied by the same company (Mühlmeier GmbH) were crushed using a Los Angeles abrasion machine. Similar to the round glass beads, the crushed glass particles were separated and washed through a set of sieves with the mesh size ranging from 0.063 mm to 1.0 mm. After oven-drying of the clean particles at 105°C, they were mixed to obtain the same two grain size distribution curves already adopted for the round glass beads. Figure 3.4b shows these grain size distribution

curves with the same mean grain size of d_{50} = 0.45 mm, but two different uniformity coefficients of C_u = 1.25 and 5.0.

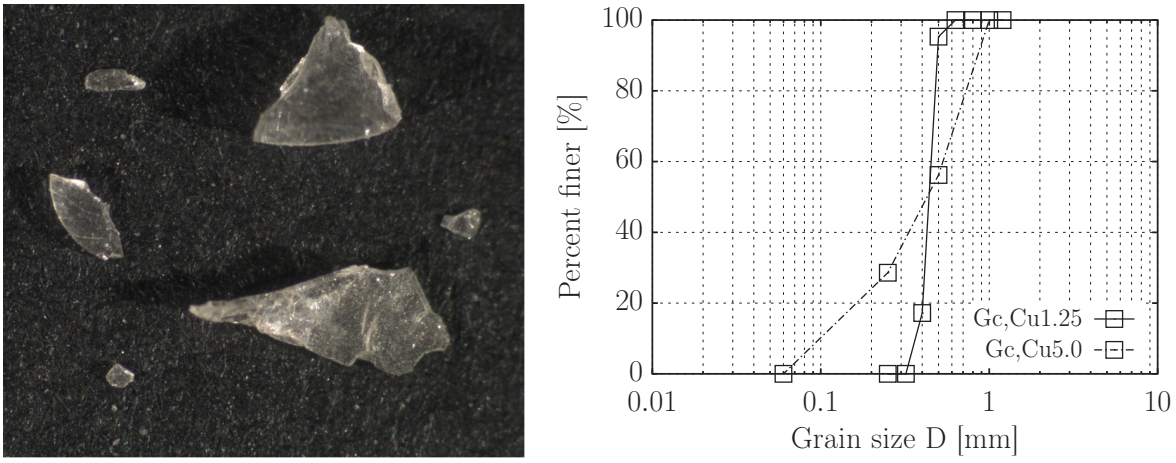

(a) (b)

Figure 3.4: Particle characteristics of the crushed glass adopted: (a) microscope image; (b) grain size distribution curves of the two mixtures.

The $e_{\min}$ and $e_{\max}$ values of the mixture with C_u = 1.25, are 0.68 and 1.15, respectively, while for the mixture with C_u = 5.0 values of 0.50 and 1.03 were determined. Similar to the round glass beads, the $e_{\min}$ and $e_{\max}$ values for C_u = 1.25 are both larger than those for C_u = 5.0.

To determine the shape parameters, the analysis was carried out on 100 particles randomly selected from each mixture. The microscopic image of the crushed glass particles in Figure 3.4a clearly shows that the particles are angular. The average values of roundness, R, sphericity, S, and regularity, ρ, of the crushed glass are 0.60, 0.30 and 0.45, respectively. These values are evidently much lower than those of the round glass beads.

3.1.4 Rhine sand (Rs)

Rhine sand is a natural quartz sand with specific gravity of 2.65. Two mixtures of the Rhine sand were prepared following the same procedure as described for the round glass beads and the crushed glass. The resulting grain size distribution curves with d_{50} = 0.48 mm and C_u = 1.25 and 5.0, respectively, are presented in Figure 3.5b.

The minimum and maximum void ratios, $e_{\min}$ and $e_{\max}$ were determined as 0.57 and 0.90 for the mixture with C_u = 1.25, while values of 0.47 and 0.83 were obtained for C_u = 5.0.

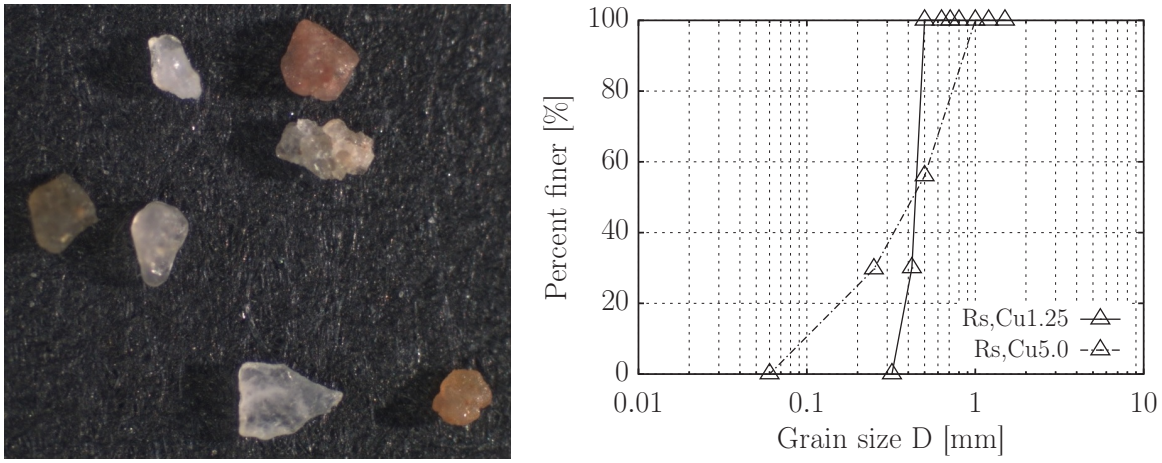

(a) (b)

Figure 3.5: Particle characteristics of the Rhine sand adopted: (a) microscope image; (b) grain size distribution curves of the two mixtures.

Also for the natural sand the minimum and maximum void ratios decrease with increasing uniformity coefficient.

The Rhine sand is adopted as a material with the shape parameters lying between the round glass beads and the crushed glass. Figure 3.5a shows an example of a microscopic image of the particles of the Rhine sand. For each mixture of the Rhine sand, 100 particles were randomly picked up to determine the shape parameters. The average values of roundness, R, and sphericity, S, were determined as 0.76 and 0.44, respectively, leading to a regularity of $\rho = 0.60$.

3.1.5 Summary of the adopted materials

Figure 3.6 summarizes the grain size distribution curves of the materials adopted, i.e. 1) Hostun sand, Hs; 2) round glass beads, Gr; 3) crushed glass beads, Gc; and 4) Rhine sand, Rs. Hostun sand was used to study the effect of the sample preparation method and stress anisotropy on the small-strain elastic stiffness of granular materials. Unfortunately, for Hostun sand it is impossible to produce two mixtures with different uniformity coefficients of $C_u = 1.25$ and 5.0 due to limitations in the range of grain sizes. For each of the three other materials two different grain size distribution curves with the same mean grain size but different uniformity coefficients $C_u = 1.25$ or 5 were tested. Figure 3.6 reveals that the mixtures of the three different materials with a given C_u posses very similar grain size distribution curves.

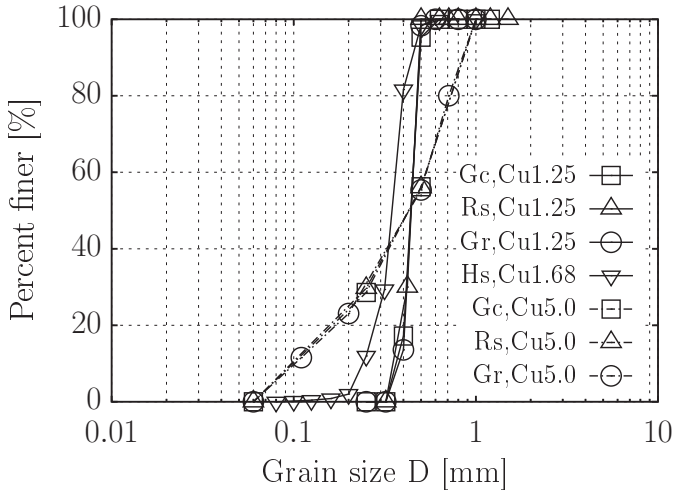

Figure 3.6: Grain size distribution curves of the materials adopted.

The physical properties, index quantities and shape parameters of the various materials adopted in this study are summarized in Table 3.2. Furthermore, the diagrams in Figure 3.7 present the minimum and maximum void ratios as well as the difference between the maximum and the minimum void ratio as functions of the regularity, distinguishing the materials with different uniformity coefficients by empty or filled symbols. Evidently, as already mentioned above, $e_{\min}$ and $e_{\max}$ decrease with increasing uniformity coefficient, while the difference $e_{\max} - e_{\min}$ is only slightly affected by C_u. Additionally, the diagrams show a clear trend for $e_{\max}$ and $e_{\max} - e_{\min}$ to decrease with an increase in the regularity, while this reduction is only moderate for $e_{\min}$.

3.2 Test devices adopted

There are two sets of experimental equipments combined in this research. A conventional triaxial device with a load frame and a pressure cell was used to apply the desired stress states under drained or undrained conditions. Furthermore, a measuring system using the piezoelectric element technique was set up to determine the velocities of elastic waves propagating in various directions in the triaxial specimen. The details of these devices will be described in the following subsections.

Table 3.2: Summary of physical properties, index quantities and particle shape parameters of the four materials adopted

Material	d_{50} [mm]	C_u [-]	$e_{\min}$ [-]	$e_{\max}$ [-]	$e_{\max} - e_{\min}$ [-]	G_s [-]	R [-]	S [-]	ρ [-]
Crushed glass	0.45	1.25	0.68	1.15	0.47	2.54	0.30	0.60	0.45
(Gc)		5.0	0.50	1.03	0.53				
Rhine sand	0.48	1.25	0.57	0.90	0.33	2.65	0.44	0.76	0.60
(Rs)		5.0	0.47	0.83	0.36				
Hostun sand (Hs)	0.35	1.68	0.66	1.02	0.36	2.65	0.4	0.75	0.58
Round glass beads	0.45	1.25	0.58	0.74	0.16	2.54	0.90	0.90	0.90
(Gr)		5.0	0.38	0.53	0.15				

3.2.1 Triaxial device

Figure 3.8 shows the triaxial device used for the current study. The device is available in the laboratory of the Chair of Soil Mechanics, Foundation Engineering and Environmental Geotechnics at Ruhr-Universität Bochum.

In the triaxial cell, specimens having a diameter of 100 mm and a height of 200 mm are sealed between the enlarged top and bottom caps with a membrane and double o-rings on each side, as seen in Figure 3.8. The membrane used in the tests of this study were made of latex and had a thickness of 0.7 mm.

A linear variable displacement transducer (LVDT), denoted as (b) in Figure 3.8, is externally mounted on the load piston, denoted as (a) in Figure 3.8, to measure the changes in the height of the specimen.

An internal load cell is located below the bottom plate to measure the vertical load applied to the specimen. For the tests under drained conditions, a load cell with a capacity of 10 kN was used to obtain more accurate measurements. For the tests under undrained conditions carried out particularly on dense specimens, a load cell with a capacity of 20 kN was employed due to the high axial strength caused by the development of negative excess pore water pressures.

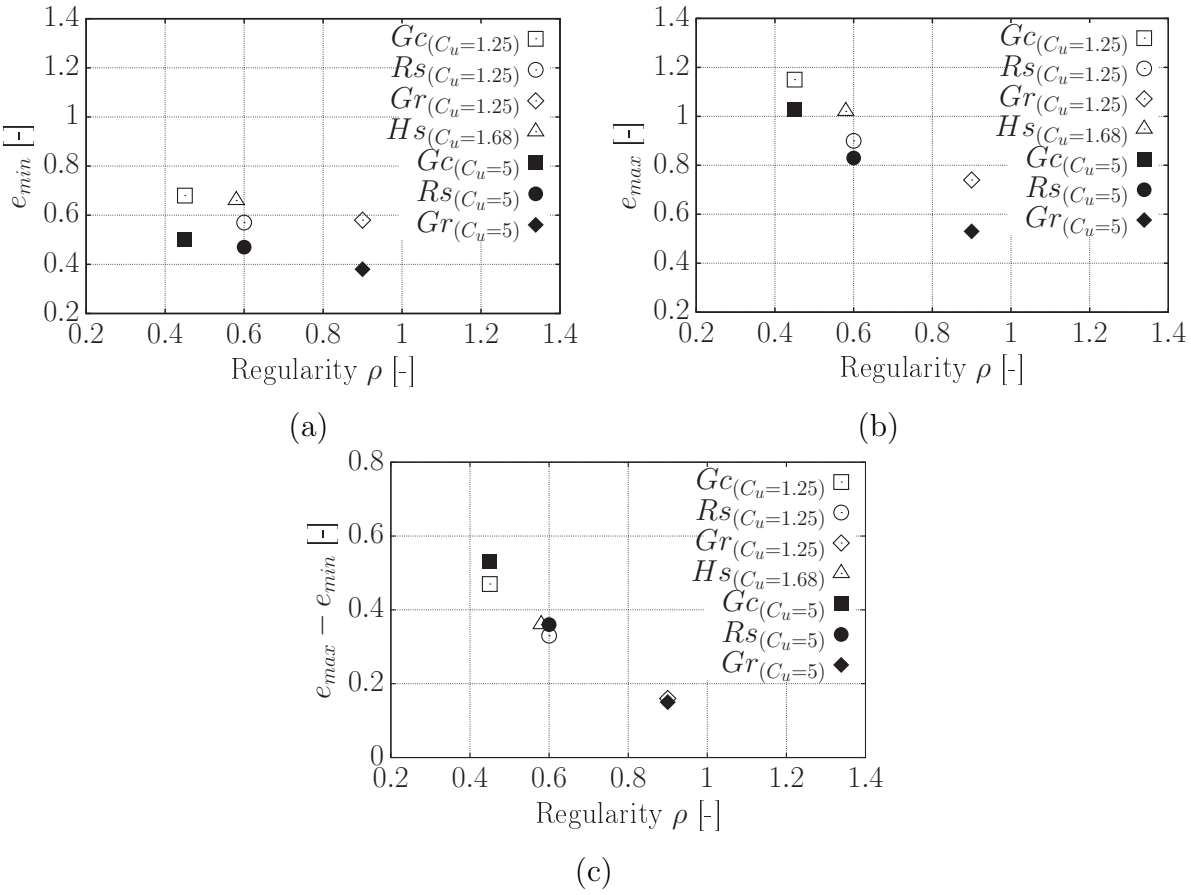

Figure 3.7: Influence of regularity and uniformity coefficient on (a) minimum void ratio $e_{\min}$, (b) maximum void ratio $e_{\max}$ and (c) the difference $e_{max} - e_{min}$.

The back pressure is monitored using a sensor connected to the drainage system at the bottom of the specimen, see (c) in Figure 3.8. Another sensor, termed (d) in Figure 3.8, is employed to measure the cell pressure. The pressure cell is filled with water, letting an air cushion of 1 to 2 cm at the top. The cell pressure is applied as air pressure to this cushion using the air pressure supply system, see (e) in Figure 3.8.

Since all tests have been conducted on specimens being fully saturated with de-mineralized and de-aired water, the change in volume of the specimens during the consolidation phase or the drained shearing can be measured by the volume of water flowing in or out of the specimen. For that purpose the drainage lines from the top and bottom caps are connected to a burette system. One burette is connected to the drainage system, thus showing a changing water level corresponding to volume changes of the specimens, while the water level in a second reference column is kept constant. The volume changes are

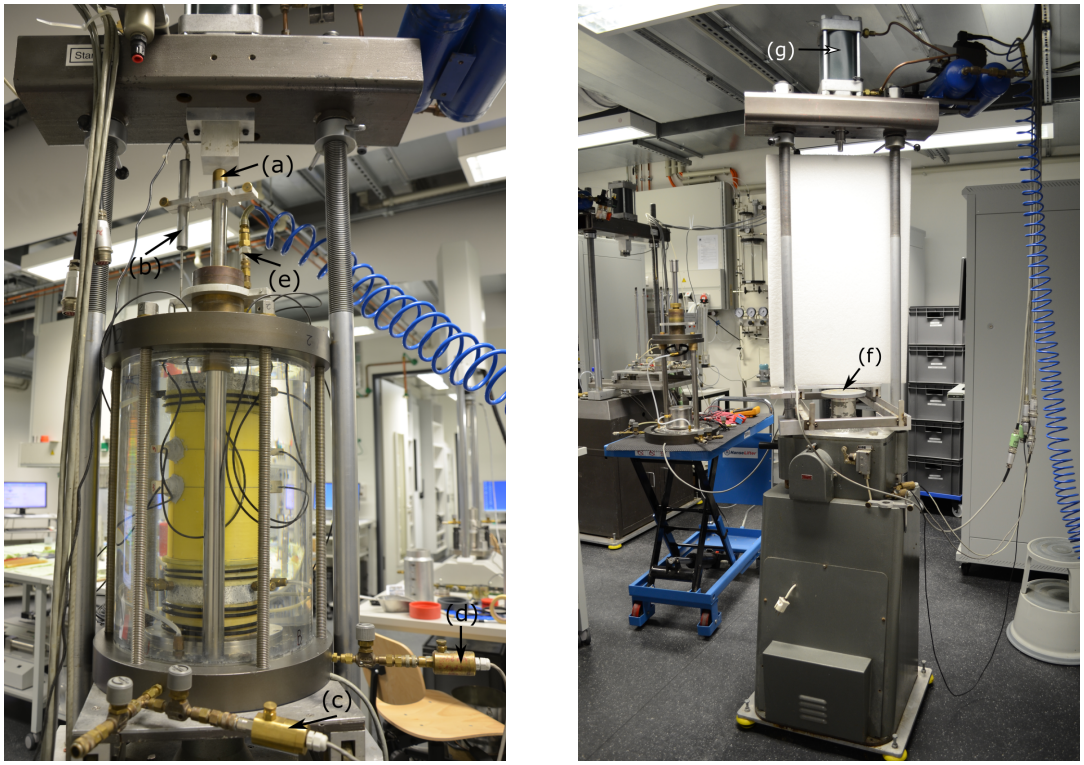

Figure 3.8: Photo of the adopted triaxial device (left) and the loading frame (right): (a) load piston, (b) linear variable displacement transducer, (c) back pressure sensor, (d) cell pressure sensor, (e) cell pressure supply, (f) movable plate of the loading frame for strain-controlled tests, and (g) pneumatic loading cylinder for stress-controlled loading.

calculated from the electrical signal of a differential pressure transducer which is connected to both burettes.

The compression load can be applied to the specimens by the loading frame shown in Figure 3.8 (right) using either strain or stress control. In the strain control method, the movable plate, see (f) in Figure 3.8, can lift the cell upwards automatically or manually with a given rate which can be controlled through a certain couple of gears. In the stress control method, the vertical load is applied through a pneumatic loading cylinder, see (g) in Figure 3.8, under the control of a computer. Both the strain and the stress control method were used in the current study.

The appropriate calibrations of the LVDT, the load cell, the pressure sensors and the differential pressure transducer for volume change measurements were done precisely before performing the experiments. Their calibration characteristics are presented in Table 3.3. It is worth noting that the measuring system for the volume change was calibrated under

a pressure of 200 kPa which is also adopted as the back pressure for consolidation and shearing under drained conditions.

Table 3.3: Calibration characteristics of the sensors adopted in the triaxial device

Transducer	Approx. range	Resolution	Type of regression	Coeff. of determin.
LVDT	± 25 mm	2.50 μm/mV	Linear	1.00
Load cell (drained)	0 - 10 kN	1.00 N/mV	Linear	1.00
Load cell (undrained)	0 - 20 kN	2.00 N/mV	Linear	1.00
Cell pressure sensor	-0.80 - 7 bar	0.10 kPa/mV	Linear	1.00
Back pressure sensor	-0.80 - 6 bar	0.10 kPa/mV	Linear	1.00
Diff. pressure transd.	0 - 201.84 cm^3	20.184 mm^3/mV	Linear	1.00

3.2.2 Measuring system using piezoelectric element technique

In this subsection, the electric measuring system adopted to determine the wave velocities is introduced. This includes the components and the calibration of the system. Shear waves (S waves) were measured in both the vertical and the horizontal directions within the sample. Compression waves (P waves) were measured only in the vertical direction.

3.2.2.1 Manufacturing of bender elements

The compression elements for the measurement of the P waves were already available at the start of this research. The bender elements for the measurement of the S waves in the vertical and horizontal directions were newly manufactured, which is described for the elements used for the vertical measurements in the following.

The bender elements were purchased from the company PI Ceramic GmbH. It can be seen in Figure 3.9a and b that the elements measure $18 \times 10 \times 1$ mm in length, width and thickness, respectively.

In order to conduct bender element tests on saturated specimens, the elements were isolated from water by being coated with epoxy. Figure 3.9c shows the air-drying process of the coated elements.

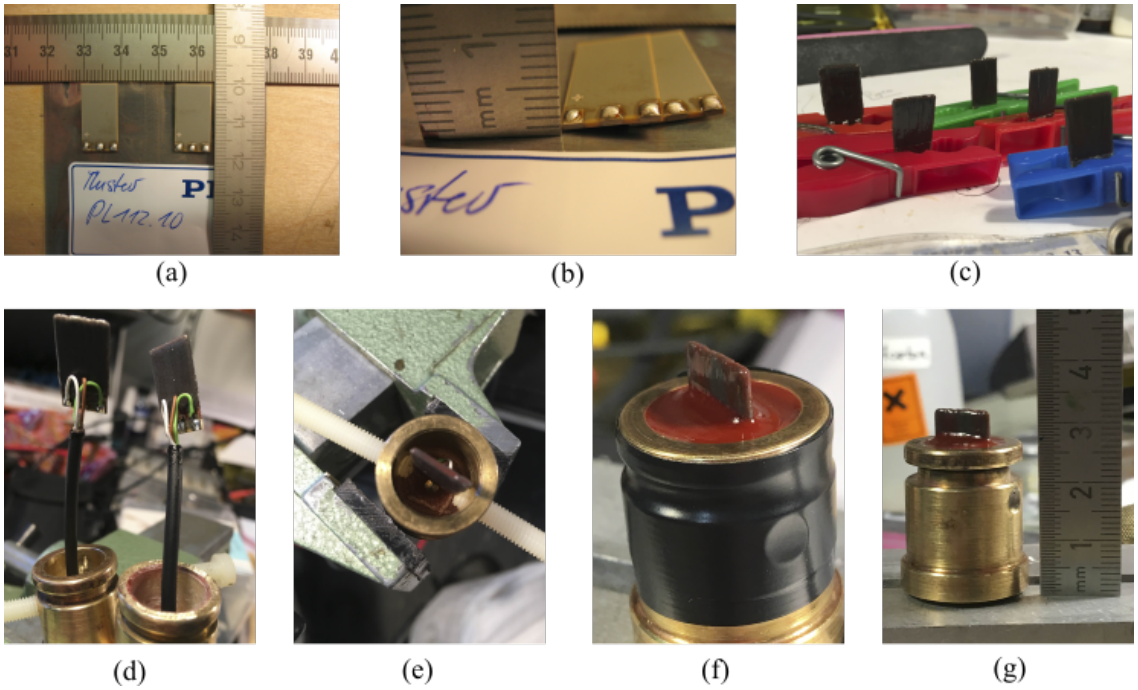

Figure 3.9: (a) Length and width of bender elements, (b) thickness of bender elements, (c) bender elements coated with epoxy, (d) elements connected with a waterproof cable through the bottom of a casing, (e) an element fixed in a casing with two plastic screws, (f) filling the casing with resin, and (g) completed sensor which will be burried in the top or bottom caps of the triaxial device.

When the epoxy coating was solidified, waterproof cables were welded to the elements through a hole in the bottom of the brass casings, as shown in Figure 3.9d. Then, the coated elements were carefully placed into the casings and held by two plastic screws through the holes in the wall of the casing (Figure 3.9e). With the two screws, the position of the bender element could be adjusted to keep it in the vertical direction and to achieve the desired penetrating length, $l_{e,i}$ (the subscript i denotes the number of the bender element), which is the part of the element that can freely move to excite a wave and is in contact to the soil particles.

Filling resin was divided into two steps. At first, the resin was injected into the space below the screws. When the elements had been fixed with the solidified resin, the screws were removed and the holes in the wall of the casing were covered with black tape, as shown in Figure 3.9f. Then, the resin could be filled into the upper space. Figure 3.9g shows the completed bender element sensor with a penetrating length of 5 mm, ready to be incorporated into the end caps of the triaxial cell.

3.2.2.2 Measuring system

All piezoelectric elements were connected with waterproof cables to an electric measuring system which is composed of a computer with the software LabVIEW, two amplifiers, and a data logger. Figure 3.10a shows a schematic sketch of the electric measuring system. In this system, the computer overtakes the role of the function generator and the oscilloscope. A digital signal generated by the computer was translated into an electric signal by the data logger and was enhanced by the amplifier. Then, the electric signal forced the piezoelectric element on one side of the specimen to excite a body wave which was detected by the piezoelectric element on the opposite side. The receiving signal was enhanced by the charge amplifier and was digitized by the data logger for the computer reading.

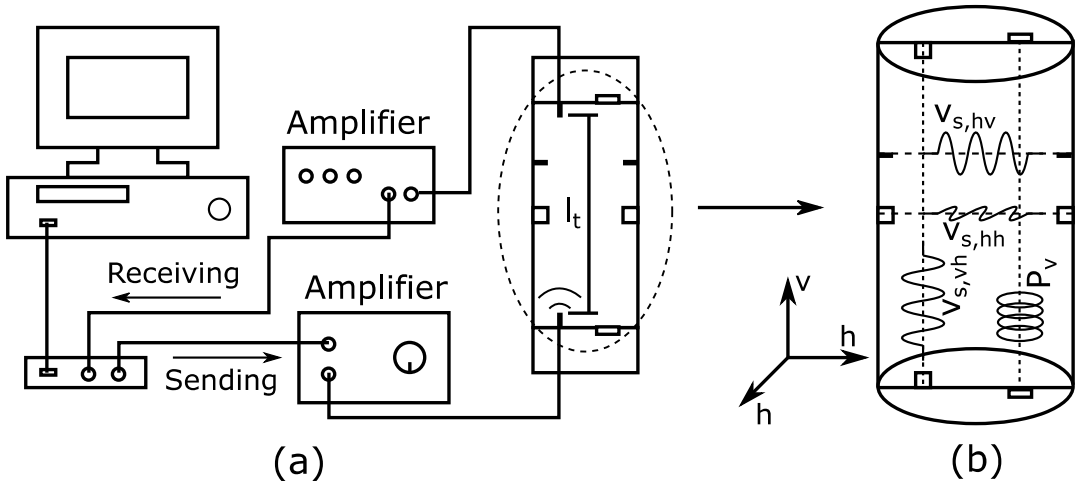

Figure 3.10: Schematic sketch of (a) the electric measuring system adopted in this research work and (b) the arrangement of the piezoelectric elements at the triaxial specimens. The single subscript before the comma denotes the type of waves, where p is a compression wave, and s is a shear wave. The first and second subscripts after the comma show the propagation and polarization directions of waves, respectively. The vertical direction is denoted as v, and the horizontal direction is denoted as h.

As shown in Figure 3.10b bender elements integrated into the base and the top cap of the specimen were used to measure the shear wave velocity $v_{s,vh}$ (vertical propagation, horizontal polarization). Likewise, compression elements in the end caps gave the P wave velocity $v_{p,v}$ in the vertical direction. Bender elements mounted on the sides of the sample, with the element penetrating the membrane, were used to measure the shear wave velocities $v_{s,hh}$ (horizontal propagation, horizontal polarization) and $v_{s,hv}$ (horizontal prop-

agation, vertical polarization). For $v_{s,hh}$ the bender element must be oriented vertically, while for $v_{s,hv}$ a horizontal mounting is necessary.

Regarding the notation of the waves, the single subscript before the comma denotes the type of waves, where p is a compression wave, and s is a shear wave. The first and second subscripts after the comma show the propagation and polarization directions of waves, respectively. The vertical and horizontal directions are denoted as v and h, respectively. Since the propagation and polarization directions of compression waves are identical, there is only one subscript after the comma for them.

For a given couple of bender or compression elements, the sent and received signals were both saved on the computer, and were displayed on the same time line in order to determine the time difference between them. This period is called the total time, t_{total}, which consists of two components, the traveling time, t_{tr}, and the delay time, t_{delay}, as can be seen in Equation 3.1. The t_{tr} is the time a wave needs to be propagated over a certain distance, and will be used for the calculation of the wave velocity. The t_{delay} is a response time of the entire system, and should be subtracted from t_{total}. The determination of t_{delay} is explained in the next subsection.

$$\begin{aligned} t_{\text{total}} &= t_{\text{tr}} + t_{\text{delay}} \\ t_{\text{tr}} &= t_{\text{total}} - t_{\text{delay}} \end{aligned} \tag{3.1}$$

For the compression elements the traveling distance l_t is identical to the actual specimen height h, since the piezoelectric elements are fully incorporated into the end plates. For the bender elements, the tip-to-tip distance is set into approach for l_t, as shown in Figure 3.10a. Thus, the penetrating length, $l_{e,i}$, of each bender element must be measured and recorded individually. The distance l_t is obtained by subtracting the $l_{e,i}$ of a couple of bender elements, denoted by $l_{e,1}$ and $l_{e,2}$ here, from the actual specimen height h:

$$l_t = h - l_{e,1} - l_{e,2} \tag{3.2}$$

The shear wave velocity v_s or the compression wave velocity v_p are then obtained from:

$$v_{s/p} = \frac{l_t}{t_{tr}} \tag{3.3}$$

3.2.2.3 Determination of the delay time t_{delay}

The delay time t_{delay} is obtained by measuring the total time t_{total} when the couple of elements is brought in direct contact to each other. In that case $t_{\text{delay}} = t_{\text{total}}$ applies,

because t_{tr} is zero. An example for such a measurement with bender elements is provided in Figure 3.11c. In the present study the t_{delay} for all bender elements mounted in the vertical and horizontal directions was determined as 2×10^{-5} seconds in that way. For the compression elements similar values for t_{delay} were determined.

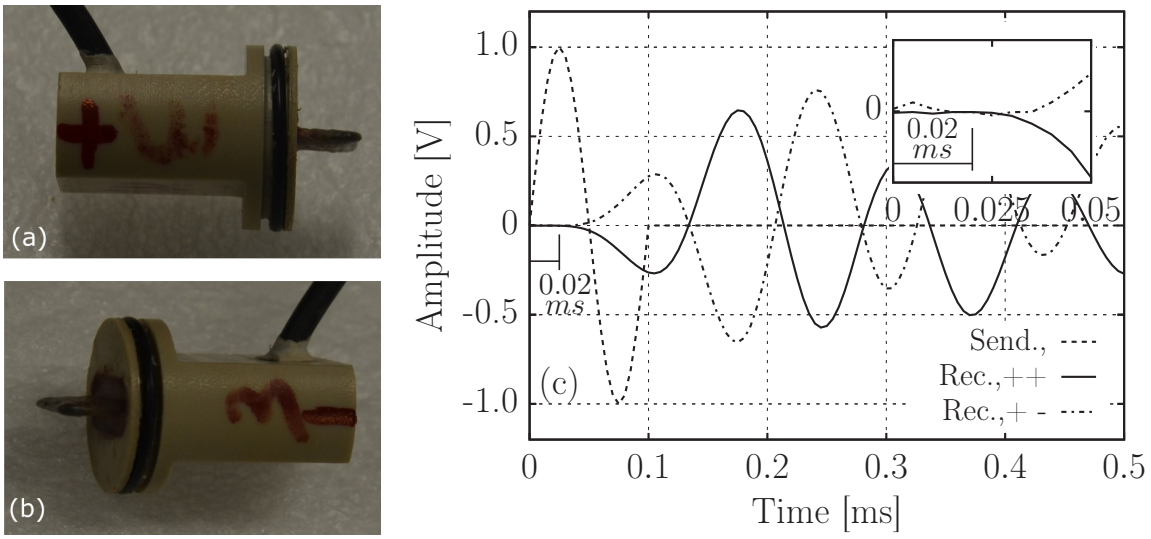

Figure 3.11: (a) A "+" mark on one side of a bender element, (b) A "-" mark on the opposite side of the same element, and (c) an example of the determination of the time delay t_{delay} for a couple of bender elements mounted with two different collocations.

In Figure 3.11c, there are two recorded received signals. They are symmetric along the x-axis because the two tests were conducted on the same couple of elements with different setup. The goal of the tests was to reveal the effect of the installation of the elements on the received signals. Before the tests, one side of the couple of elements was marked with "+", and the other side was marked with "-", as shown in Figure 3.11a and b. In the first test, the elements were mounted with the same mark on the same side. The received signal is shown as a solid line denoted as "++" in the figure, and its first deflection starts downwards. In the second test, the elements were mounted with different marks on the same side. The received signal is shown as a dashed line termed "+-", and its first deflection starts upwards. It can be concluded that the two collocations have no impact on the measured t_{delay}, but can cause the different starting directions of the first deflection of the received signals. This calibration has been done for every couple of elements. It can help determining the starting point of the received signals in case of the measurements on the triaxial specimens.

The measured t_{delay} for each couple of bender elements was validated by means of additional measurements on aluminium and plastic rods with a diameter of 5 mm and a length of 200 mm. The rods had notches on boths sides to host the tips of the bender elements. The measured t_{total} and the calculated shear modulus $G_{\max}$ of the two materials are presented in Table 3.4. The results are in good agreement with the standard values of the two materials.

Table 3.4: Validation of t_{delay} using measurements on aluminium and plastic samples.

Sample	diameter [mm]	length [mm]	t_{total} [μs]	t_{delay} [μs]	t_{tr} [μs]	v_s [m/s]	ρ [kg/m^3]	$G_{\max}$ [GPa]
Aluminium	5	200	85	20	65	3077	2700	25.6
Plastic	5	200	245	20	225	889	1400	1.1

3.2.2.4 Signal analysis

In order to obtain a signal with a good quality for the determination of the total time t_{total}, a preliminary study was performed in which different wave shapes were tested with the frequency of 10 kHz. The bender element measurements were conducted in the vertical direction on a specimen of Hostun sand at a void ratio of $e = 0.75$ and an isotropic stress state with $p' = 50$ kPa. The sent and corresponding received signals are shown in Figure 3.12. It can be seen that there is no significant difference between the received signals for the three sending signal shapes. The t_{total} for the different signal shapes were determined using the first deflection method that has been also adopted in previous works (e.g. Gajo et al. 1997, Yamashita et al. 2009, and Goudarzy et al. 2016a). The first deflection points are denoted with a black arrow in Figure 3.12. The different signal shapes show obviously the same t_{total}. Thus, the sinusoidal signal, which is often used in the previous studies (e.g. Gajo et al. 1997, Pennington et al. 2001, Leong et al. 2005, Yamashita et al. 2009, and Azeiteiro et al. 2017), was adopted in all of the experiments using bender elements in this study.

In a further preliminary test sinusoidal waves with different frequencies were used to excite the bender elements following the suggestion by Lee & Santamarina (2005). This experiment was conducted on a specimen of Hostun sand, which had a void ratio of 0.81 and was subjected to the isotropic effective stress of 200 kPa. The sending signals were sinusoidal waves with the frequencies of 5, 10 and 15 kHz. As shown in Figure 3.14a the

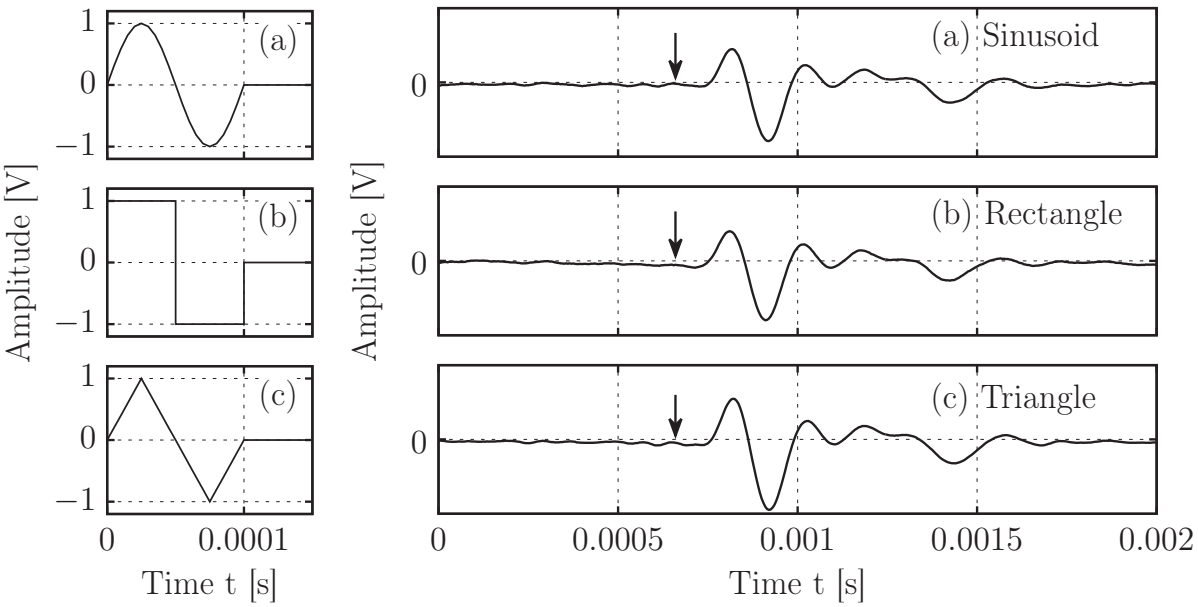

Figure 3.12: Sent (left) and received (right) signals with the frequency of 10 kHz and different signal shapes: (a) Sinusoid, (b) Rectangle, and (c) Triangle.

t_{total} was also determined with the first deflection method, as marked by arrows in that figure. The location of the arrows shows that there is no obvious difference between the detected t_{total} for the range of tested frequencies. The sinusoidal wave with the frequency of 10 kHz was chosen as the sending signal for all experiments in the present research work.

Figure 3.14b shows the recorded receiving signals from an experiment on an air-pluviated specimen of Hostun sand with the void ratio of 0.95, which was successively subjected to the effective stress states of 50, 100 and 200 kPa. The results of the bender element measurements are in good agreement to the previous studies and to the expectation, that a shear wave is propagated faster with increasing stress level.

For the P wave measurements with the compression elements excitation signals with a frequency of either 10 or 15 kHz were used.

3.2.2.5 Modification of the triaxial device for wave velocity measurements

The triaxial cell, shown in Figure 3.8, was modified to enable measurements of wave velocities in both the vertical and horizontal directions. The details of the modification are shown in Figure 3.15.

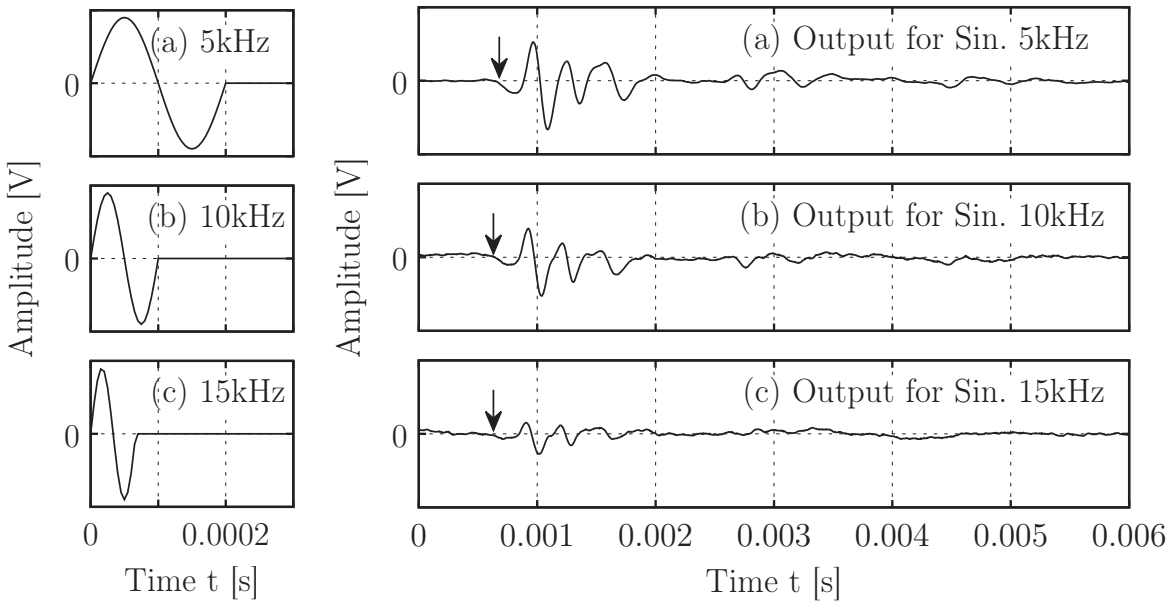

Figure 3.13: Sent (left) and received (right) signals for excitation frequencies of: (a) 5 kHz, (b) 10 kHz, and (c) 15 kHz.

The top and bottom caps mounted in this cell were modified for the installation of the compression and bender elements, as shown in Figure 3.15c. Two pairs of compression and bender elements, which can be seen in Figure 3.15d and e, were used to determine the velocities of the compressional and shear waves, $v_{p,v}$ and $v_{s,vh}$, respectively, which were propagated in the vertical direction of the specimens. As can be seen in Figure 3.15c the elements are mounted halfway between the center and the boundary of the specimen, while a porous stone of 2 cm diameter is located in the center of the end plate to allow drainage. The three white disks visible in Figure 3.15c are ceramics with a high air entry resistance, which are needed for tests on partially saturated soil samples. Since all tests of the current study have been performed on fully water-saturated samples, these ceramics are not relevant for this thesis.

In order to measure the velocities of the shear waves propagated in the horizontal direction, $v_{s,hv}$ and $v_{s,hh}$, four pieces of bender elements (Figure 3.15b) were mounted on the side surface of the specimen, as shown in Figure 3.15a. For that purpose, the front side of the bender element housing is curved, so that it smoothly adapts to the cylindrical surface of the samples with 100 mm diameter. The mounting of the horizontal elements was done when the specimen stands under vacuum. The membrane was carefully cut, the bender element was installed and the cut was sealed again using silicon. In the configuration shown in Figure 3.15a the sensors for $v_{s,hh}$ were mounted in a height of 100 mm, while

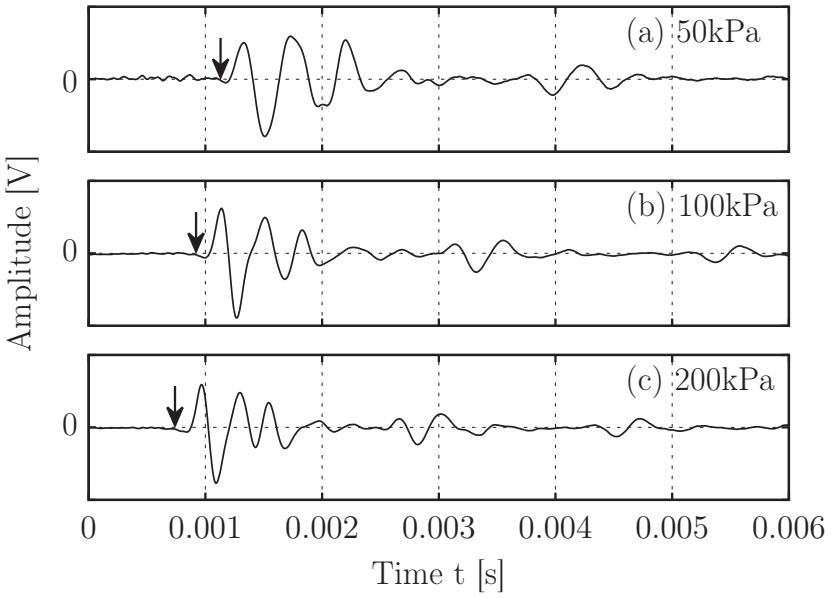

Figure 3.14: Receiving signals obtained at isotropic stress states of (a) 50 kPa, (b) 100 kPa, and (c) 200 kPa.

those for the $v_{s,hv}$ were installed at a height of 150 mm. In other configurations these heights were chosen as 50 and 150 mm.

Figure 3.16 provides more details regarding the installation of the lateral bender elements. The specimen, sealed between the top and bottom caps with a membrane and o-rings, was stabilized by a negative pore pressure of -50 kPa, as shown in Figure 3.16a. The base socket of the bender element was glued at the desired position by using silicone (Figure 3.16b). Then, the liquid latex was filled into the gap between the membrane and the socket (gray colour in Figure 3.16c). When the liquid latex was solidified, the membrane was cut through the slit in the base socket with a scalpel. Subsequently, the plug with an o-ring (Figure 3.11a) was stabbed carefully and quickly into the specimen to avoid the collapse of the specimen due to losing the negative pore pressure through the cut in the membrane, as shown in Figure 3.16d. The last step (Figure 3.16e) was to fill the liquid latex into the gap between the socket and the plug to ensure sealing.

3.3 Sample preparation

Two sample preparation methods were adopted in this research: i) the dry air pluviation (AP) method and ii) the moist tamping (MT) method. These methods are described in

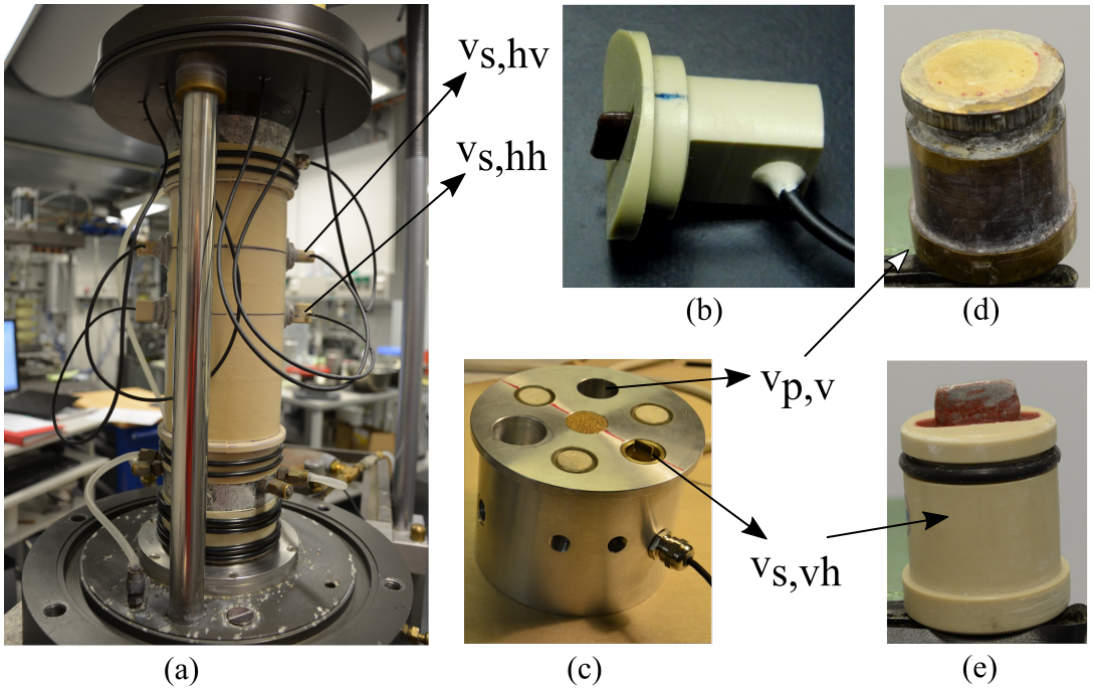

Figure 3.15: (a) Modified triaxial device employed in the present study, mounting piezoelectric elements for wave velocity measurements (b) in the horizontal direction (elements installed on the side surface of a specimen), (c) in the vertical direction (elements buried in the top and bottom caps), (d) a compression element, and (e) a bender element.

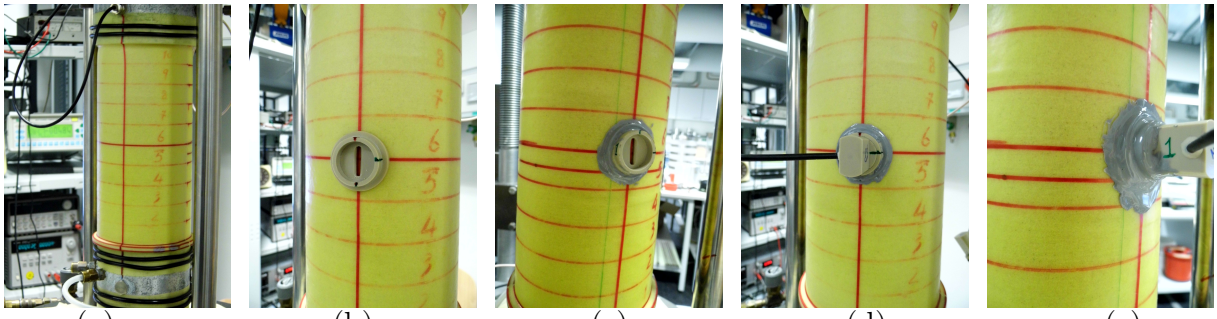

Figure 3.16: Photos showing the installation of the lateral bender elements.

detail in the following. After preparation all samples tested in this study have been fully water-saturated.

3.3.1 Air pluviation (AP) method

In this method, oven-dried sand was poured into the split mold using a funnel. The inital density of the specimens with a diameter of 100 mm and a height of 200 mm was controlled by both the nozzle size of the funnel and the dropping height from the funnel tip to the sand's surface. Smaller nozzle sizes and larger dropping heights lead to higher initial densities. The loose samples were usually prepared with zero dropping height, lifting the funnel carefully in the center of the mold, analogously to the test for the determination of the maximum void ratio $e_{\max}$.

3.3.2 Moist tamping (MT) method

In this method, oven-dried sand was mixed with a predetermined weight of water, calculated to achieve a specified water content (5%, 10%, and 15% in this study), approximately 16 hours prior to sample preparation. This ensured an even distribution of water throughout the mixture, promoting sample homogeneity. The resulting moist mixture was then placed and compacted in 10 layers within the split mold to form a specimen measuring 100 mm in diameter and 200 mm in height. Each layer was compacted by a tamper to a thickness of 20 mm to ensure uniformity along the specimen's height. The quantity of the moist mixture used for each layer was determined based on the desired density and the volume of each layer. Subsequently, the moist sand for each layer was evenly distributed within the split mold using a spoon and compacted to a height calculated based on the number of layers in the mold. Notably, building a layer at higher density requires more compaction energy than at lower density. The remaining mixture was weighed both before and after drying in the oven to confirm the water content and the mass of sand in the specimen.

3.4 Testing procedure

After preparation with a given density the specimens were stabilized by the application of a negative pore pressure of -50 kPa supplied by a vacuum. Subsequently, the vertical and horizontal dimensions of the specimen were measured to determine its initial volume. These dimensions were checked again after the bender elements were installed on the side surface of the specimen. Next the cell was assembled and filled with water. Afterwards the negative pore pressure was reduced in steps of 10 kPa up to zero, while the cell

pressure was increased in the same steps up to 50 kPa, keeping the effective stress of 50 kPa constant. During the subsequent saturation phase, the specimen was first flushed with carbon dioxide gas and then with de-aired water. The cell and back pressure were raised to values of 250 kPa and 200 kPa, respectively. The sample stayed overnight under these pressures to improve saturation. The saturation was checked on the next day by performing the B value test. A B value greater than 0.95 was regarded sufficient.

After assembling of the device and before filling the cell water, the data aquisition program of the triaxial device was activated to record the change in the height of the specimens during all steps of the experiment. Since the recorded data show a negligible change in the height of the specimen during saturation, it can be considered that the void ratio obtained after the sample preparation was not changed.

After saturation the specimens were consolidated under the given initial effective stress state. As outlined in more detail in the next subsection, the further testing procedure involved either a sequential loading along isotropic or anisotropic stress paths, or a continuous shearing under drained or undrained conditions. At certain points during the loading the wave velocities were measured along the different paths. For the calculation of the velocities, the travel lengths in the vertical and horizontal directions were updated based on the changes in the volume and height of the specimen.

3.5 Testing program

Three series of experiments were performed in this research. The first one was dedicated to the influence of initial (inherent) fabric, varied by using different sample preparation methods. The second one investigated the influence of stress-induced anisotropy. Finally, the third series was dedicated to the combined effects of grain shape and grading.

3.5.1 Experiments on the effect of the sample preparation method

To study the effect of the sample preparation method or the initial fabric, respectively, the air pluviation (AP) and moist tamping (MT) methods were both adopted to constitute loose, medium dense and dense specimens of Hostun sand. In case of the MT method also the water content during preparation was varied (w_{pre} = 5, 10 or 15 %). The specimens were subsequently consolidated under the three isotropic effective stresses of p' = 50, 100 or 200 kPa. After consolidation at each of these stress states the shear wave velocities

were measured in the vertical and horizontal directions. Subsequently, starting from p' = 200 kPa, which is considered as the initial mean effective stress, p'_0, (in most tests, p'_0 = 100 kPa in two tests), the specimens were subjected to a triaxial compression loading with a shear rate of 0.1 mm per minute under drained conditions. At the axial strain of 24%, the test was stopped after the shear wave velocity in the vertical direction had been measured again. This test series did not contain P wave measurements. The testing program is summarized in Table 3.5, including the void ratios and relative densities at the different stress levels.

An additional test (SP-14) was performed with stress-controlled loading on an air-pluviated specimen. After the specimen was consolidated under the isotropic stress of 200 kPa, the vertical stress was increased in steps of 100 kPa up to 600 kPa. At each stress stage, the wave velocities in the various directions were measured when the height and the volume of the specimen remained constant.

3.5.2 Experiments on the effect of stress-induced anisotropy

In this test series specimens of Hostun sand were prepared with different void ratios using the AP method. After the consolidation under isotropic stresses of p' = 50, 100, 200 or 300 kPa, the triaxial compression test with a shear rate of 0.1 mm per minute was started under undrained conditions to keep the volume of the specimen constant. The shear wave velocities were measured during the step-wise isotropic consolidation and during the undrained shearing. No measurements of P waves were performed in this test series. The testing program is summarized in Table 3.6.

An additional test (CU-09) was performed with stress-controlled loading on an air-pluviated specimen. After the specimen was consolidated under the isotropic stress of 200 kPa, the vertical stress was increased under undrained conditions up to the desired value σ'_1/σ'_3 = 3. When the height and the volume of the specimen remained constant, the wave velocities in various directions were measured.

3.5.3 Experiments on the effect of particle shape

In this test series specimens of the three materials with different grain shape, i.e. round glass beads (Gr), angular crushed glass (Gc) and Rhine sand (Rs) were prepared by air pluviation. For the mixtures with C_u = 5 several samples with different initial relative densities were prepared. For the mixtures with C_u = 1.25 only medium dense samples

Table 3.5: Testing program for studying the effect of the sample preparation method on Hostun sand (Hs)

No.	Preparation method	w_{pre} [%]	p'= 50 kPa		p'= 100 kPa		p'= 200 kPa		p'_0 for testing [kPa]	Drainage condition
			e [-]	D_r [%]	e [-]	D_r [%]	e [-]	D_r [%]		
SP-01	AP	0	0.957	17.5	0.952	18.9	-	-	100	Drained
SP-02	AP	0	0.760	72.2	0.758	72.8	-	-	100	Drained
SP-03	AP	0	0.975	12.5	0.971	13.6	0.962	16.1	200	Drained
SP-04	AP	0	0.882	38.3	0.879	39.2	0.873	40.8	200	Drained
SP-05	AP	0	0.812	57.8	0.810	58.3	0.805	59.7	200	Drained
SP-06	AP	0	0.762	71.7	0.758	72.8	0.756	73.3	200	Drained
SP-07	AP	0	0.698	89.4	0.698	89.4	0.698	89.4	200	Drained
SP-08	MT	5	0.990	8.3	0.985	9.7	0.983	10.3	200	Drained
SP-09	MT	5	0.908	31.1	0.905	31.9	0.889	36.4	200	Drained
SP-10	MT	5	0.839	50.3	0.836	51.1	0.832	52.2	200	Drained
SP-11	MT	10	0.767	70.3	0.766	70.3	0.765	70.8	200	Drained
SP-12	MT	15	0.968	14.4	0.962	16.1	0.953	18.6	200	Drained
SP-13	MT	15	0.792	63.3	0.790	63.9	0.786	65.0	200	Drained
SP-14	AP	0	0.899	34.9	0.898	35.1	0.894	37.4	200	Drained

Table 3.6: Testing program for studying the effect of stress-induced anisotropy on Hostun sand (Hs)

No.	Preparation method	p'= 50 kPa		p'= 100 kPa		p'= 200 kPa		p'= 300 kPa		p'_0 for testing [kPa]	Drainage condition
		e [-]	D_r [%]	e [-]	D_r [%]	e [-]	D_r [%]	e [-]	D_r [%]		
CU-01	AP	0.930	25.1	0.924	26.7	-	-	-	-	100	Undrained
CU-02	AP	0.851	46.9	0.847	47.9	-	-	-	-	100	Undrained
CU-03	AP	0.780	66.7	0.778	67.2	-	-	-	-	100	Undrained
CU-04	AP	0.922	27.2	0.918	28.3	0.911	30.4	-	-	200	Undrained
CU-05	AP	0.833	51.9	0.830	52.8	0.825	54.2	-	-	200	Undrained
CU-06	AP	0.715	84.7	0.713	85.3	0.709	86.4	-	-	200	Undrained
CU-07	AP	0.921	27.5	0.917	28.6	0.910	30.6	0.904	32.3	300	Undrained
CU-08	AP	0.732	79.9	0.730	80.5	0.727	81.5	0.724	82.2	300	Undrained
CU-09	AP	0.910	31.7	0.907	32.6	0.905	33.1	-	-	200	Undrained

were tested. After preparation the effective stress path shown in Figure 3.17 was followed using the stress control. An isotropic consolidation at stresses of $p' = 50$, 100 and 200 kPa, accompanied by measurements of the P and S wave velocities, was followed by an anisotropic loading. During that anisotropic loading phase the effective stress in the vertical direction, σ'_1, was increased in steps of 10 kPa up to 500 kPa while the effective stresses in the horizontal direction, $\sigma'_2 = \sigma'_3$, were kept constant at 200 kPa. At the deviatoric stresses, $q = \sigma_1 - \sigma_3$, of 50, 100, 200 and 300 kPa, the specimen was consolidated until there was no further change in its height and volume. At the end of the consolidation, the P and S wave velocities in the vertical and horizontal directions were measured. In Figure 3.17 the failure lines for the loose specimens of the three materials adopted are shown. It can be found that the highest deviatoric stress $q = 300$ kPa might not be reached in the tests on the loose specimens of the round glass beads. The testing program is summarized in Table 3.7.

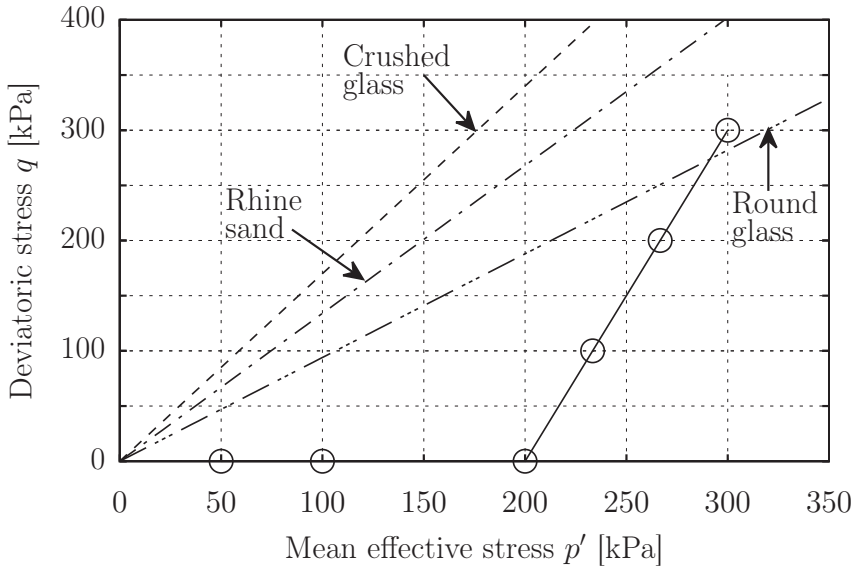

Figure 3.17: Stress path with isotropic and anisotropic loading applied on the materials with different grain shape

Table 3.7: Test program for studying the effect of particle shape on three different granular materials: Round glass beads (Gr), Crushed glass (Gc), and Rhine sand (Rs)

No.	Material	C_u	Preparation method	$p' = 50$ kPa $q = 0$ kPa		$p' = 200$ kPa $q = 0$ kPa		$p' = 300$ kPa $q = 300$ kPa		Drainage condition
				e	D_r	e	D_r	e	D_r	
		[-]		[-]	[%]	[-]	[%]	[-]	[%]	
Gr-01	Glass beads	5.0	AP	0.512	12.0	0.505	16.7	0.503	18.0	Drained
Gr-02	Glass beads	5.0	AP	0.470	40.0	0.467	42.0	0.465	43.3	Drained
Gr-03	Glass beads	5.0	AP	0.408	81.3	0.405	83.3	0.403	84.7	Drained
Gr-04	Glass beads	5.0	AP	0.378	101.3	0.376	102.7	0.375	103.3	Drained
Gc-01	Crushed glass	5.0	AP	0.877	28.9	0.859	32.3	0.840	35.8	Drained
Gc-02	Crushed glass	5.0	AP	0.742	54.3	0.730	56.6	0.716	59.2	Drained
Gc-03	Crushed glass	5.0	AP	0.699	62.5	0.688	64.5	0.677	66.6	Drained
Gc-04	Crushed glass	5.0	AP	0.594	82.3	0.587	83.6	0.581	84.7	Drained
Rs-01	Rhine sand	5.0	AP	0.772	16.1	0.754	21.1	0.736	26.1	Drained
Rs-02	Rhine sand	5.0	AP	0.699	36.4	0.687	39.7	0.673	43.6	Drained
Rs-03	Rhine sand	5.0	AP	0.545	79.2	0.539	80.8	0.534	82.2	Drained
Rs-04	Rhine sand	5.0	AP	0.505	90.3	0.500	91.7	0.497	92.5	Drained
Gr-05	Glass beads	1.25	AP	0.670	43.8	0.666	46.3	0.665	46.9	Drained
Gc-05	Crushed glass	1.25	AP	0.947	43.2	0.934	46.0	0.926	47.7	Drained
Rs-05	Rhine sand	1.25	AP	0.747	46.4	0.740	48.5	0.737	49.4	Drained

4 Experimental results

This chapter presents the results of the experiments conducted according to the procedures and programs described in Chapter 3. This chapter is divided into three sections:

The first section aims to explore how different methods of preparing the sand samples impact their mechanical properties at both small and large strains.

The second section will focus on the role of boundary conditions, particularly stress states, on the elastic stiffness of sand.

Finally, the third section will evaluate the impact of the grain shape and the grain size distribution curve on the small-strain stiffness of granular materials.

4.1 Effect of sample preparation method

To investigate the influence of the sample preparation method on the mechanical properties of Hostun sand at small and large strains, a series of compressional triaxial tests was conducted under drained conditions. The study employed two distinct specimen preparation methods, dry air pluviation (AP) and moist tamping (MT), to achieve specimens with relative densities ranging from 10% to 90%.

All specimens underwent careful saturation to ensure a B-value exceeding 0.95 and were isotropically consolidated at stress levels of 50, 100, and 200 kPa. Following each consolidation stage, shear wave velocities were measured in both vertical and horizontal directions using three pairs of bender elements. The velocities were calculated considering the specimen's height and volume change, updating the travel lengths accordingly.

Subsequently, a displacement-controlled triaxial test, consolidated and drained, was conducted under the lateral effective stress of 200 kPa, with a shear rate of 0.1 mm per minute. During the test, shear wave velocities were measured again when the axial strain reached approximately 24%, aiming to investigate v_s at the critical state. The test concluded near an axial strain of 25%.

Further details related to the experimental procedure and the testing program can be found in Section 3.5.1.

The results of this test series are presented and discussed in the following subsections.

4.1.1 Effect of sample preparation method at the small-strain level

The diagrams in Figure 4.1a, b, and c illustrate the relationship between the maximum shear modulus, $G_{\max}$, corresponding to the shear wave velocity $v_{s,vh}$, versus the void ratio, e, for specimens prepared using the moist tamping (MT) and the air pluviation (AP) techniques. The data are shown separately for the isotropic stress states of 50, 100, and 200 kPa, respectively. The results in each diagram indicate a consistent and well-known trend: as e decreases, the $G_{\max}$ increases. Furthermore, comparing the data in the three diagrams reveals the well-known increase of small-strain shear modulus with increasing mean effective stress.

In the diagrams of Figure 4.1, the solid and open points show the measured stiffness for the specimens prepared by the MT and AP methods, respectively. As can be seen, the results for both methods are located in a narrow band. For the MT preparation method, a negligible effect of the initial water content on the maximum shear modulus, $G_{\max}$, can be concluded. The results reveal small differences in the measured maximum shear modulus, $G_{\max}$, between specimens prepared using the AP and MT methods in both loose and very dense states. For instance, in the loose specimens ($D_r = 20\%, e = 0.95$) under the isotropic effective stress of 200 kPa, the $G_{\max}$ in the specimen prepared by the AP method is about 15% larger than the $G_{\max}$ in the specimen prepared by the MT method. Whereas, in dense specimens ($D_r = 76\%, e = 0.75$), the $G_{\max}$ in the specimen prepared by the AP method is about 5% less than the $G_{\max}$ in the specimen prepared by the MT method. This could be due to the applied energy to prepare dense specimens using the MT method that causes a significant inherent anisotropy in the dense specimens (this will be explained later in term of the cross anisotropy of the specimens).

The cross anisotropy of the specimens was assessed by measuring the wave velocities in the different directions. As can be seen in Figure 4.1d, the wave velocity with the vertical propagation and the horizontal polarization, $v_{s,vh}$, and the wave velocity with the horizontal propagation and the vertical polarization, $v_{s,hv}$, can be considered as the in plane wave velocities. Meanwhile, the wave velocity with the horizontal propagation and polarization, $v_{s,hh}$, is the out of plane wave velocity.

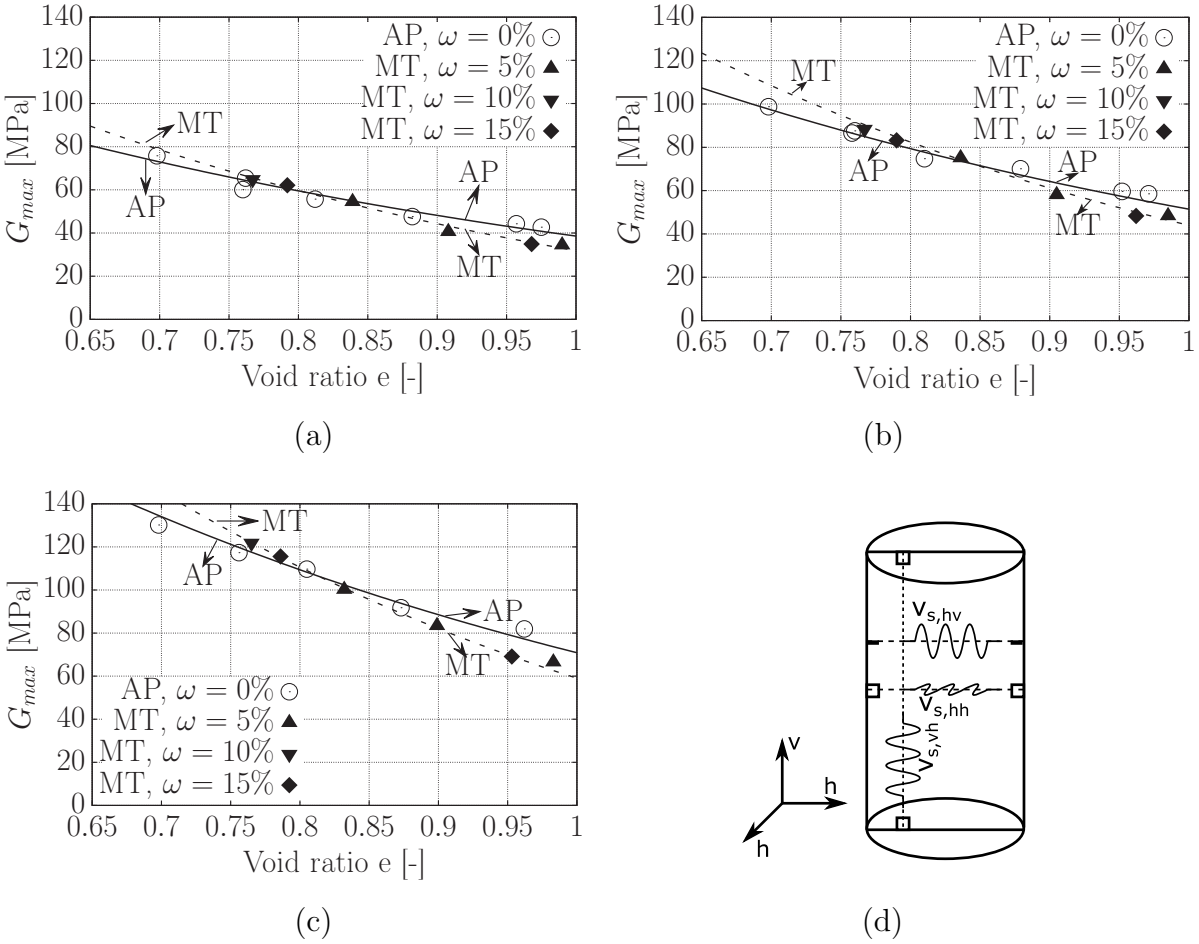

Figure 4.1: $G_{\max}$ versus void ratio for the mean effective stress p'= (a) 50 kPa, (b) 100 kPa, (b) 200 kPa; (d) A schematic sketch of the shear waves in different directions. The first and second subscripts after the comma show the propagation and polarization directions of waves, respectively. The vertical direction is denoted as v, and the horizontal direction is denoted as h.

The shear wave velocities $v_{s,vh}$ and $v_{s,hv}$ of two dense specimens prepared by the AP and MT methods are compared in Figure 4.2 to further evaluate the fabric effects. Figure 4.2a shows the measured wave velocities for the specimen prepared by the AP method with the relative density of 76% versus mean effective stress p'. As can be seen in this figure, the $v_{s,vh}$ and the $v_{s,hv}$ are almost the same. This confirms that the fabric of the dense specimens prepared by the AP method is the same in the vertical and horizontal directions. On the other hand, Figure 4.2b shows the $v_{s,vh}$ and the $v_{s,hv}$ measured for the specimen prepared by the MT method with the relative density of 72%. This figure shows some deviation

between the measured wave velocities. Figure 4.3 shows a similar presentation for the corresponding shear moduli, leading to the same conclusions.

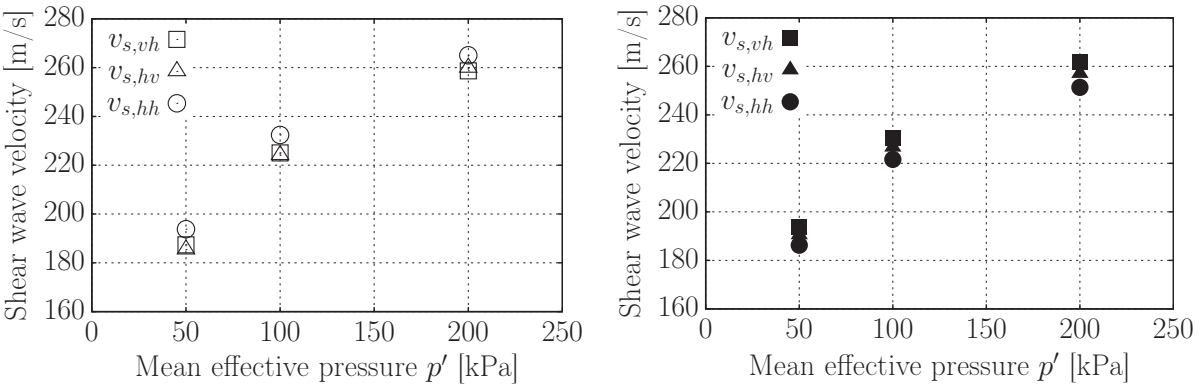

Figure 4.2: Shear wave velocities in different directions versus mean effective stress, p': (a) for the specimen prepared by the AP method at the void ratio of 0.75 ($D_r = 76\%$), (b) for the specimen prepared by the MT method at the void ratio of 0.77 ($D_r = 72\%$).

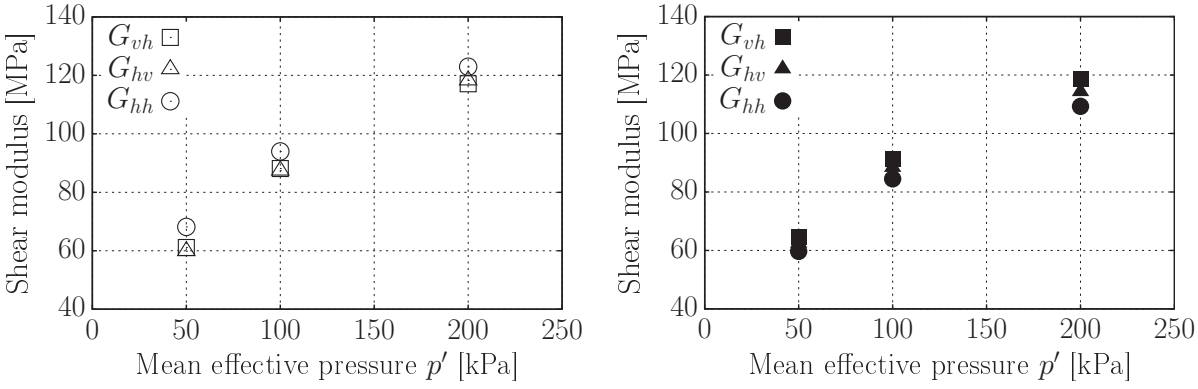

Figure 4.3: Shear moduli in different directions versus mean effective stress, p': (a) the specimen prepared by the AP method at the void ratio of 0.75 ($D_r = 76\%$), (b) the specimen prepared by the MT method at the void ratio of 0.77 ($D_r = 72\%$).

To further support these conclusions, the three wave velocities were normalized with respect to the $v_{s,vh}$ value in Figure 4.4. Figure 4.4a presents the normalized wave velocities for the specimen prepared by the AP method and shows that the $v_{s,vh}$ and the $v_{s,hv}$ obtained from this specimen are very similar. On the other hand, Figure 4.4b presents the normalized wave velocities for the specimen prepared by the MT method and shows

that the $v_{s,vh}$ is larger than the $v_{s,hv}$. This shows the effect of the sample preparation on the fabric of specimens. Furthermore, the horizontal shear wave velocity with horizontal polarization $v_{s,hh}$ is 3 to 4 % larger than $v_{s,vh}$ for the AP sample (Figure 4.4a), while $v_{s,hh}$ is 4 to 5 % smaller than $v_{s,vh}$ for the MT sample (Figure 4.4b). Figure 4.5 provides a similar presentation for the ratios of the shear moduli, showing slightly larger relative deviations.

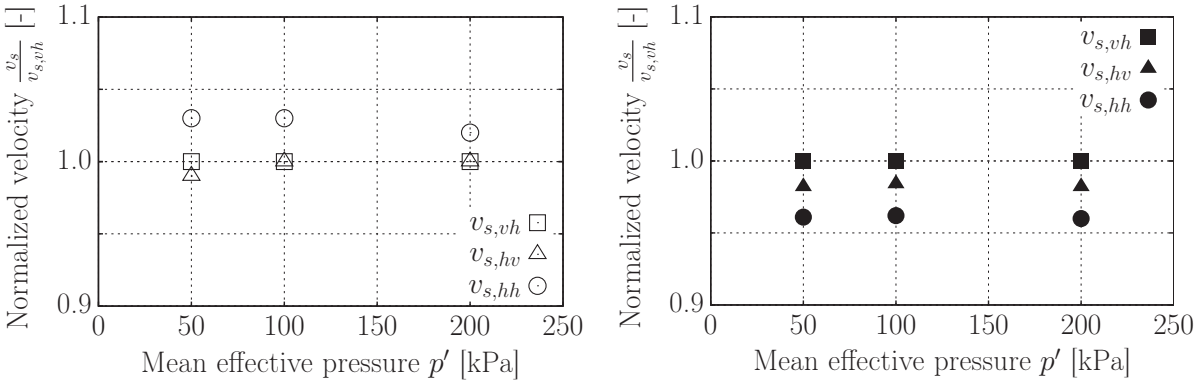

Figure 4.4: Normalized shear wave velocities, $v_s/v_{s,vh}$, versus mean effective stress, p': (a) for the specimen prepared by the AP method at the void ratio of 0.75 ($D_r = 76\%$), (b) for the specimen prepared by the MT method at the void ratio of 0.77 ($D_r = 72\%$).

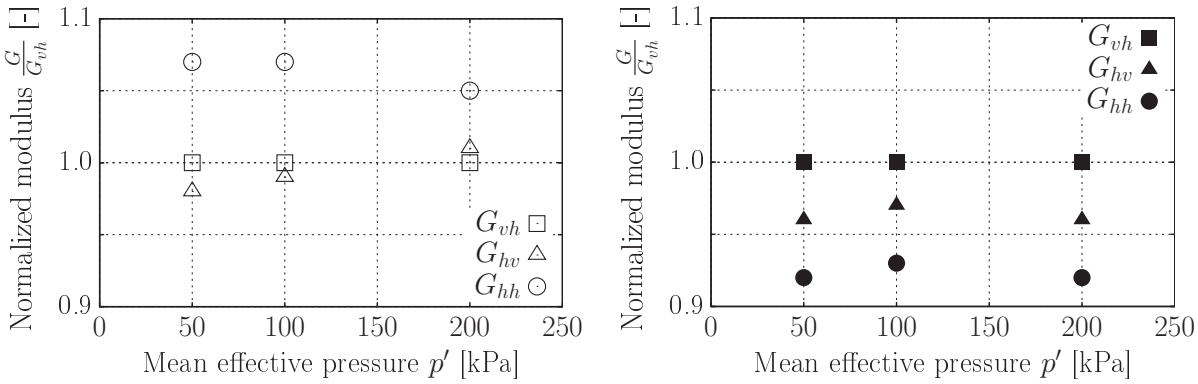

Figure 4.5: Normalized shear moduli, G/G_{vh}, versus mean effective stress, p': (a) for the specimen prepared by the AP method at the void ratio of 0.75 ($D_r = 76\%$), (b) for the specimen prepared by the MT method at the void ratio of 0.77 ($D_r = 72\%$).

4.1.2 Effect of sample preparation method at the large-strain level

Figure 4.6 presents results from the subsequent drained shearing phase. The curves of deviatoric stress, q, versus axial strain, ε_1, and volumetric strain, ε_v, versus axial strain, ε_1, are provided for specimens prepared by either air pluviation (Figure 4.6a) or moist tamping (Figure 4.6b). For both sample preparation methods data for loose and dense specimens are provided. The general response is similar for both preparation methods. The q-ε_1 curves of the dense specimens show a high initial stiffness, reach a peak corresponding to the maximum shear strength followed by softening towards the critical state. The loose specimens show a more gradual increase of q with ε_1, reach the maximum deviatoric stresses at much higher axial strains and show no or only slight softening afterwards. The volumetric response curves reveal a short initial contractive phase followed by pronounced dilatancy for the dense specimens. The loose specimens mainly show contraction and only a slight dilatant phase towards the end of the test.

In Figure 4.7 the results for the dense and the loose specimens prepared by either AP or MT are compared in separate $q-\varepsilon_1$ and $\varepsilon_v-\varepsilon_1$ diagrams. Figure 4.7a compares the data for the dense specimens ($D_r = 74\%$), showing that the $q-\varepsilon_1$ curve for the MT specimen is located above the curve for the AP specimen up to the axial strain of 5%. This means that the initial stiffness of the specimen prepared by the MT method is higher than the one of the specimen prepared by the AP method. Furthermore, this figure shows that the peak of the deviatoric stress, q_{peak}, for the specimen prepared by the MT method is located at the axial strain of 3%, where for the specimen prepared by the AP method it is found at the axial strain of 7.5%. Furthermore, q_{peak} is slightly lower for the MT specimen. Regarding the volumetric response, the contractive phase is shorter and the dilatancy is more pronounced for the MT specimen. However, both types of specimens seem to reach a similar volumetric strain at large strains.

The results for loose specimens (D_r= 18%) in Figure 4.7b show no significant differences between the AP and the MT specimens with respect to the initial stiffness. However, at axial strains above about 2 % the $q-\varepsilon_1$ curve for the AP specimen is again located above those for the specimens prepared by the MT method (with $w = 5$ or 15%). As it is apparent from this figure, the peaks of the three curves are all located at the same strain level. The water content during sample preparation appears to have minimal impact on the $q-\varepsilon_1$ curves for loose specimens prepared by MT. However, it is noteworthy that the initial slope of the $q-\varepsilon_1$ curve for the specimen prepared with a water content of $w = 5\%$ is marginally steeper than that for the specimens with $w = 15\%$. The initial parts of the curves of volumetric strain are almost identical for both sample preparation methods.

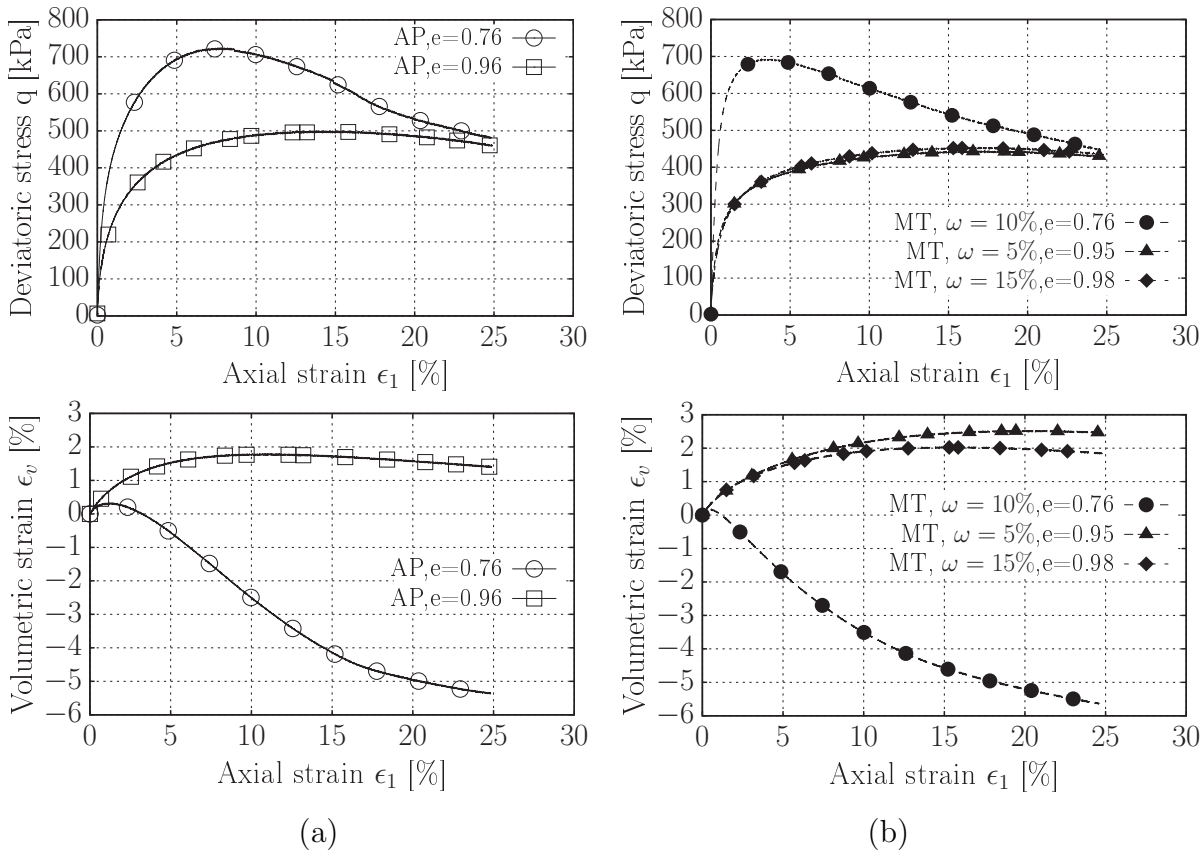

Figure 4.6: Deviatoric stress, q, versus axial strain, ε_1, and volumetric strain, ε_v, versus axial strain, ε_1, for (a) specimens prepared by air pluviation and (b) specimens prepared by moist tamping

However, the AP specimen shows a slight dilatancy at larger strains, which is even smaller or almost absent in the tests on the MT specimens. Therefore, the volumetric strains at the end of the drained shearing phase are slightly different for the loose specimens prepared by either AP or MT.

These observations regarding the $q - \varepsilon_1$ curves can be attributed to the influence of the sample preparation method on soil behavior. Specifically, the applied energy during compaction leads to distinct fabric characteristics in dense specimens prepared via the MT method compared to those prepared using the AP method or in loose specimens.

It can also be found in Figure 4.7 that, despite a larger peak for the denser specimens, the deviatoric stresses q at the end of the tests (at the axial strain, ε_1, of around 24%) are all close to each other regardless of the different initial relative densities. Due to the identical

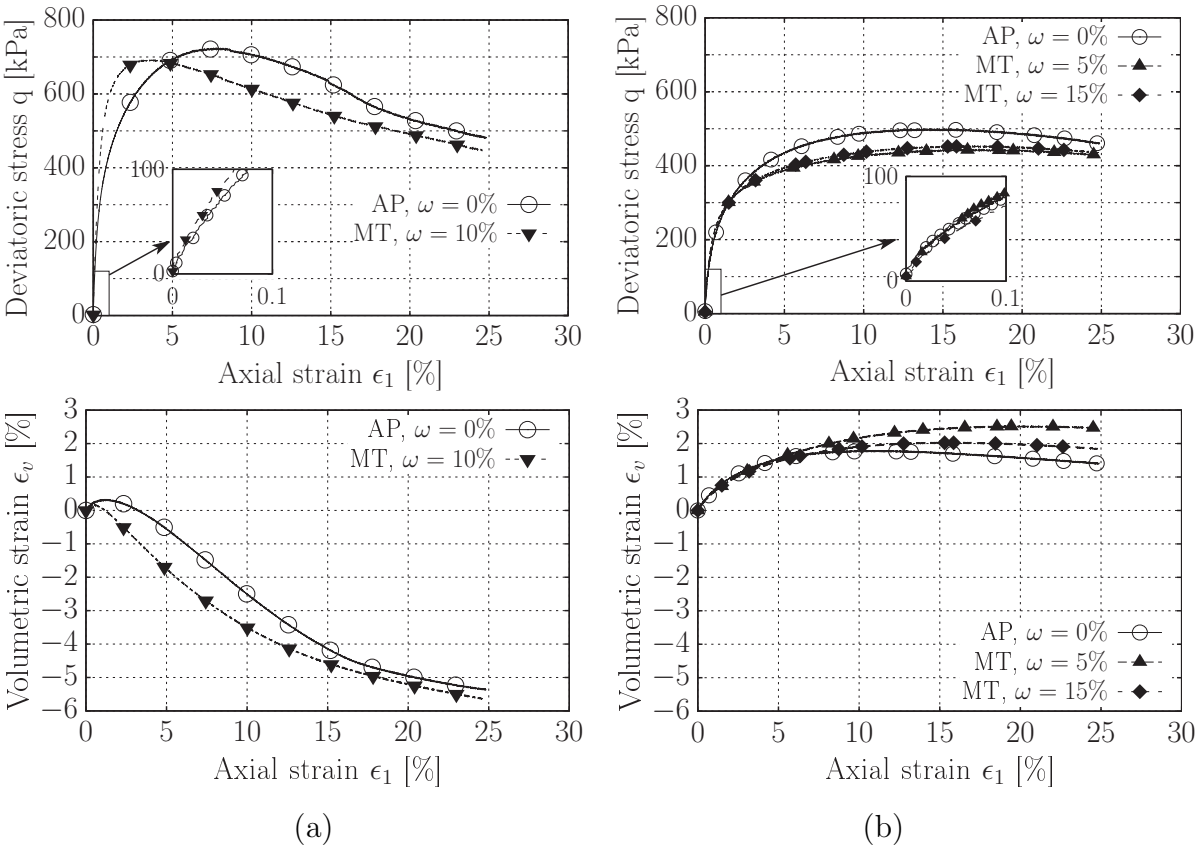

Figure 4.7: Deviatoric stress, q, versus axial strain, ε_1, with a detail up to $\varepsilon_1 = 0.1\%$, and volumetric strain, ε_v, versus axial strain, ε_1, for: (a) specimens prepared at the void ratio of 0.76 (at $D_r = 74\%$), and (b) specimens prepared at the void ratio of 0.96 (at $D_r = 18\%$).

value of the effective confining pressure adopted in the tests, all specimens reached similar deviatoric stresses at the end of the tests.

At large strain level, soil will experience a continuous deformation under constant shear stress and constant mean effective stress. The states of the specimens at this strain level are usually represented by a unique line in a diagram of void ratio versus mean effective stress, e-p', which is called the steady state line or critical state line. Verdugo & Ishihara (1996) stated that the steady state of a soil in a triaxial test is usually reached at axial strains larger than 20-25%, irrespective of the initial state of the samples. The steady / critical state line is described in form of Equation 4.1 or 4.2 in previous works (Li & Wang, 1998).

$$e_{ss} = \lambda - \Lambda \left(\frac{p'_{ss}}{p_a} \right)^{\Gamma} \tag{4.1}$$

$$e_{ss} = L - \delta \ \log \left(\frac{p'_{ss}}{p_a} \right) \tag{4.2}$$

where, e_{ss} is the void ratio at the steady / critical state, p'_{ss} is the mean effective stress at the steady / critical state and p_a is atmospheric pressure. λ, Λ, Γ, L and δ are material constants. A state parameter, Ψ, is defined as a difference between the current void ratio e and e_{ss} for the same mean effective stress, $\Psi = e - e_{ss}$ (Been & Jefferies, 1985).

In Figure 4.8a, the void ratios of the specimens prepared by the AP and MT methods measured at the last isotropic stress level ($p' = 100$ or 200 kPa), denoted as the open points, are compared with those measured at the axial strain of 24%, denoted as the solid points. The latter are plotted over the mean effective stress at the steady state. It can be seen that the void ratios measured at the axial strain of 24% were relatively close to each other regardless of the initial value and the sample preparation method. The differences between the void ratios obtained at the axial strain of 24% could be due to limitations of the triaxial test procedure (Roscoe et al., 1958), e.g. shear band formation in the specimens. Based on the aforementioned results, all specimens could have a similar fabric at the axial strain of 24%, which seems to agree to the observation reported by Guo & Yang (2017).

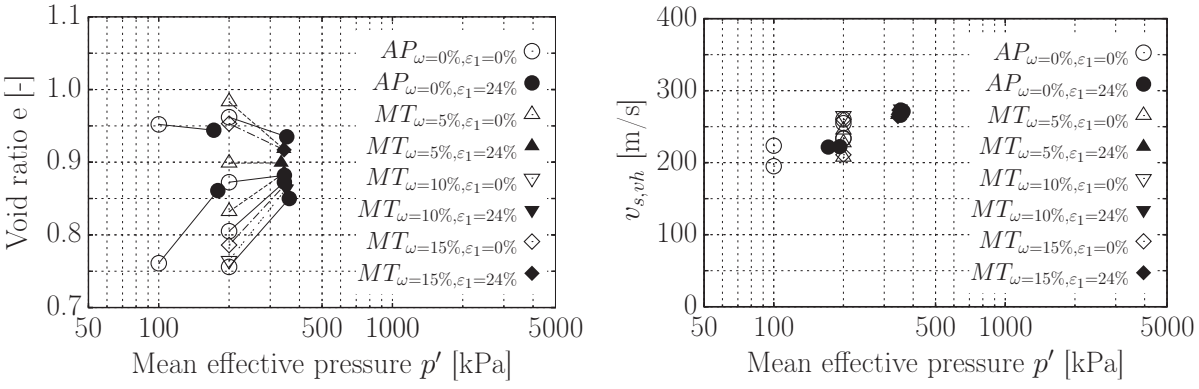

(a) (b)

Figure 4.8: A comparison of the values at the beginning and end of the tests for: (a) void ratio, e; (b) shear wave velocity in the vertical direction of the specimens, $v_{s,vh}$. The open dots denote the values obtained at the beginning of the drained triaxial tests. The solid dots denote the values measured at the end of the drained triaxial tests.

To verify the hypothesis of Guo & Yang (2017), stating that shear wave velocity in the critical state is independent of initial fabric, the vertical shear wave velocity, $v_{s,vh}$, was measured at the axial strain of 24% during the compressional triaxial tests. These tests were performed with a low displacement rate of 0.1 mm per minute. During this process, the variation of the height of the specimens was measured using a calibrated LVDT and recorded in a computer with respect to time. Before performing the bender element test, the time of the triaxial test was recorded to obtain the height of the specimen. After that, the bender element test was immediately performed, and the input and output signals were saved in the computer. However, due to the quality of the signals from the bender element measurements, it was not always easy to get clear signals with one try. Therefore, these measurements of shear wave velocity at large strain were successful only for some of the tests. The respective data are presented in Figure 4.8b.

Figure 4.8b shows the vertical shear wave velocity, $v_{s,vh}$, with respect to the mean effective stress, p'. This figure compares the measured $v_{s,vh}$ for all of the specimens prepared by the AP and MT methods with different relative densities. In this figure, the open points show the measured wave velocity after the isotropic consolidation and the solid points show the measured wave velocity at the axial strain of 24%. The significant scatter of the wave velocities at the initial state is due to the significant impact of density and slight impact of the sample preparation method on the wave velocity. However, as can be seen in Figure 4.8b, the wave velocity obtained at the axial strain of 24% is almost independent of the sample preparation method and the density of the specimens. This means that the wave velocity at this strain is only dependent on p'. This is in good agreement with the steady state / critical state theory since all combinations of void ratio and mean effective stress should lie on a unique curve, the steady state / critical state line addressed above.

4.2 Effect of stress state

In this test series triaxial compression tests were performed under undrained conditions. The undrained conditions were chosen in order to study the effect of an anisotropic stress state while keeping the volume of the specimens constant. The specimens of Hostun sand were prepared by air pluviation with different void ratios, e, ranging from 0.72 to 0.93 ($D_r = 32\%-87\%$). All specimens were fully water-saturated and consolidated isotropically to $p' = 50$, 100, 200 or 300 kPa. The undrained shearing with strain control was conducted with the displacement rate of 0.1 mm/min until the axial strain, ε_1, reached around 24%. The shear wave velocities were measured at different isotropic stresses ($p' = 50$, 100, 200

or 300 kPa) during the isotropic consolidation phase, as well as during the undrained shearing. Further details on the experimental procedure and the testing program can be found in Section 3.5.2. The results of these tests will be presented in the following subsections.

4.2.1 Isotropic stress state

Figure 4.9 shows the data of the maximum shear modulus, $G_{\max}$, and the corresponding shear wave velocity in the vertical direction, $v_{s,vh}$, measured during the isotropic loading phase. The $G_{\max}$ and the $v_{s,vh}$ data are presented as functions of void ratio e for the four tested stress levels $p' = 50$, 100, 200 and 300 kPa. Beside the data from the current test series, also data at $p' = 50$, 100 and 200 kPa from the drained triaxial tests described in Section 4.1 are included. It is evident in Figure 4.9 that the $G_{\max}$ and the $v_{s,vh}$ values for each stress level are lying in a narrow band, and both quantities increase with increasing stress and decreasing void ratio.

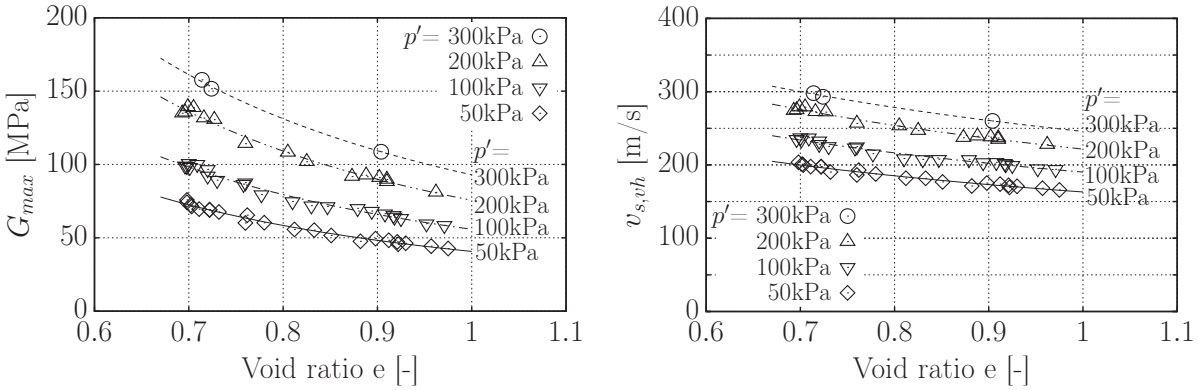

Figure 4.9: Variation of (a) maximum shear modulus, $G_{\max}$, and (b) shear wave velocity in the vertical direction, $v_{s,vh}$, against void ratio, e, for the different isotropic stress states, $p' = 50$, 100, 200, 300 kPa.

In order to study the effect of isotropic stress states on the fabric anisotropy of granular soils, the shear wave velocities were measured in various directions in a specimen ($v_{s,vh}$, $v_{s,hv}$ and $v_{s,\theta}$) at the isotropic stress states of $p' = 50$, 100 and 200 kPa. Six pieces of bender elements were used which were either integrated in the end plates or mounted on the sides of the specimen. The elements are marked with numbers from 1 to 6, as can be seen in Figure 4.10a. This figure is a schematic sketch for the arrangement of the bender elements

Table 4.1: Relationship between the couple of bender elements used to generate the wave and the angle of the measurements presented in Figure 4.10b: for the wave, the first number indicates the element used for the sending signal, and the second number indicates the element used for the receiving signal.

Shear wave	4 to 3	4 to 5	1 to 2	3 to 6	5 to 6	5 to 4	2 to 1	6 to 3
θ [°]	0	45	90	135	180	225	270	315

on a specimen, and shows the directions of the wave velocities measured. As can be seen in this figure, all of the wave velocities in various directions are corresponding to waves having the propagation and polarization directions in the same vertical cross section. The $v_{s,vh}$ was measured between the elements 1 and 2. The $v_{s,hv}$ was measured between the elements 3 and 4, and between the elements 5 and 6. The $v_{s,\theta}$, with the angle $\theta = 45°$, 135°, 225° or 315° measured counterclockwise from the horizontal to the propagation direction of the waves, was obtained between the elements 3 and 6, and between the elements 4 and 5, respectively. Thus, the couple of elements used to generate a certain wave can be indicated by the wave propagation direction θ, and their relationship is summarized in Table 4.1.

The wave velocities obtained from a specimen prepared at the void ratio of $e = 0.90$ for the various stress levels are presented in polar coordinates with respect to the direction θ in Figure 4.10b. An alternative presentation is provided in Figure 4.10c where v_s is plotted versus θ. The results in both presentations show that the velocities in the various directions within the vertical cross section of the specimen are almost the same for a certain isotropic stress level, and increase evenly with the increasing stress level. It can be concluded that the isotropic loading has no significant effect on the fabric, which remains rather isotropic during the increase of the isotropic stress.

4.2.2 Anisotropic stress state

After completing the final isotropic consolidation stage, the current volume of the specimens was determined by subtracting the volume change recorded during consolidation from the initial volume, which was measured after sample preparation. Following this, the monotonic triaxial test commenced with a shear rate of 0.1 mm per minute. The volume of the specimens remained constant throughout testing under undrained conditions.

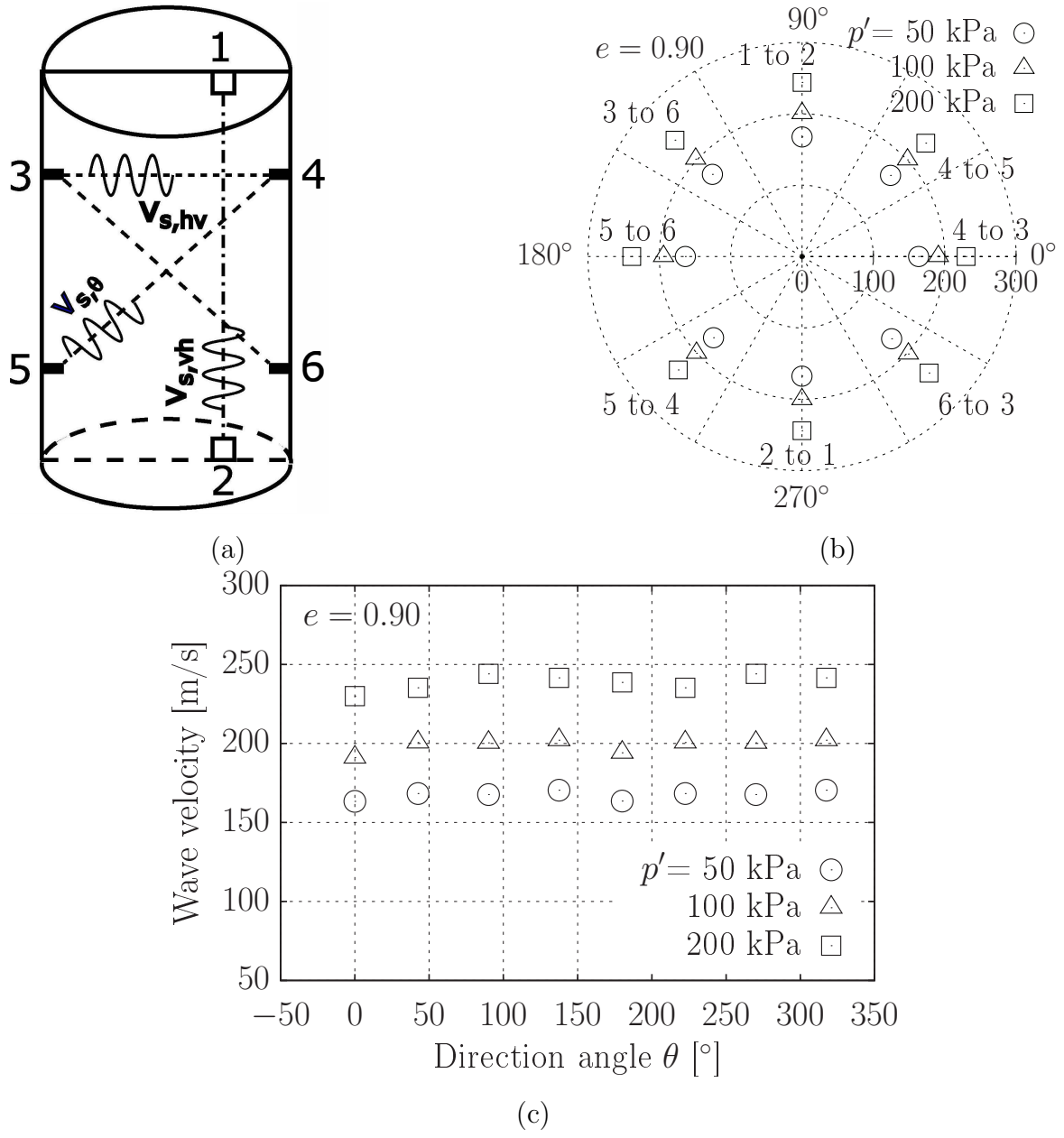

Figure 4.10: (a) Schematic sketch for the arrangement of bender elements; (b) v_s measured in different directions at the isotropic stress states of $p' = 50$, 100, 200 kPa shown in a polar presentation; (c) same data in a diagram of v_s versus direction angle θ.

Figure 4.11 compares the results from the undrained shearing phase obtained for specimens prepared with the void ratios of $e = 0.78$, 0.85, and 0.93, and consolidated under an identical mean effective stress of $p' = 100$ kPa. As depicted in Figure 4.11a, the deviatoric stress, q, exhibited a rapid increase in all specimens until the axial strain, ε_1, reached approximately 1%. Beyond this point, their behaviors diverged significantly. The loose

specimen ($e = 0.93$ and $D_r = 32\%$) displayed only slight variations in q with increasing ε_1. Conversely, the medium dense specimen ($e = 0.85$ and $D_r = 53\%$) experienced a slight decrease in q before undergoing a rapid increase once more. In contrast, the dense specimen ($e = 0.78$ and $D_r = 71\%$) exhibited a continuous increase in q at varying rates until ε_1 reached 17%. Notably, the dense specimen demonstrated a significantly larger peak in q compared to the medium dense and loose specimens. Under undrained conditions, the volume change associated to the change in stresses was prevented due to the constant pore water volume, and was transformed into the change in pore water pressure, u. Figure 4.11b illustrates the variation of u in the three tests as ε_1 increases. It is observed that u was initially set at 200 kPa for all tests and increased rapidly until ε_1 reached approximately 1%. Subsequently, as ε_1 continued to increase, the loose specimen exhibited a gradual decrease in u to around 230 kPa after a slight initial increase, whereas u in the medium dense specimen was nearly completely dissipated. In contrast, the dense specimen experienced an even faster decrease in u compared to the two aforementioned specimens, eventually entering the negative pressure zone by the end of the test. These findings indicate that, after a short contractive phase, the loose specimen exhibits minimal dilatancy, while the dense specimen demonstrates significant dilatancy. Finally, the effective stress paths of these tests are provided in a q-p' diagram in Figure 4.11c. In agreement with the evolution of pore water pressure, the specimens with lower density reach lower mean effective stresses p' during the tests. However, the failure lines followed during the final phase of the tests are only moderately affected by density.

In addition to the previously mentioned conclusion, there is another notable difference evident in the results depicted in Figure 4.11, particularly concerning the behavior of the loose specimen compared to the others. While measurements from the loose specimen exhibit a smooth and continuous variation, those from the medium dense and dense specimens display a distinct breakpoint occurring at $\varepsilon_1 = 19\%$ and 8%, respectively. This breakpoint is also evident in Figure 4.11b, occurring at a pore water pressure of about $u = 20$ kPa. This observation raises concerns regarding the reliability of the calculated stresses after the breakpoint, i.e. at very low or even negative pore water pressures, a topic that will be further discussed in the subsequent chapter, drawing upon thorough data analysis.

Figure 4.12 presents similar data for the higher initial mean effective stress $p'_0 = 300$ kPa. The influence of density on the measured curves is qualitatively identical to the one previously described for $p'_0 = 100$ kPa.

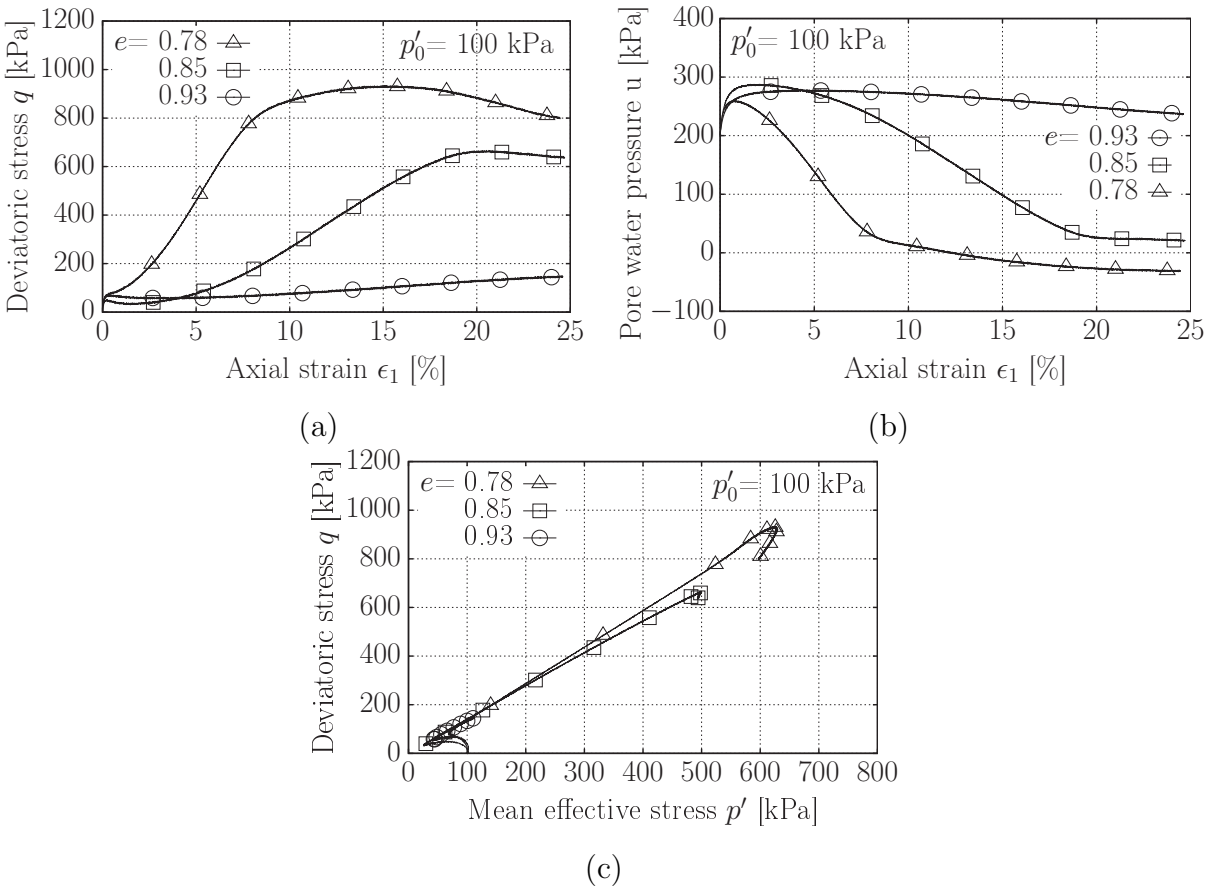

Figure 4.11: Results from the undrained triaxial tests conducted on the specimens prepared with different void ratios, $e = 0.78 - 0.93$, and consolidated isotropically at the identical initial mean effective stress of $p'_0 = 100$ kPa: (a) Deviatoric stress, q, versus axial strain, ε_1, (b) Pore water pressure, u, versus axial strain, ε_1, (c) Effective stress paths.

Figure 4.13 illustrates the influence of initial effective stress on the measured response during undrained shearing. These tests were conducted on specimens prepared with an identical void ratio of $e = 0.93$ ($D_r = 32\%$), subjected to the initial effective stresses, p'_0, of 100, 200, and 300 kPa. As depicted in Figure 4.13a, all three tests exhibit similar trends. The first peak in the curve of deviatoric stress versus axial strain and the subsequent quasi-steady state occur at similar axial strains of about 0.5% and 3%, respectively, although their magnitudes increase with rising p'_0. This phenomenon is also reflected in the variation of pore water pressure in these specimens, as shown in Figure 4.13b. The effective stress paths provided in Figure 4.13c show a similar pattern in the initial phase and follow the same failure line in the final phase of the tests.

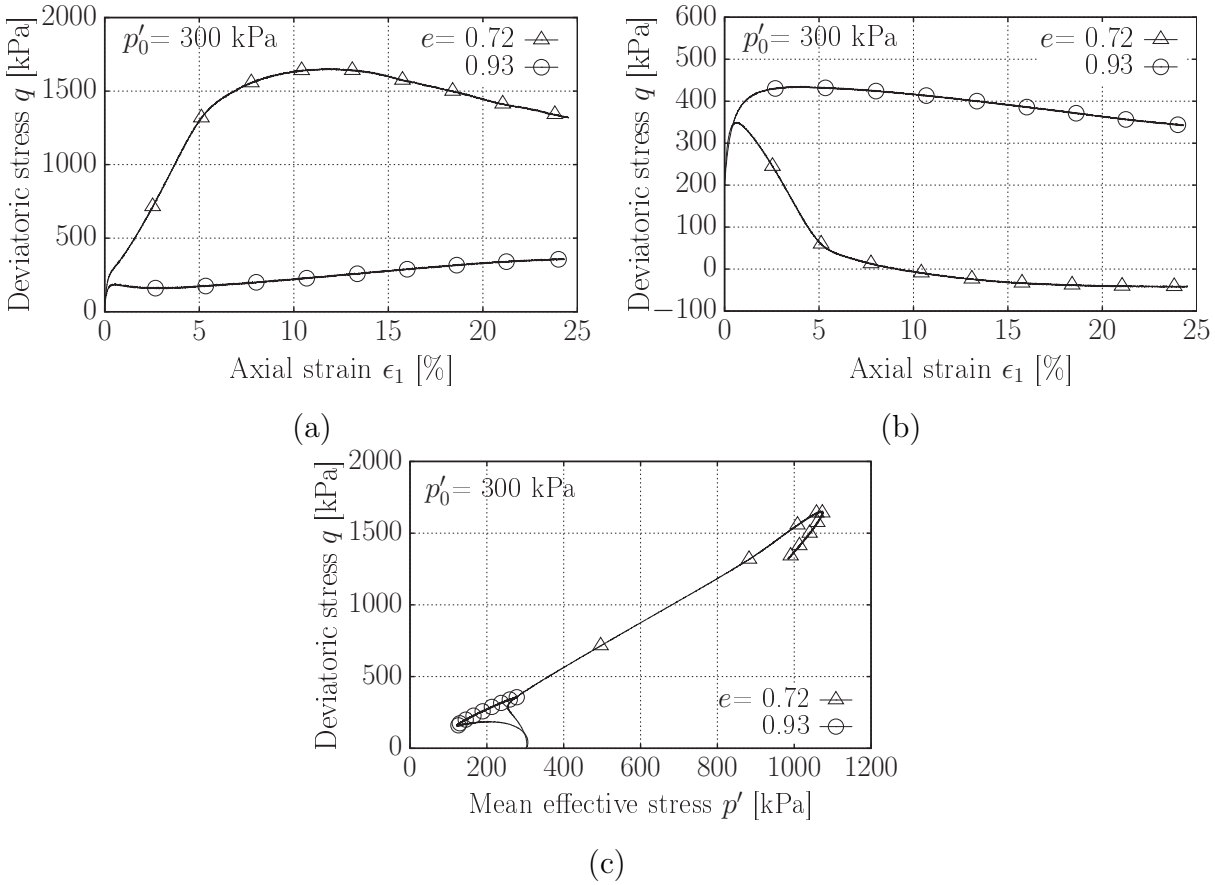

Figure 4.12: Results from the undrained triaxial tests conducted on the specimens prepared with different void ratios, $e = 0.93$ and 0.72, and consolidated isotropically at the identical initial mean effective stress of $p'_0 = 300$ kPa: (a) Deviatoric stress, q, versus axial strain, ε_1, (b) Pore water pressure, u, versus axial strain, ε_1, (c) Effective stress paths.

To complete the discussion of the large-strain behaviour, the peak and residual friction angles derived from the triaxial tests with shearing under drained or undrained conditions are presented as functions of initial relative density D_{r0} in Figure 4.14. The peak friction angles φ_p have been derived from the maximum stress ratios $\eta = q/p$ measured during the test, while the critical values φ_{cs} have been determined from the data at the largest strain applied in the respective test. As expected and independently of the drainage conditions, the peak values are larger than the residual ones. While the peak friction angles considerably grow with increasing relative density, only a slight increase with D_{r0} is evident in the residual friction angles. This may be partly due to the fact that a critical state was not fully reached in all tests. Furthermore, the φ_p values from the drained tests (taken from the tests on AP samples described in Section 4.1) are slightly larger than

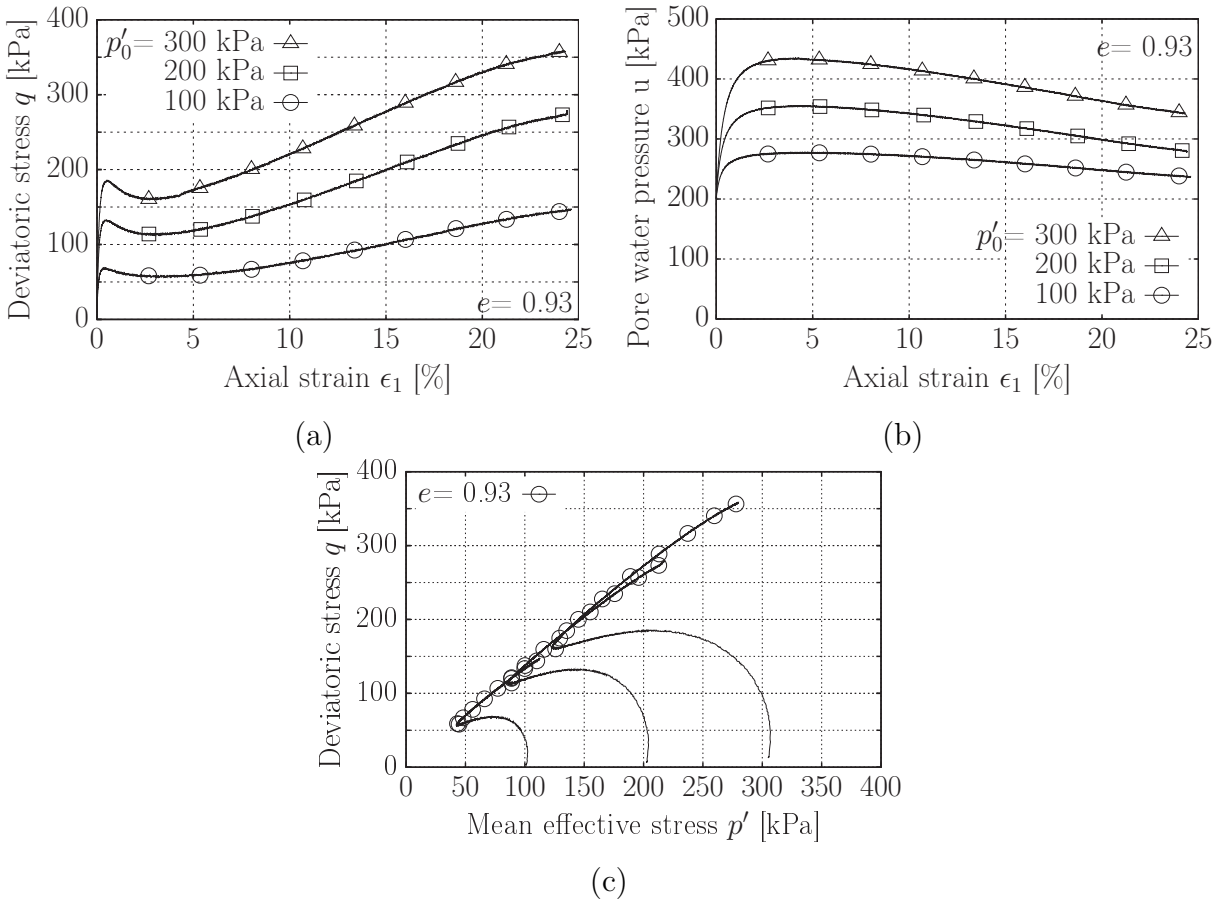

Figure 4.13: Results from undrained triaxial tests conducted on specimens prepared with identical void ratio, $e = 0.93$, and consolidated isotropically at various initial mean effective stresses of 100, 200, and 300 kPa: (a) Deviatoric stress, q, versus axial strain, ε_1, (b) Pore water pressure, u, versus axial strain, ε_1, (c) Effective stress paths.

those from the undrained ones. A similar dependence of φ_p on the drainage conditions was also reported by Andersen (2009) and Wichtmann (2016). In contrast, the φ_{cs} data does not show a clear effect of the drainage conditions during shearing.

Throughout the undrained shearing, the shear wave velocity in the vertical direction was periodically measured until ε_1 reached approximately 24%. Figure 4.15a displays the wave velocities $v_{s,vh}$ obtained from a specimen prepared at $e = 0.93$ ($D_r = 32\%$) and consolidated at an initial effective stress of $p'_0 = 300$ kPa, plotted against the mean effective stress, p'. The measurement points, depicted in Figure 4.15b, are situated along the effective stress path of the tests. Before the phase transformation, wave velocities are represented by open circles labeled numerically from 1 to 5. After the phase transformation, filled circles, labeled numerically from 7 to 12, denote the wave velocities. The

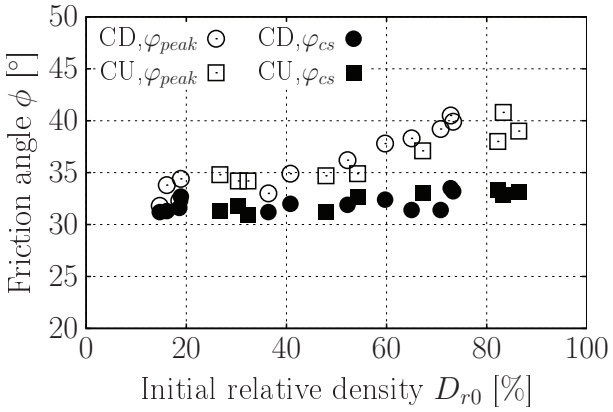

Figure 4.14: Peak friction angles φ_p and critical friction angles φ_{cs} from the drained and the undrained triaxial tests as functions of initial relative density

measurement taken at the phase transformation is marked as number 6. For strain controlled triaxial tests, the lateral bender elements were not installed on the side surface of the specimens because the large deformation in the horizontal direction could damage the sealing condition between the bender elements and the specimen.

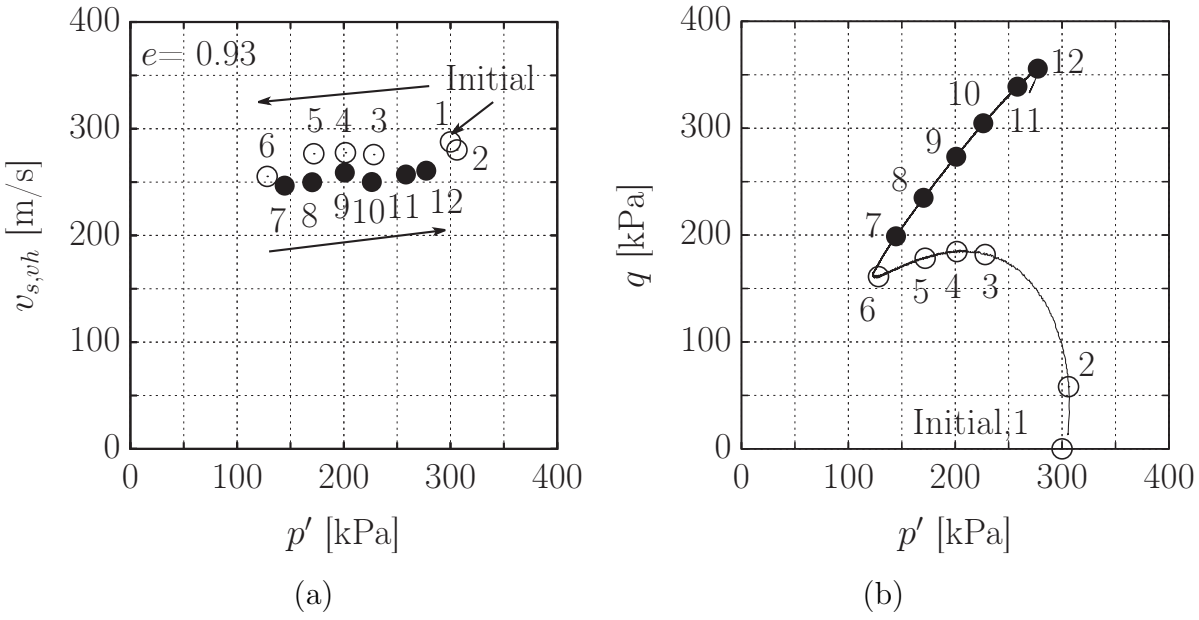

Figure 4.15: Shear wave velocity $v_{s,vh}$ along the stress path of the CU triaxial test. The measurements obtained before the phase transformation are denoted as open dots, while those obtained after the phase transformation are denoted as filled dots.

Figure 4.15a illustrates that the shear wave velocity is primarily influenced by p'. Before the phase transformation, wave velocity decreases with decreasing p', while it increases with increasing p' afterwards. However, it is notable that the open symbols consistently lie above the filled symbols. For instance, open circle 4 indicates a higher velocity than filled circle 9, despite both are measured under the same p'. This observation suggests a potential influence of the stress ratio, q/p', on the elastic stiffness of granular materials, as depicted in Figure 4.15b, where the q/p' of the empty symbols is lower than that of the filled symbols. Figure 4.15a thus gives hints that the shear wave velocity for a given p' decreases with an increasing stress ratio q/p'.

Figure 4.16 presents the results of the additional tests performed with stress-controlled loading under either drained (test SP-14 in Table 3.5) or undrained conditions (test CU-09 in Table 3.6). Figure 4.16 compares the in-plane shear wave velocities, encompassing $v_{s,vh}$, $v_{s,hv}$, and $v_{s,\theta}$ ($\theta = 45°$, 135°, 225°, and 315°). The data are provided in both a polar presentation and diagrams of v_s versus θ. The polar coordinates indicate the direction of the wave propagation generated by the respective elements, following the definition outlined in Table 4.1. The specimens tested were prepared with a void ratio of $e = 0.93$ ($D_r = 32\%$) and consolidated at an isotropic stress state of $p'_0 = 200$ kPa. Upon completion of the consolidation stage, wave velocities in various directions were measured using three pairs of bender elements at the specimens (Figure 4.10a), represented as the open squares in Figure 4.16 corresponding to $\sigma'_1/\sigma'_3 = 1$. Subsequently, the specimens were subjected to vertical loading under both drained and undrained conditions until the ratio of vertical to horizontal effective stress, σ'_1/σ'_3, reached 3. Upon stabilization, wave velocities in the corresponding directions were measured again, shown as filled squares in Figure 4.16.

In Figure 4.16, it is evident that the in-plane wave velocities in different directions, $v_{s,vh}$, $v_{s,hv}$, and $v_{s,\theta}$, are very similar, with $v_{s,vh} \approx v_{s,hv} \approx v_{s,\theta}$, for specimens under isotropic stress conditions. However, the effects of stress anisotropy on wave velocities differ under varying drainage conditions.

Under drained conditions, p' equaled 333 kPa due to the constant σ'_3 of 200 kPa when $\sigma'_1/\sigma'_3 = 3$. As the current p' exceeds p'_0, the filled squares are positioned at higher values of shear wave velocity than the open squares in Figure 4.16a. Additionally, the vertical shear wave velocity $v_{s,vh}$ is notably greater than the horizontal $v_{s,hv}$ due to particle rearrangement, leading to a concentration of contact normal forces in the major principal stress direction. $v_{s,\theta}$ in inclined directions has a value between $v_{s,vh}$ and $v_{s,hv}$.

In Figure 4.16b, under undrained conditions, filled squares are positioned closely to the open squares in the corresponding directions because the current p' equals p'_0. Notably,

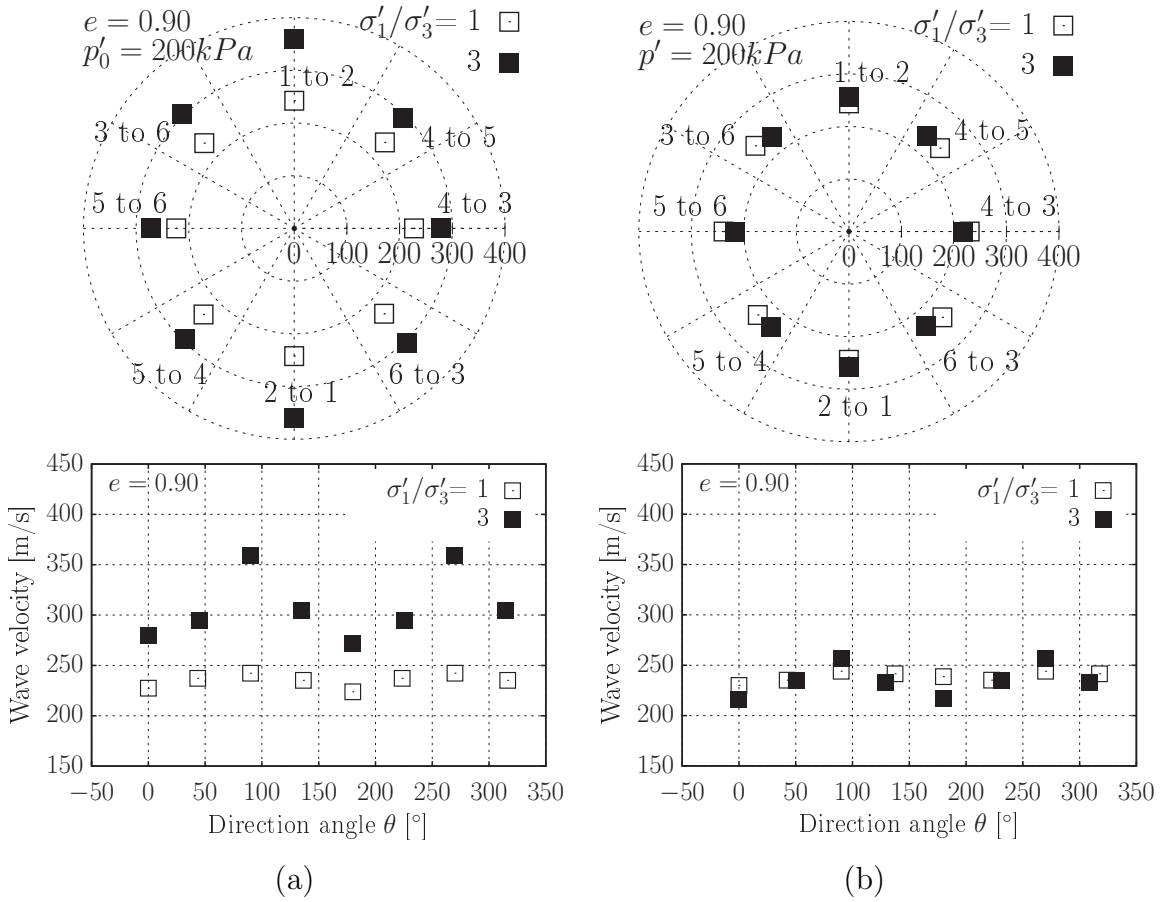

(a) (b)

Figure 4.16: Shear wave velocity v_s in different directions measured at the isotropic and anisotropic stress states with the identical stress ratio under: (a) drained conditions, (b) undrained conditions. The measurements obtained at the isotropic stress state ($\sigma'_1/\sigma'_3 = 1$) are denoted as open squares, while those obtained for the stress ratio $\sigma'_1/\sigma'_3 = 3$ are shown as filled squares.

under anisotropic stress, the shear wave velocity in the vertical direction is slightly larger than under isotropic stress, whereas the horizontal shear wave velocity under anisotropic stress is slightly less than that under isotropic stress. This observation suggests a decrease in in-plane wave velocity as the propagation direction shifts from the major principal stress direction to the minor principal stress direction. These findings underscore the influence of stress anisotropy on fabric, a phenomenon inadequately captured solely by p' or the stress ratio, q/p'.

4.3 Effect of particle shape and gradation

In this section the results of the experiments on the effect of particle shape and gradation on the small-strain stiffness will be presented. The experiments were performed on three materials with different particle shape: crushed glass (with roundness $R = 0.3$, sphericity $S = 0.6$, regularity $\rho = 0.45$), Rhine sand ($R = 0.44$, $S = 0.76$, $\rho = 0.60$), and round glass ($R = 0.90$, $S = 0.90$, $\rho = 0.90$). All three materials were tested with two distinct gradations, having the same mean grain size but different uniformity coefficients of $C_u = 1.25$ and 5.0.

For each material, samples with different relative densities were prepared by the air pluviation (AP) method. All specimens underwent full saturation and were successively consolidated at isotropic stress levels of $p' = 50$, 100, and 200 kPa. Following the final isotropic consolidation, the deviatoric stress was stepwise increased to $q = 100$, 200, and 300 kPa, while maintaining the lateral effective stress at $\sigma'_2 = \sigma'_3 = 200$ kPa. At the conclusion of each isotropic or anisotropic consolidation stage, shear wave velocities ($v_{s,vh}$, $v_{s,hv}$, $v_{s,hh}$) were measured in both vertical and horizontal directions to determine the elastic properties of the specimens. Also measurements of the P wave velocity in the vertical direction ($v_{p,v}$) were performed in this test series. Further details regarding the experimental program (Section 3.5.3) and material characteristics can be found in Chapter 3.

The experiments of this test series aim on examining the impact of particle shape and gradation, coupled with stress state (isotropic, anisotropic) and density, on the P and S wave velocities and the corresponding elastic stiffness of granular materials, including the shear moduli G_{vh}, G_{hv}, G_{hh}, Young's modulus E_v, and Poisson's ratio ν_{vh}.

4.3.1 Shape of particles

4.3.1.1 Influence on small-strain shear modulus $G_{\max}$

The influence of void ratio on the small strain stiffness, $G_{\max}$, measured along different propagation directions and with different polarizations of the shear waves, G_{vh}, G_{hv}, and G_{hh}, is shown for the well-graded materials ($C_u = 5.0$) in Figure 4.17. The diagrams in Figure 4.17a, b and c show the results for isotropic stress states, while the diagrams in Figure 4.17d, e and f present the results for anisotropic stress states. It can be seen that for all materials, the $G_{\max}$ in the various directions increases with a decrease in void ratio for both isotropic and anisotropic stress states. However, it appears that the void ratio

has a greater impact on $G_{\max}$ in the various directions under anisotropic stress states compared to isotropic stress states.

Figure 4.17a, b and c show the G_{vh}, G_{hv}, and G_{hh} obtained at the isotropic stress states of $p' = 50$ and 200 kPa for the three materials. For each stress level, the G_{vh}, G_{hv}, and G_{hh} values are similar to each other at an identical void ratio, and increase with the decrease in void ratio. However, the variation of void ratio has a higher impact on the $G_{\max}$ for the angular crushed glass and the subangular Rhine sand under isotropic stresses than for the round glass beads.

Figure 4.17d, e and f show the G_{vh}, G_{hv}, and G_{hh} obtained at the anisotropic stress state of $q = 300$ kPa in combination with the constant lateral effective stress, $\sigma'_2 = \sigma'_3 = 200$ kPa, for the three materials. In contrast to the isotropic stress state, significant differences between G_{vh}, G_{hv}, and G_{hh} are evident for the anisotropic stress state. For all three materials G_{vh} is significantly larger than G_{hh}. G_{hv} lies in between (Rhine sand and crushed glass) or quite close to G_{vh} (round glass). As expected, a decrease in void ratio results in an increase in G_{vh}, G_{hv}, and G_{hh}. However, the rates of increase of the G_{vh}, G_{hv} and G_{hh} differ from each other. For all of the tested materials, G_{vh} grows at the highest rate while G_{hh} grows at the lowest rate. The rate of G_{hv} is in between them. Therefore, the difference between the $G_{\max}$ values in various directions also increases with a decrease in void ratio. Furthermore, there is an influence of grain shape on the rates of the shear moduli with void ratio. The G_{vh} and G_{hv} for the round glass beads show larger rates of increase than those for the angular crushed glass. The G_{vh} and G_{hv} for the subangular particles of Rhine sand exhibit an intermediate rate of increase.

Figure 4.17 also illustrates the influence of stress state on the maximum stiffness of the materials studied (RG, RS, CG) under isotropic and anisotropic loading conditions. Across all materials, stiffness increases with rising isotropic pressure, p', as depicted in Figure 4.17a, b, and c. Additionally, the results reveal that under anisotropic stress conditions (e.g., $q = 300$ kPa, $p' = 300$ kPa), the maximum stiffness of the soil is larger than for the specimens under isotropic loading, as shown in Figures 4.17d, e, and f or Figure 4.18. This increase is partly due to the rise of p'. Figure 4.18 further elucidates the impact of anisotropic loading on stiffness. Notably, the effect of deviatoric stress, q, on stiffness differs from that of isotropic pressure, p', and in certain samples, dilation or compaction may lead to variations in stiffness with increasing q.

Figure 4.18 illustrates the variation of the maximum stiffness obtained for loose ($D_r = 20\%$) and dense ($D_r = 90\%$) specimens of the three materials studied (RG, RS, CG) along the same stress path. During isotropic loading ($\sigma'_1 = \sigma'_2 = \sigma'_3 \leq 200$ kPa), the

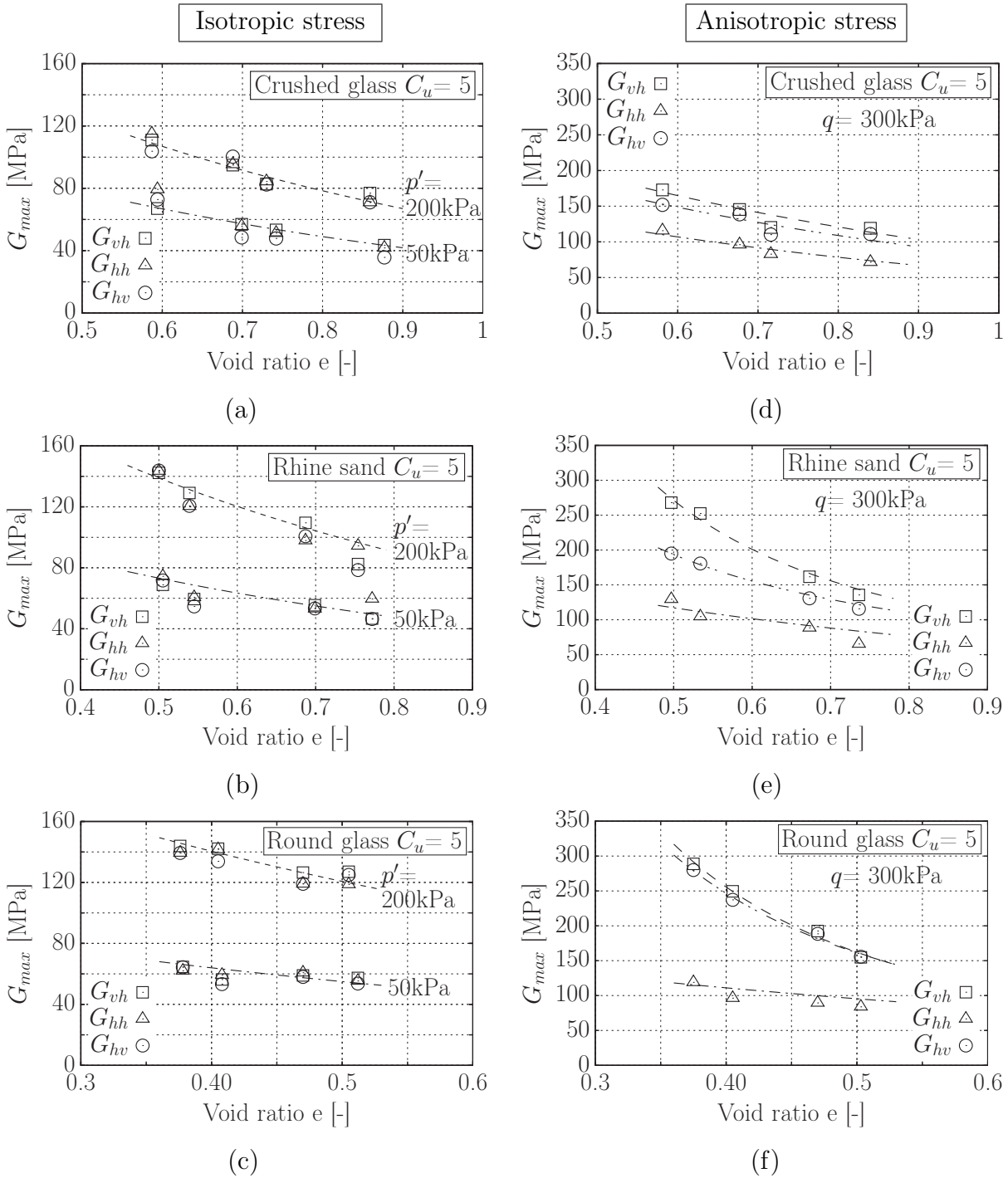

Figure 4.17: Variation of small-strain shear moduli G_{vh}, G_{hv}, and G_{hh} with respect to void ratio e at isotropic stresses of 50 and 200 kPa for: (a) Crushed glass, (b) Rhine sand, (c) Round glass; and under an anisotropic stress with deviatoric stress $q = 300$ kPa and constant $\sigma'_3 = 200$ kPa for: (d) Crushed glass, (e) Rhine sand, (f) Round glass.

$G_{\max}$ in the various directions obtained in the loose and dense specimens for the three materials rises with the increasing effective stress. During the subsequent anisotropic loading ($\sigma'_1 > \sigma'_2 = \sigma'_3 = 200$ kPa), G_{vh} and G_{hv} exhibit further increases with the increasing axial stress, with G_{vh} growing at a larger rate compared to G_{hv}. In contrast, G_{hh} shows even a slight reduction during the anisotropic loading phase. This decrease is most pronounced for round glass beads and appears relatively independent of density. Furthermore, as depicted in Figure 4.18, for loose and more pronounced for dense samples under anisotropic stress conditions, the values of G_{vh} and G_{hv} increase with increasing roundness and sphericity of the particles. On the other hand, it can be seen that the disparity between G_{vh} and G_{hv} during anisotropic loading is also related to the particle shape. For the round glass beads, G_{vh} and G_{hv} show almost the same rate of increase with the increasing axial stress, while for the subangular particles of Rhine sand G_{vh} and G_{hv} clearly exhibit different rates of increase. However, the disparity between G_{vh} and G_{hv} is only moderate for the angular crushed glass.

Figure 4.19 shows the same data as Figure 4.18, but with the mean effective stress p' instead of the effective vertical stress σ'_1 on the horizontal axis. Evidently, all shear moduli show a discontinuity when anisotropic loading starts. This give hints that the shear moduli under anisotropic loading cannot be adequately described by empirical relationships considering void ratio and mean effective stress alone. Instead, they should also consider the stress anisotropy, as is further elaborated in Chapter 5.

The test results may be explained through a micro-mechanical interpretation: At isotropic stress states, the soil fabric is nearly isotropic. However, increasing vertical loading while keeping the horizontal load constant enhances the normal contact forces between grains in the vertical direction, while the horizontal forces remain relatively unchanged. This leads to a higher shear wave velocity $v_{s,vh}$, and consequently increased stiffness G_{vh} in the vertical direction (for further micro-mechanical arguments on the impact of stress anisotropy, see Goudarzy et al. (2018)). Regarding the horizontal directions, the vertically polarized signals, $v_{s,hv}$ and G_{hv}, also benefit from the application of vertical load. However, for horizontally polarized waves, $v_{s,hh}$, additional vertical loading destabilizes contacts in the horizontal direction. The buckling of force chains under higher vertical stress reduces the number of horizontal contacts and weakens the fabric, resulting in lower stiffness in the horizontal direction, especially reflected in the shear wave velocity $v_{s,hh}$ and the corresponding shear modulus G_{hh} (Goudarzy et al., 2020).

If the sand samples on which the wave velocities are measured are considered as a homogeneous continuum, then G_{vh} must be equal to G_{hv} to satisfy the symmetry of the

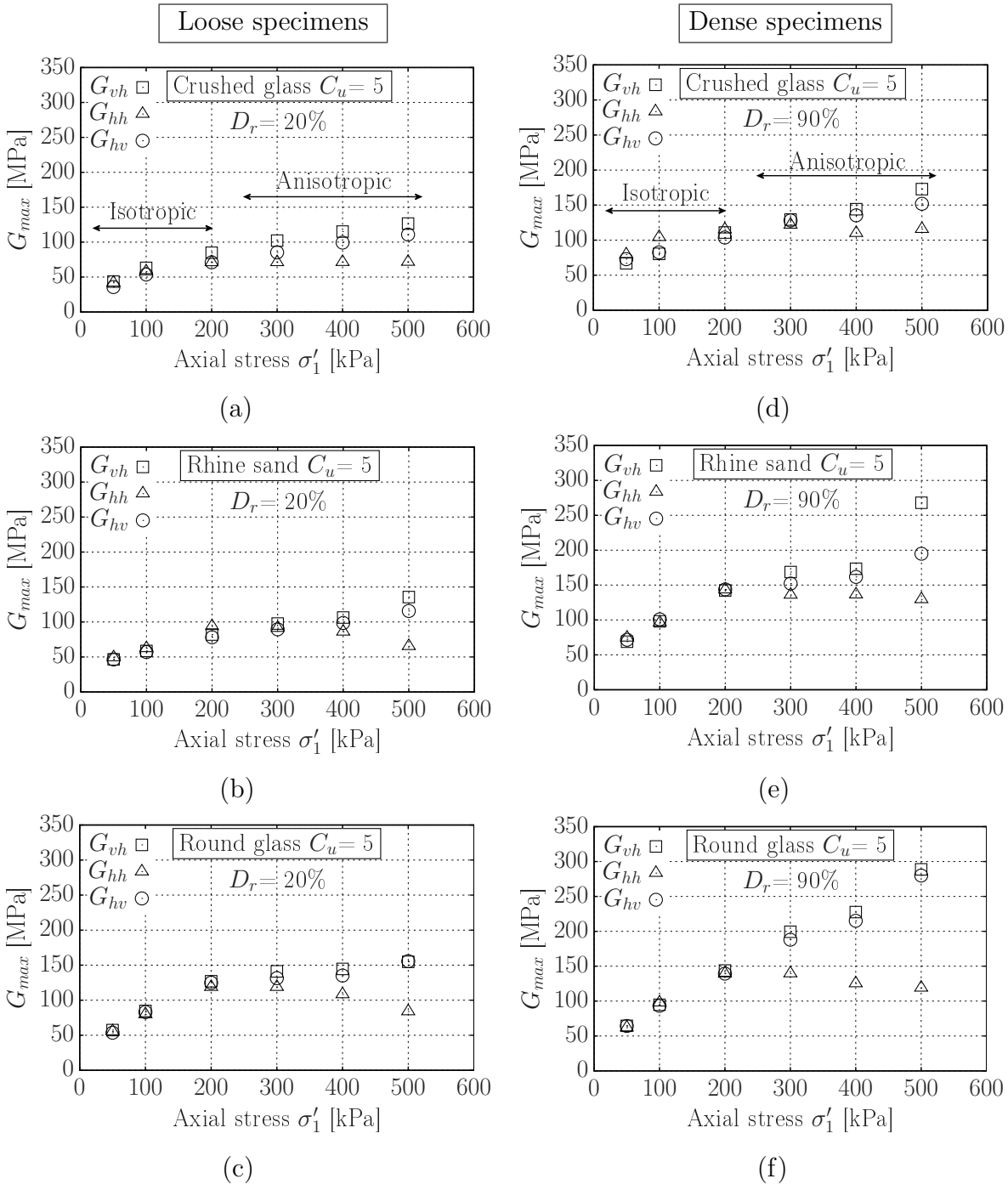

Figure 4.18: Variation of small-strain shear moduli G_{vh}, G_{hv}, and G_{hh} with respect to the effective vertical stress σ'_1 for the loose specimens with the relative density of $D_r = 20\%$: (a) Crushed glass, (b) Rhine sand, (c) Round glass; and for the dense specimens with the relative density of $D_r = 90\%$: (d) Crushed glass, (e) Rhine sand, (f) Round glass.

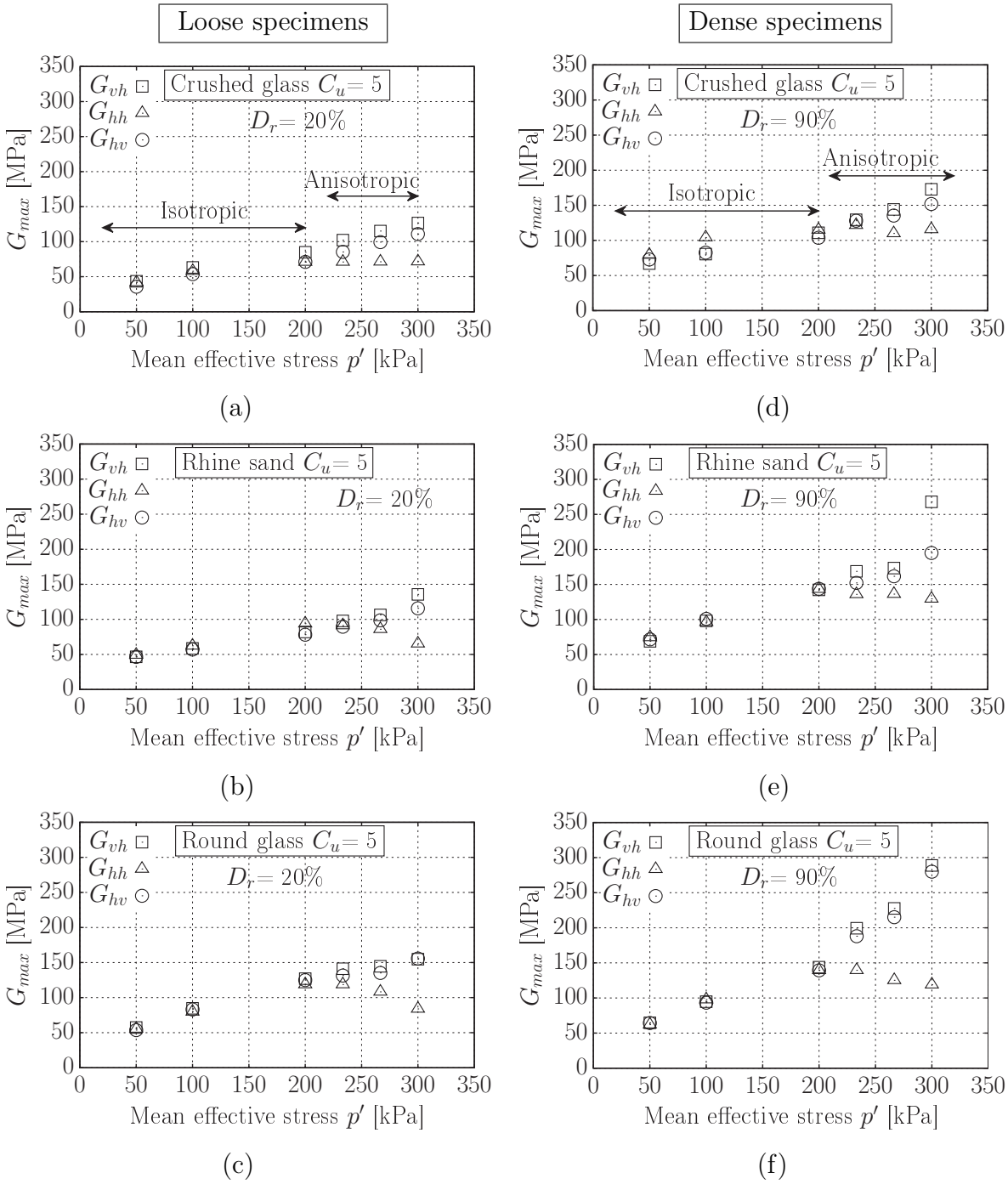

Figure 4.19: Variation of small-strain shear moduli G_{vh}, G_{hv}, and G_{hh} with respect to the mean effective stress p' for the loose specimens with the relative density of $D_r = 20\%$: (a) Crushed glass, (b) Rhine sand, (c) Round glass; and for the dense specimens with the relative density of $D_r = 90\%$: (d) Crushed glass, (e) Rhine sand, (f) Round glass.

stiffness matrix. However, the current tests show $G_{vh} \neq G_{hv}$ particularly for anisotropic stress states. Such disparity between G_{vh} and G_{hv} was also observed by other authors, e.g. Kuwano (1999) on Ham River sand. In contrary, tests carried out on a clayey silt using the same equipment showed similar values for G_{vh} and G_{hv} (Kuwano, 1999). Pennington et al. (1997) also reported similar values for G_{vh} and G_{hv} for clay tested in a triaxial cell with the piezoelectric element technique. The aforementioned studies reveal that the disparity between G_{vh} and G_{hv} could be related to soil type and particle size (Kuwano, 1999). Kuwano (1999) reported that the average of maximum shear modulus, $(G_{vh} + G_{hv})/2$ can be used for continuum approaches in case of $G_{vh} \neq G_{hv}$.

The influence of the grain shape on the shear moduli at identical void ratios and stress states is further analysed in Figure 4.20. The diagrams show the shear moduli G_{vh}, G_{hv} and G_{hh} as a function of void ratio for the isotropic stress states with $p' = 50$ and 200 kPa (Figure 4.20a, b and c) as well as for the anisotropic stress state with $q = 300$ kPa (Figure 4.20d, e and f). It should be mentioned that the range of tested void ratios of the glass beads is lower and does not intersect with the range of void ratios tested for the crushed glass. The data for Rhine sand encompass a range of void ratios showing an intersection with both the ranges for glass beads and crushed glass. For a constant void ratio, the round glass beads show lower values of all three shear moduli G_{vh}, G_{hv} and G_{hh} than the two other more angular materials, independently of the considered isotropic or anisotropic stress state. For low isotropic stresses ($p' = 50$ kPa), slightly higher shear moduli were measured for the angular crushed glass compared to the subangular Rhine sand, although the differences are not large. At higher isotropic stress level ($p' = 200$ kPa) the shear moduli of the Rhine sand exceed those of the crushed glass. For an anisotropic stress state with $q = 300$ kPa, the G_{vh} values are slightly larger for the Rhine sand compared to the crushed sand. However, there are almost no differences between these two materials with respect to G_{hv} and G_{hh}. Therefore, it may be concluded that the influence of grain shape on the small-strain stiffness does not always follow a clear trend with respect to the grain shape parameters like regularity, and that this influence also depends on the current stress state.

Figure 4.21 shows the same data as Figure 4.20, but with relative density D_r instead of void ratio e on the horizontal axes of the diagrams. For isotropic stresses (Figure 4.21a,b,c) and low relative densities, the G_{vh}, G_{hv} and G_{hh} values are largest for the round glass beads, followed by the natural Rhine sand and the angular crushed glass. These difference become more pronounced with increasing stress level (compare $p' = 50$ and 200 kPa), but decrease with increasing relative density. For high relative densities ($D_r > 60$ to 80 %) in

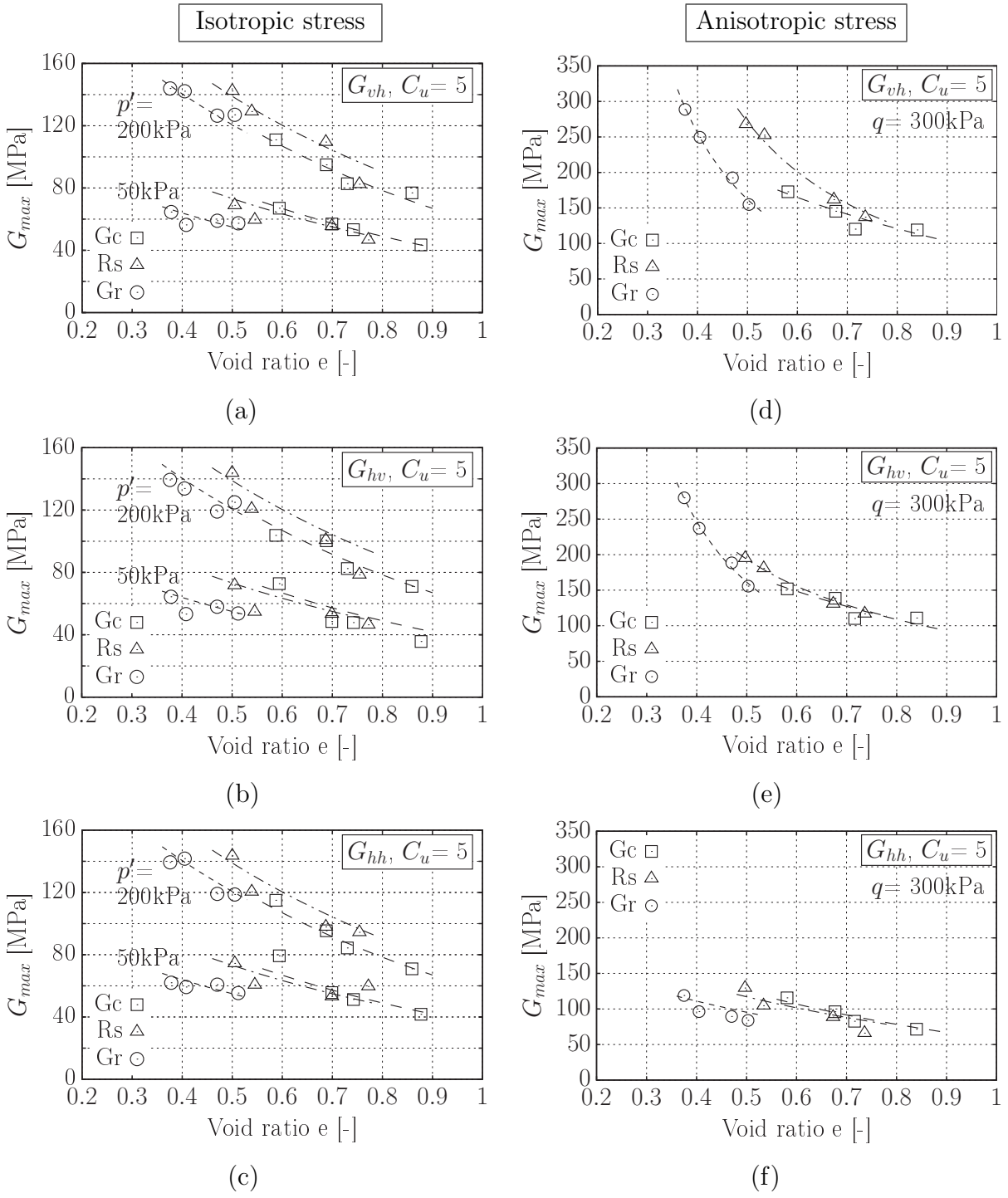

Figure 4.20: Small-strain shear moduli of the three tested materials versus void ratio e at the isotropic stress levels of $p' = 50$ and 200 kPa for: (a) G_{vh}, (b) G_{hv}, and (c) G_{hh}; under an anisotropic stress state with the deviatoric stress $q = 300$ kPa and constant $\sigma'_3 = 200$ kPa for: (d) G_{vh}, (e) G_{hv}, and (f) G_{hh}.

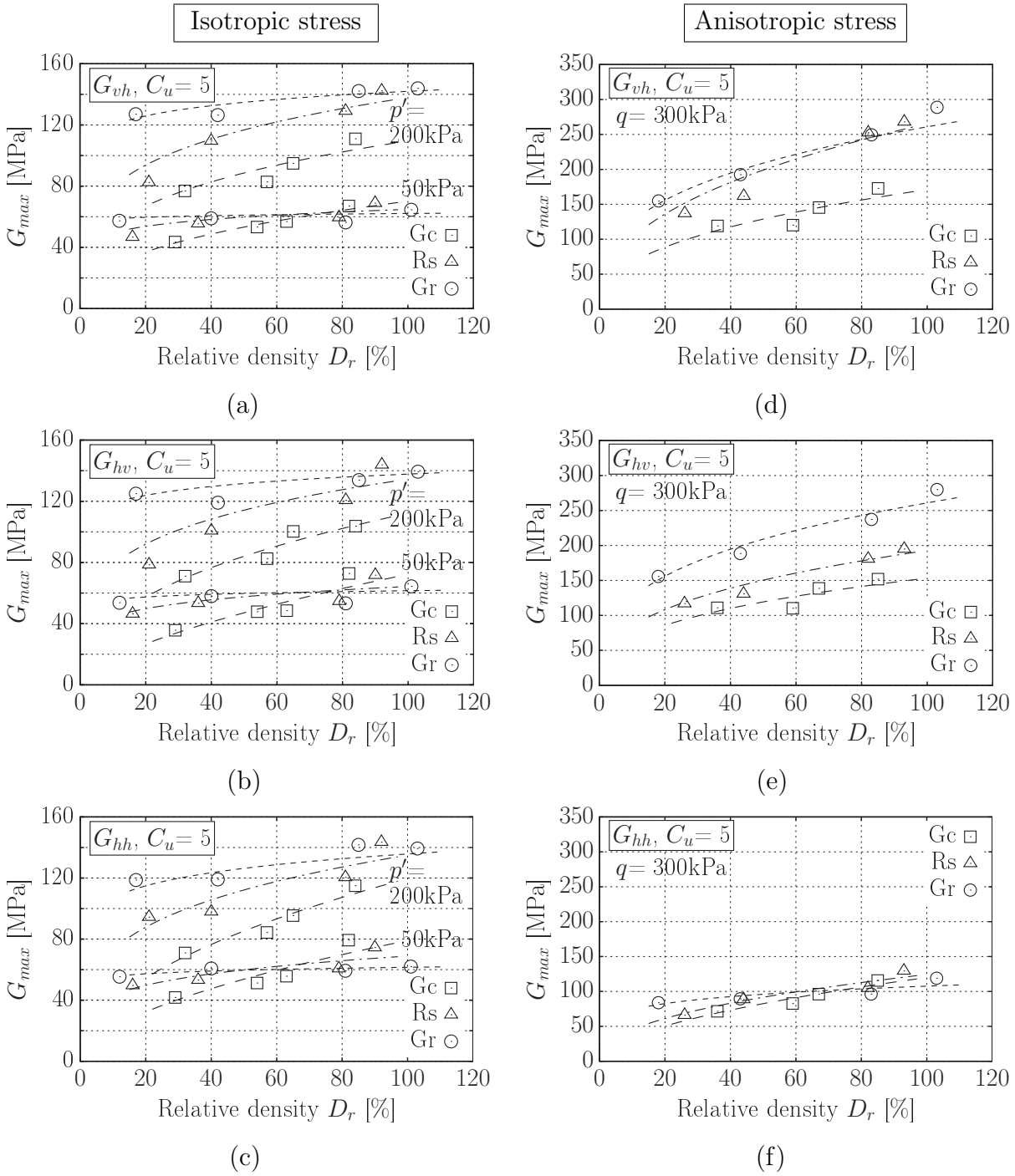

Figure 4.21: Small-strain shear moduli of the three tested materials versus relative density D_r at the isotropic stress levels of $p' = 50$ and 200 kPa for: (a) G_{vh}, (b) G_{hv}, and (c) G_{hh}; under an anisotropic stress state with the deviatoric stress $q = 300$ kPa and constant $\sigma'_3 = 200$ kPa for: (d) G_{vh}, (e) G_{hv}, and (f) G_{hh}.

combination with low pressures ($p' = 50$ kPa) the tendencies even reverse, although the differences between the three materials remain rather low. At anisotropic stresses with $q = 300$ kPa (Figure 4.21d,e,f) the picture is more diverse. The values of the shear moduli in the vertical plane, G_{vh} and G_{hv}, again show the highest values for the glass beads and the lowest ones for the crushed material. The natural sand is either in between (G_{hv}) or quite close to the glass beads (G_{vh}). In contrast, the differences between the three materials are rather small for the shear modulus measured in the horizontal plane, G_{hh}. For low relative densities the G_{hh} follow the same trend with grain shape as G_{hv} and G_{vh}, while this trend vanishes with increasing density and even reverses at high relative densities.

4.3.1.2 Influence on small-strain Young's modulus E_{max}

Due to the size of compression elements and the contact form between elements and specimens, it was impossible to install compression elements on the side surface of specimens. Therefore, Young's modulus was measured only in the vertical direction, i.e. $E_{max} = E_v$, corresponding to P wave velocity $v_{p,v}$. Figure 4.22 presents the variation of E_{max} with void ratio for the three studied materials under the different stress conditions. It is clear that E_{max} for all materials increases with increasing vertical stress σ'_1 and decreasing void ratio e for both isotropic (Figure 4.22a,b,c) and anisotropic (Figure 4.22d,e,f) stress states. Furthermore, particularly under the anisotropic stress state with $q = 300$ kPa, the E_{max} values for the round glass beads increase more rapidly with decreasing e than the ones for the angular crushed glass do. The E_{max} for the subangular particles of Rhine sand grows with a rate in between them. The dependence of E_{max} on e is also visible in Figure 4.23.

Figure 4.23 illustrates the change in E_{max} for the crushed glass, the Rhine sand and the round glass beads, respectively, along the same stress path shown in Figure 3.17. These diagrams show that E_{max} for all materials grows with increasing axial effective stress or mean effective stress, respectively. The symbols denoting the specimens with smaller void ratios are always above those denoting the specimens with larger void ratios. However, the influence of effective stress on E_{max} differs between the materials with the different particle shape. Along the same stress path, the E_{max} for the round glass beads grows with a larger rate than in case of the other materials, while the E_{max} for the angular crushed glass shows the smallest rate of increase.

The influence of grain shape on small-strain Young's modulus E_{max} for a constant void ratio can be judged based on Figure 4.24. The tendencies are very similar to those described for the shear moduli based on Figure 4.20. For the isotropic stress states, however,

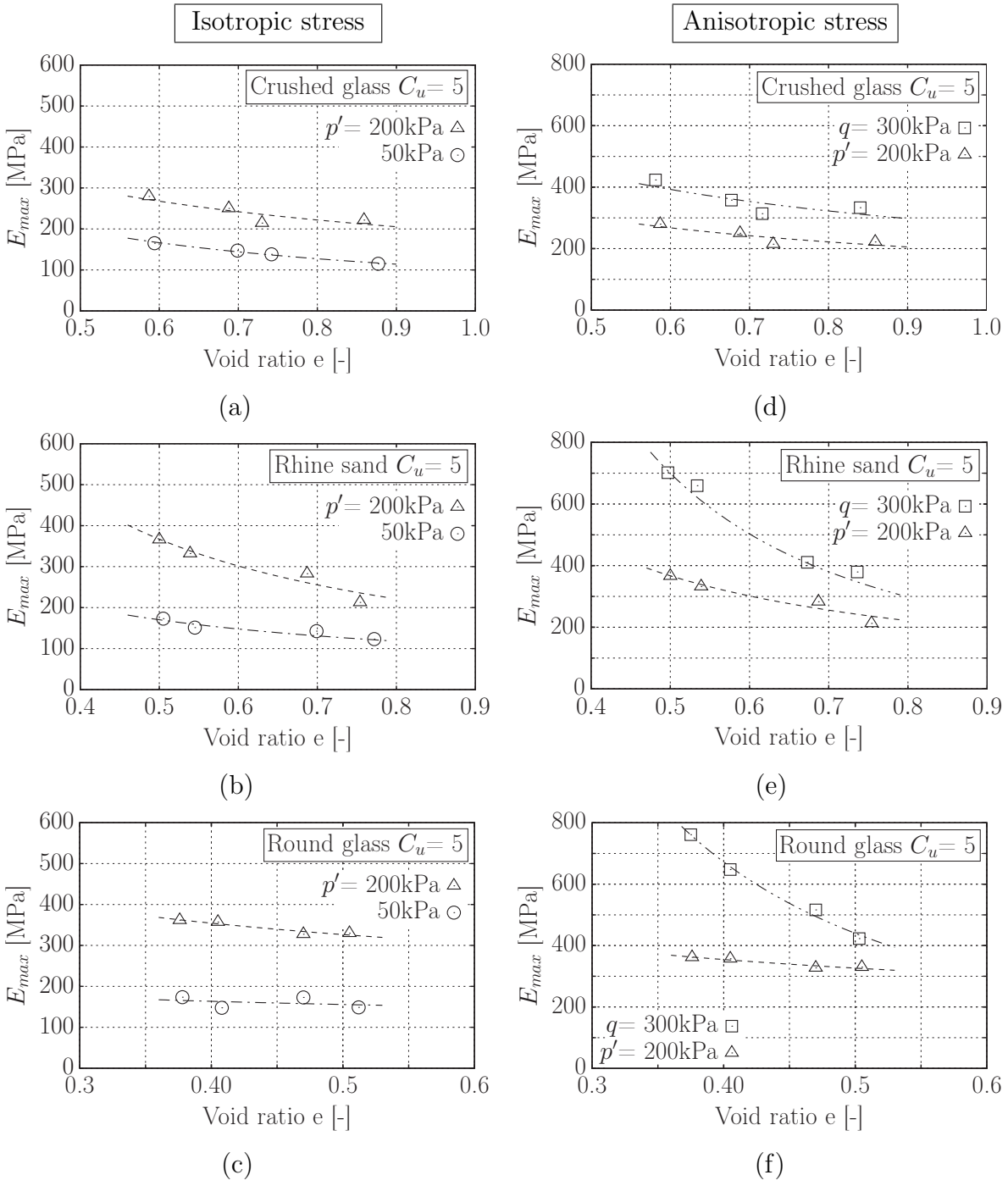

Figure 4.22: Variation of small-strain Young's modulus in the vertical direction $E_{\max}$ with respect to void ratio e at the isotropic stress levels of 50 and 200 kPa for: (a) Crushed glass, (b) Rhine sand, (c) Round glass; and under an anisotropic stress state with $q = 300$ kPa and constant $\sigma'_3 = 200$ kPa for: (d) Crushed glass, (e) Rhine sand, (f) Round glass.

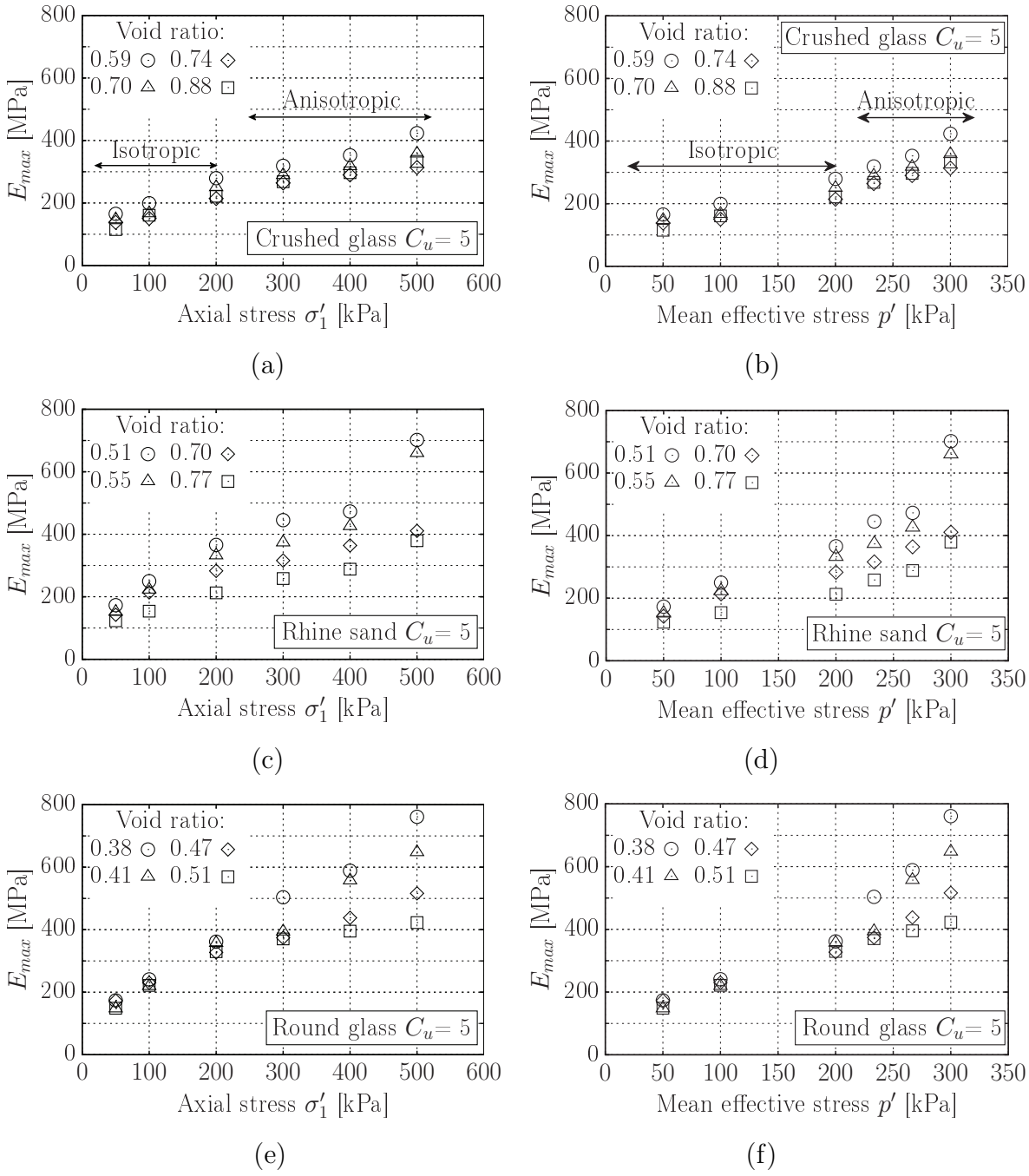

Figure 4.23: Variation of small-strain Young's modulus in the vertical direction $E_{\max}$ with respect to the effective vertical stress σ'_1 or the mean effective stress p', respectively, for various void ratios and the three tested materials: (a,b) Crushed glass, (c,d) Rhine sand, (e,f) Round glass.

the $E_{\max}$ values for the glass beads are closer to the data for both more angular materials as compared to the shear moduli.

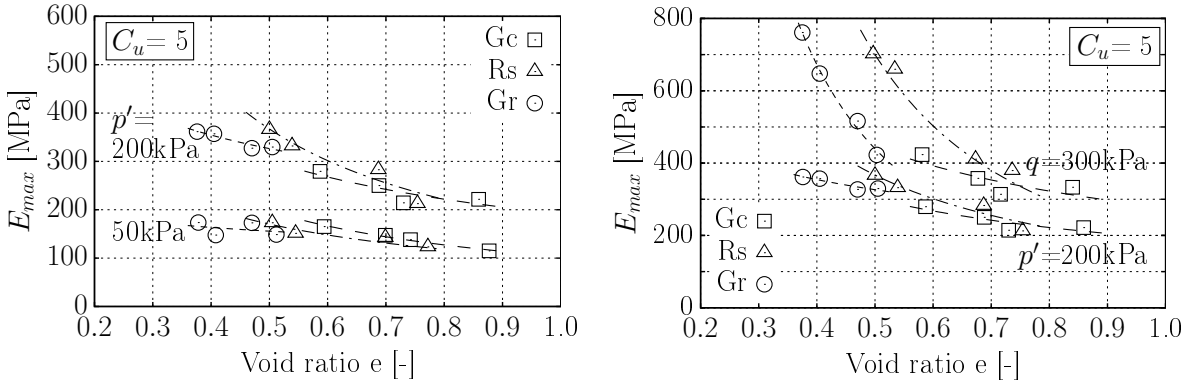

Figure 4.24: Small-strain Young's modulus of the three tested materials versus void ratio e (a) at the isotropic stress levels of $p' = 50$ and 200 kPa and (b) under an anisotropic stress state with the deviatoric stress $q = 300$ kPa.

Figure 4.25 shows the same data as Figure 4.24 but with the relative density on the horizontal axes of the diagrams. For isotropic stresses (Figure 4.24a) the $E_{\max}$ values are highest for the round glass beads, followed by the natural Rhine sand and the angular crushed glass. For low stress levels in combination with high densities these differences almost vanish, however. At anisotropic stresses (Figure 4.24b) the differences between $E_{\max}$ of the glass beads and the crushed glass even increase, while the natural sand lies closer to the glass beads.

Based on the aforementioned results, it can be concluded that the influence of grain shape on $E_{\max}$ was observed to be quite similar to that on $G_{\max}$ reported in the previous section.

4.3.1.3 Influence on Poisson's ratio ν

Poisson's ratio, ν, was determined for the vertical direction only, based on the averaged maximum shear modulus, $(G_{vh} + G_{hv})/2$, and the E_v data. Values for the well-graded mixtures of crushed glass, Rhine sand and round glass beads are provided in Figure 4.26 as functions of void ratio e. The diagrams in Figure 4.26a, b and c show the data for the isotropic stress states with $p' = 50$, 100 and 200 kPa, while those in Figure 4.26d, e and f contain the data for the anisotropic stress states with $q = 100$, 200 and 300 kPa at a constant $\sigma'_3 = 200$ kPa (along with the corresponding isotropic stress state, $q =$

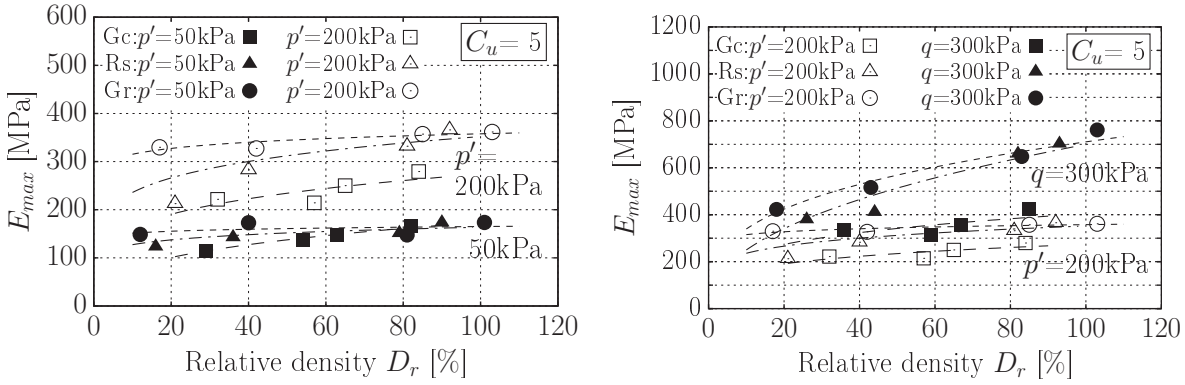

Figure 4.25: Small-strain Young's modulus of the three tested materials versus relative density D_r (a) at the isotropic stress levels of $p' = 50$ and 200 kPa and (b) under an anisotropic stress state with the deviatoric stress $q = 300$ kPa.

0). The data in Figure 4.26 shows the tendency of a slight increase of Poisson's ratio with increasing void ratio. However, there is no clear trend with increasing mean effective stress during the isotropic loading phase, or with increasing deviatoric stress during the anisotropic loading phase.

Figure 4.27a compares the Poisson's ratios for the three materials with different grain shapes at various void ratios for an isotropic stress state with $p' = 200$ kPa. Beside the small increase of ν with e, no clear influence of grain shape can be observed. In Figure 4.27b Poisson's ratio for a relative density of $D_r = 45$ % is plotted versus axial effective stress σ'_1. Also here, the influences of axial stress and grain shape seem negligible. An average value of $\nu \approx 0.3$ was observed in this study.

4.3.2 Grain size distribution

To assess the influence of the uniformity coefficient, C_u, on the dynamic stiffness of granular soils, the G_{vh}, G_{hv}, and G_{hh} as well as the $E_{max} = E_v$ values for all six materials, i.e. the mixtures of crushed glass, Rhine sand and round glass beads with either $C_u = 1.25$ or $C_u = 5$, were compared at a similar relative density $D_r = 45$ %. In Figure 4.28 the stiffness values are plotted versus the axial effective stress σ'_1, for both the isotropic and the anisotropic loading phase. Generally, the trends observed for $C_u = 1.25$ are similar to those for $C_u = 5$ that have been discussed in the previous subsections. In particular, during the anisotropic loading phase also the mixtures with $C_u = 1.25$ show a further in-

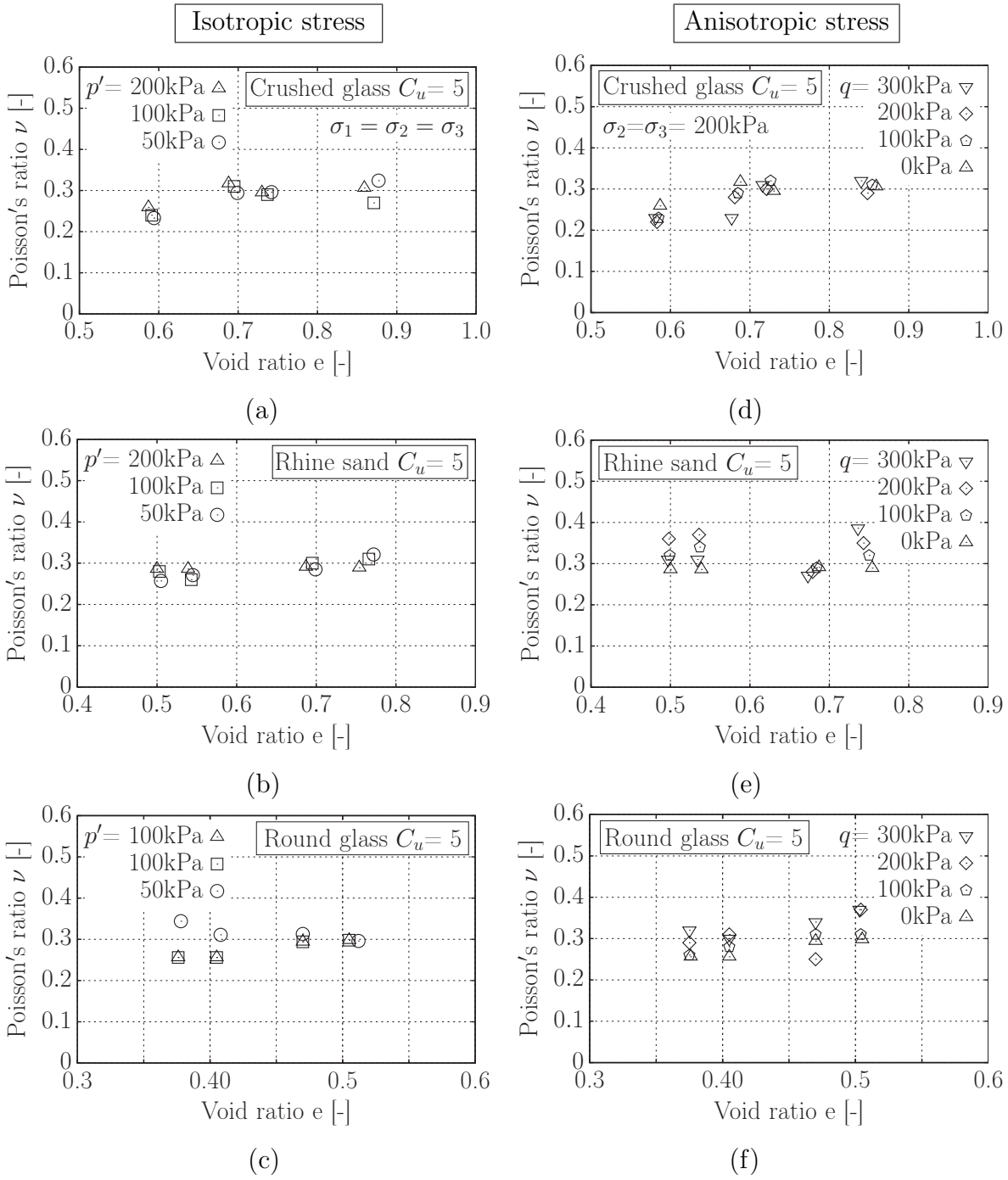

Figure 4.26: Variation of Poisson's ratio in the vertical direction ν with respect to void ratio e at the isotropic stress levels of $p' = 50$, 100, and 200 kPa for: (a) Crushed glass, (b) Rhine sand, (c) Round glass; and under various anisotropic stress states with $q = 0$, 100, 200, and 300 kPa with constant horizontal stresses $\sigma'_2 = \sigma'_3 = 200$ kPa for: (d) Crushed glass, (e) Rhine sand, (f) Round glass.

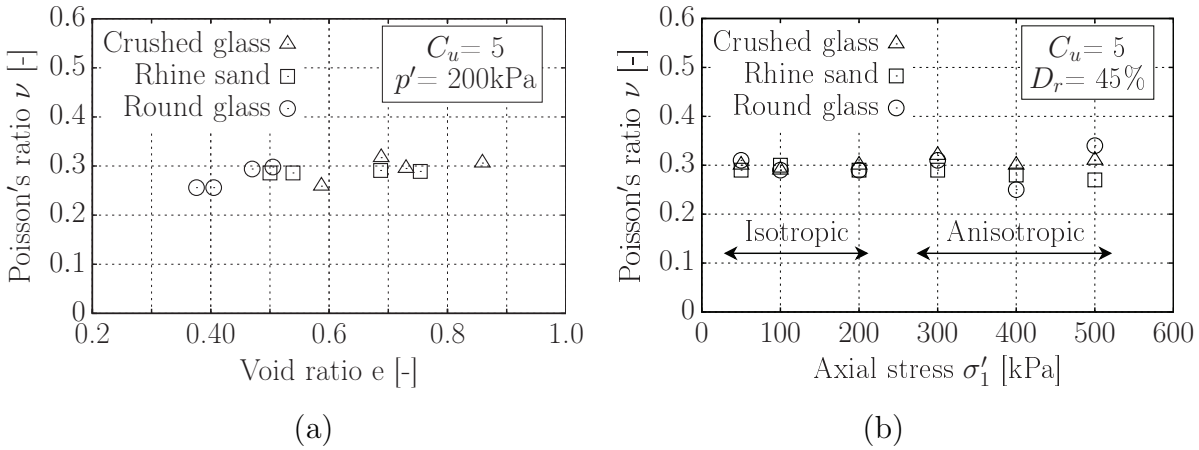

Figure 4.27: Variation of Poisson's ratio, ν for the three well-graded materials with different grain shape, (a) against void ratio for an isotropic stress state with $p' = 200$ kPa, and (b) versus axial stress σ_1' for a relative density $D_r = 45$ %.

crease of G_{vh}, while G_{hh} is slightly reduced with increasing deviatoric stress. For crushed glass and Rhine sand, the values of G_{vh}, G_{hh} and $E_{\max}$ for the uniformly graded mixtures ($C_u = 1.25$) are slightly larger than for the well-graded material ($C_u = 5$). The difference becomes slightly more pronounced under anisotropic stress conditions, in particular with respect to G_{vh} and $E_{\max}$. The data for glass beads shows almost similar stiffness values for $C_u = 1.25$ and $C_u = 5$, i.e. the influence of the uniformity coefficient seems negligible for materials with spherical and round particles.

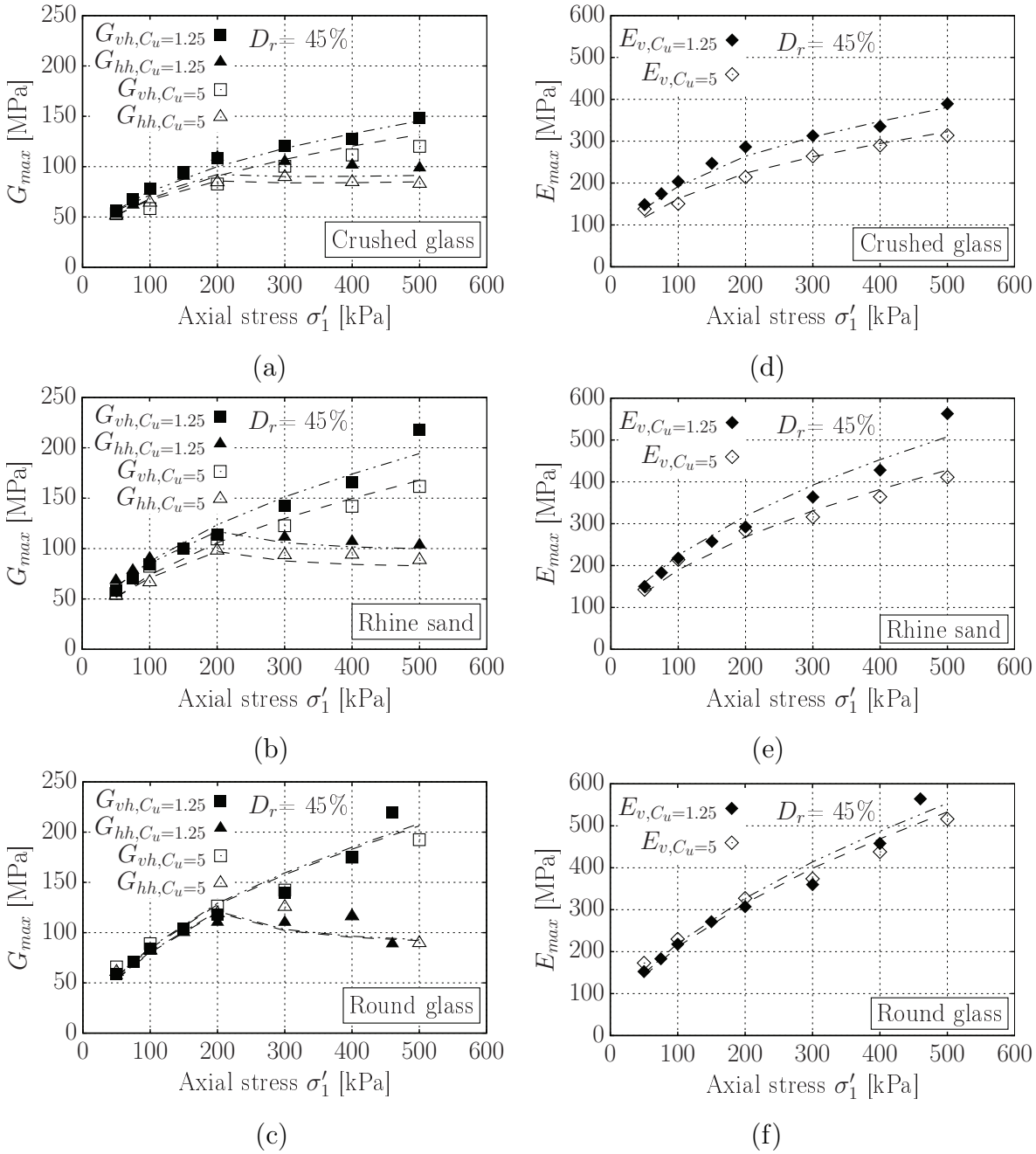

Figure 4.28: Influence of the uniformity coefficient, $C_u = 1.25$ and 5, on the maximum shear moduli, G_{vh} and G_{hh}, for: (a) Crushed glass, (b) Rhine sand, (c) Round glass; and on the small-strain Young's modulus, $E_{\max} = E_v$, for: (d) Crushed glass, (e) Rhine sand, (f) Round glass.

5 Empirical equations

In this chapter the experimental results presented in the last chapter are further analyzed in the framework of empirical relationships. Hardin & Black (1966) proposed one of the most widely used empirical relations (Equation 5.1) describing the maximum shear modulus, $G_{\max}$, as a function of void ratio, e, and mean effective stress, p':

$$G_{\max} = A\ p_a\ f(e) \left(\frac{p'}{p_a}\right)^n \tag{5.1}$$

where, A is a material constant, p_a is the atmospheric pressure (≈ 100 kPa), n is the stress exponent (another material constant), and $f(e)$ is the void ratio function, commonly found in form of Equation 5.2 (Hardin & Black, 1966) or Equation 5.3 (Jamiolkowski et al., 1991):

$$f(e) = \frac{(c-e)^2}{1+e} \tag{5.2}$$

$$f(e) = e^{-x} \tag{5.3}$$

where, c and x are further material constants, which are sometimes related to the angularity of particles (e.g. $c = 2.97$ for angular sands and $c = 2.17$ for rounded sands proposed by Hardin & Black (1966)).

Equation 5.1 is used as the basis for the analysis of the experimental data in the following. It has been fitted to the data from the different test series. Based on the variation of the material constants, the effects of soil fabric, stress states and particle characteristics are discussed in this chapter. An extension of Equation 5.1 for anisotropic stress states is also proposed.

5.1 Effect of sample preparation method

In this section the data of the test series on Hostun sand with the two different sample preparation methods Air Pluviation (AP) and Moist Tamping (MT) documented in Section 4.1 are further analysed.

5.1.1 Void ratio function

The goal of this section is to determine the effect of the sample preparation method (initial fabric of specimens) on the fitting parameters of Hardin's relationship (Equation 5.1). To achieve this goal, the plots of small-strain shear modulus $G_{\max}$ versus void ratio e for mean effective stresses of $p' = 50$, 100 and 200 kPa were utilized (Figure 4.1). The procedure for determining the fitting parameters follows the method described by Goudarzy et al. (2018).

In a first step, the function of void ratio, $f(e)$, shown in Equation 5.2 was fitted to the experimental data points in the $G_{\max} - e$ space individually for each stress level and each sample preparation method (Figure 5.1). For a given stress level, the function of stress, $(p'/p_a)^n$, shown in Equation 5.1 can be considered as a constant value, although the stress exponent, n, is unknown. Thus, the empirical relationship can be simplified in the form $G_{\max} = kf(e)$, where k is a fitting parameter. The values of the parameter c for each stress level were determined by maximizing the determination coefficient, R^2, and are presented in Table 5.1 with respect to each stress level. The average value was afterwards adopted as the best value for the parameter c in Equation 5.2. These values were $c = 2.12$ for the air pluviation (AP) and $c = 1.67$ for the moist tamping (MT) method, reflecting the slightly different dependence of $G_{\max}$ on e for the two preparation methods. Figure 5.1 shows that the lines in form of $kf(e)$ with the average values of c match well the experimental data points obtained from the specimens prepared by the AP or MT method, respectively.

5.1.2 Stress function

Isotropic loading

In a next step, the $G_{\max}$ was normalized with respect to the void ratio function $f(e)$. For the specimens prepared by the AP and MT methods, the parameter c was adopted as 2.12 and 1.67, respectively. The normalized $G_{\max}/f(e)$ was drawn with respect to the

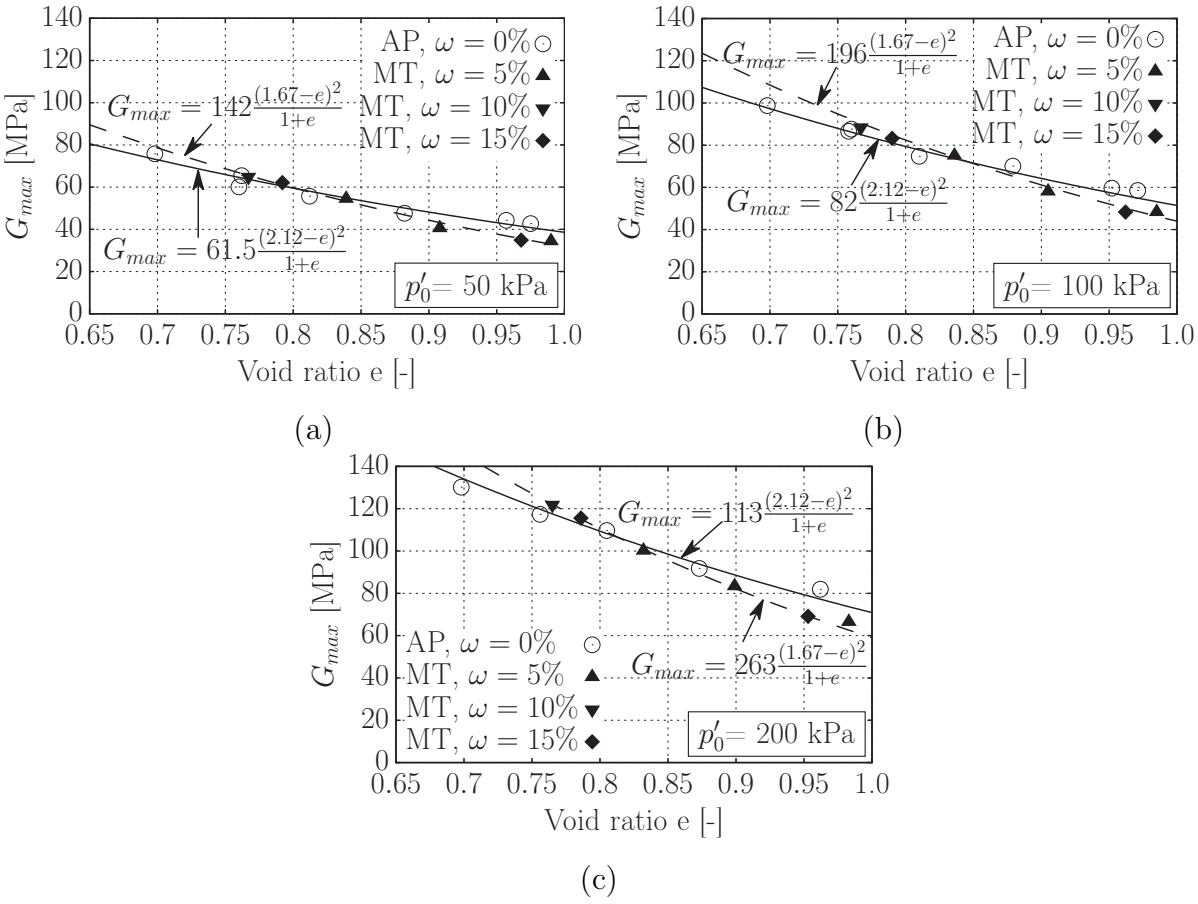

Figure 5.1: Small-strain shear modulus $G_{\max}$ versus void ratio, e, for different mean effective stresses p'. The fitting lines are in form of $G_{\max} = k\frac{(c-e)^2}{(1+e)}$, $c_{AP} = 2.12$ for specimens prepared by the air pluviation (AP) method (solid lines), $c_{MT} = 1.67$ for specimens prepared by the moist tamping (MT) method (dashed lines): (a) $p' = 50$ kPa, (b) $p' = 100$ kPa, (c) $p' = 200$ kPa.

mean effective stress p', as shown in Figure 5.2. Evidently, the normalized data for the samples prepared by moist tamping are significantly larger than those for the air pluviation method. The other fitting parameters A and n of Equation 5.1 were determined from a power regression of these data for getting the maximum R^2.

Table 5.1 shows the summary of the determined fitting parameters for the specimens prepared by the two different methods. As can be seen in Table 5.1, there is a difference between the average values of the fitting parameters A and c for the specimens prepared by the AP and MT methods. However, the preparation method seems to have no significant effect on the stress exponent n, which was about 0.44 for both preparation methods.

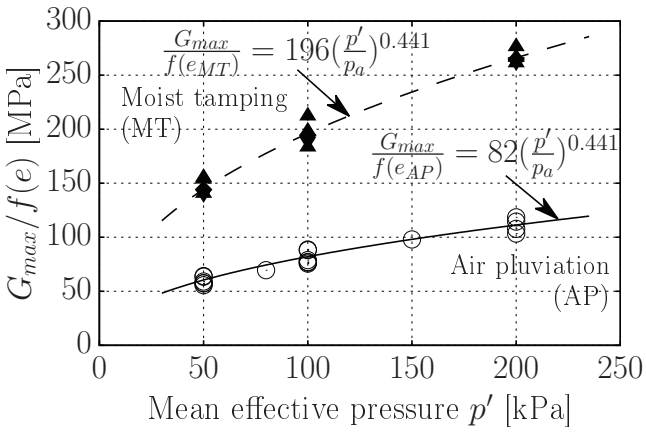

Figure 5.2: Normalized small-strain shear modulus $G_{\max}/f(e)$ versus mean effective stress, p', for the two applied sample preparation methods AP and MT. The fitting curves are in form of $G_{\max}/f(e) = A\,(p'/p_a)^n$.

Table 5.1: Determined fitting parameters of Equation 5.1 for the specimens prepared using: (a) AP method, (b) MT method.

(a)

p' [kPa]	k [MPa]	c [-]	A [-]	n [-]
50	60	2.13		
100	84	2.11		
200	111	2.12		
Average	-	2.12	0.82	0.441

(b)

p' [kPa]	k [MPa]	c [-]	A [-]	n [-]
50	142	1.66		
100	184	1.65		
200	249	1.70		
Average	-	1.67	1.96	0.441

In Figure 5.3 the values of maximum shear modulus, $G_{\max}$, measured in the current study on specimens prepared by the AP method, are compared with those from previous investigations using Hostun sand (Ezaoui & Di Benedetto, 2009; Sadek et al., 2007; Azeiteiro et al., 2017; Goudarzy et al., 2016b) in order to confirm the results. The comparison is

done in two diagrams showing the same data but using different scales (linear or logarithmic) on the axes. For the comparison, the $G_{\max}$ data were all normalized with the function of void ratio, $f(e) = \frac{(c-e)^2}{1+e}$, using the constant parameter $c = 2.12$ determined in the current study. The material constants A, c and n from the current study for AP were also used to draw the solid line in Figure 5.3. It can be seen that the results from the current study agree well with those from the previous ones.

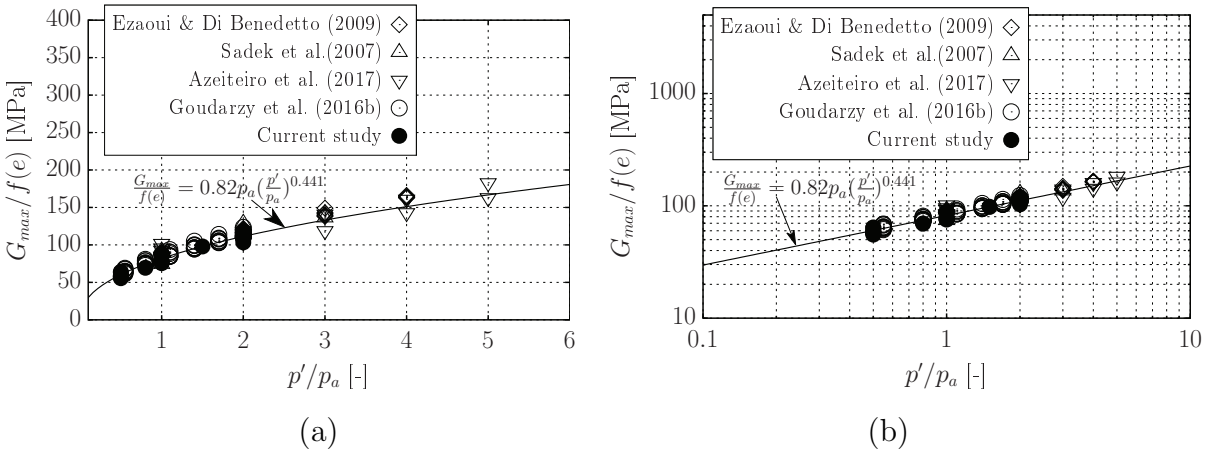

Figure 5.3: Normalized small-strain shear modulus, $G_{\max}/f(e)$, versus normalized mean effective stress, p'/p_a, comparing the results of the current study with those from previous investigations on Hostun sand, using diagrams with (a) linear scale, (b) log-log scale.

Anisotropic loading at the axial strain of 24%

Figure 5.4a shows the state of the AP and MT specimens at the axial strain of 24% (the filled circles). A regression analysis was performed to fit Equation 5.4 (for the maximum R^2) to these steady state / critical state data points. In Equation 5.4, $e_{\lim}$ is the limiting value corresponding to $p' = 0$ kPa, p_a is the atmospheric pressure, and λ_{ss} and ζ are the curve fitting parameters. From the performed regression, the values of $e_{\lim}$, λ_{ss} and ζ are 1.023, 0.094 and 0.254, respectively.

$$e = e_{\lim} - \lambda_{ss} \left(\frac{p'}{p_a} \right)^{\zeta} \tag{5.4}$$

Furthermore, the comparison with steady state / critical state data or equations determined for Hostun sand in previous studies in the literature (Figure 5.5) shows a very good agreement, confirming the results of the current experimental study.

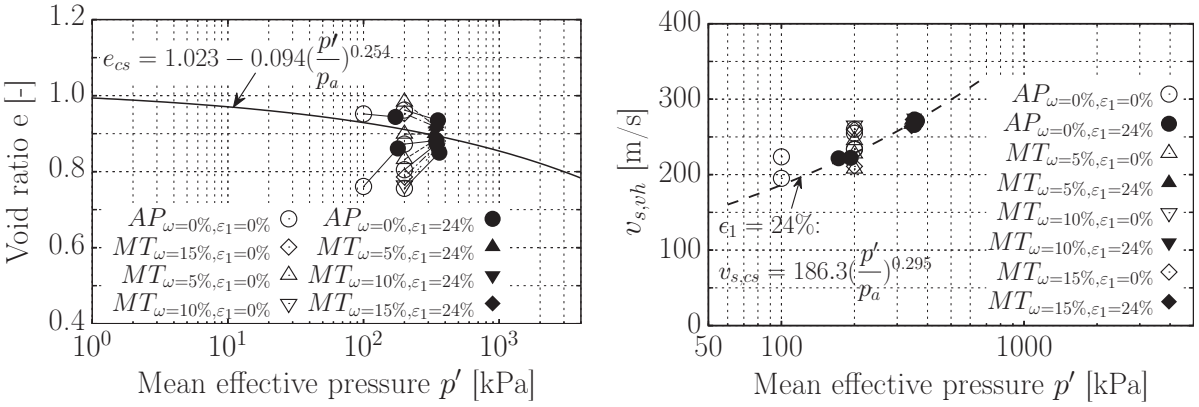

Figure 5.4: Measurements at the axial strain of $\varepsilon_1 = 24\%$ with respect to the mean effective stress, p': (a) Void ratio, e, versus p'; (b) Shear wave velocity, $v_{s,vh}$, versus p'. Void ratios after isotropic consolidation are denoted as empty symbols, those measured at $\varepsilon_1 = 24\%$ are denoted as filled symbols. Dashed line shows the best fitting line on the solid points for $v_{s,vh}$ at $\varepsilon_1 = 24\%$.

Figure 5.4b shows the shear wave velocity $v_{s,vh}$ at the initial state of the tests and at the axial strain of 24% versus the mean effective stress p'. Evidently, $v_{s,vh}$ at $\varepsilon_1 = 24\%$ is independent of the initial void ratio e and the sample preparation method, i.e. a unique curve of $v_{s,vh}$ versus p' is obtained. It can be fitted by an equation of the form

$$v_{s,vh} = K \left(\frac{p'}{p_a} \right)^m \tag{5.5}$$

The best fit is shown as dashed line in Figure 5.4b, leading to parameters of $K = 186.3$ m/s and $m = 0.295$. The results in Figure 5.4b show that the shear wave velocity measured at the axial strain of 24%, which could be close to or at the steady state / critical state line (CSL), is only a function of the mean effective stress.

5.2 Effect of stress state

In this section the data of the test series on air-pluviated samples of Hostun sand with isotropic consolidation followed by undrained shearing documented in Section 4.2 are further analysed. Data from the isotropic loading stages of the tests performed on the AP specimens from Section 4.1 are also included.

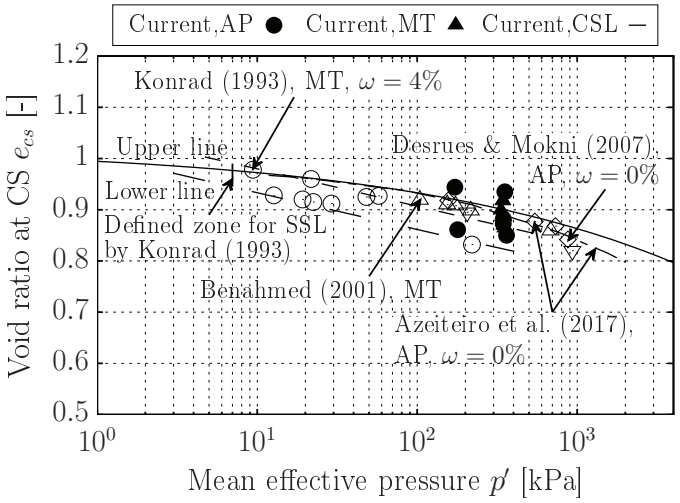

Figure 5.5: Comparison with the measurements and the CSL for Hostun sand from previous literature. The filled symbols and the solid line denote the measurements and the best-fit CSL obtained in the current study. The empty symbols and the dashed lines denote the measurements and the CSL proposed by the previous studies.

5.2.1 Isotropic stress states

The data of the small-strain shear modulus $G_{\max}$ obtained at the isotropic consolidation stages before the undrained or drained shearing are plotted versus void ratio in Figure 5.6. The fitting of Equation 5.1 to the data follows the same procedure as described in the previous section. The fitting lines in Figure 5.6a were drawn using the void ratio function $f(e)$ according to Equation 5.2 with the parameters presented in Table 5.1a, thus the parameters already determined in the previous section. Figure 5.6b shows the same data with fitting lines plotted applying the alternative void ratio function $f(e)$ from Equation 5.3. The fitting parameters in the empirical equation are summarized in Table 5.2a. It can be concluded that both void ratio functions are suitable to approximate the data well. There is no significant difference in the prediction quality of both functions.

The corresponding shear wave velocities $v_s = v_{s,vh}$ (Figure 5.8a) can be described by a relationship similar to Hardin's equation 5.1 employing Equation 5.3 for $f(e)$:

$$v_s = K\ p_a\ f(e) \left(\frac{p'}{p_a}\right)^n \tag{5.6}$$

The fitting of the data of shear wave velocity by Equation 5.6 was done in a similar way as in the case of the small-strain shear modulus (Figure 5.8a). The resulting parameters

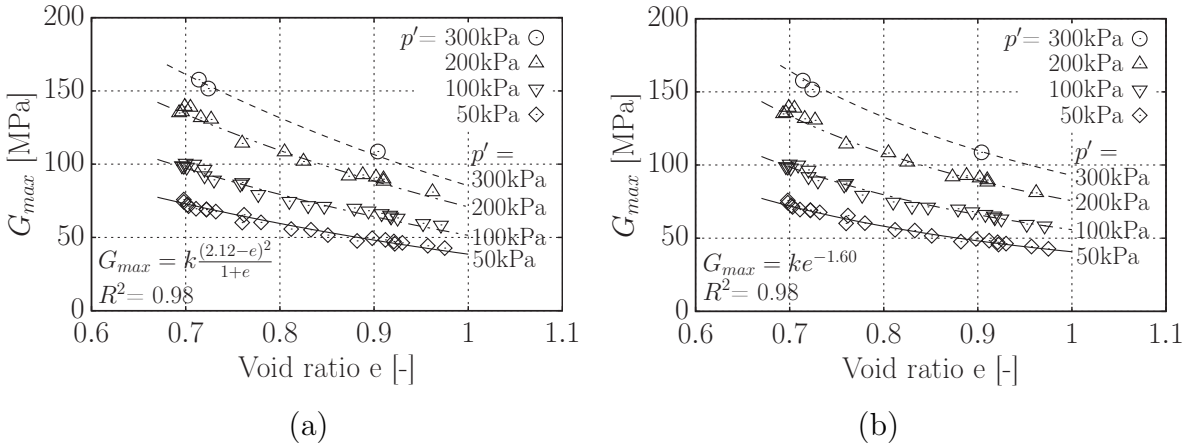

Figure 5.6: Small-strain shear modulus $G_{\max}$ versus void ratio, e, for different mean effective stresses, p', fitted with different void ratio functions: (a) The fitting lines are in form of $G_{\max} = k\frac{(c-e)^2}{(1+e)}$ with $c = 2.12$, (b) The fitting lines are in form of $G_{\max} = ke^{-x}$ with $x = 1.60$.

are presented in Table 5.2b. Comparing Tables 5.2a and 5.2b, the parameter x of the void ratio function is significantly lower for v_s than for $G_{\max}$ (0.58 vs. 1.60). Furthermore, the stress exponent n for v_s is only about half the value for $G_{\max}$ (0.247 vs. 0.441). This is in good agreement with the general relationship between the elastic stiffness and the wave velocity.

5.2.2 Anisotropic stress states

As can be seen in Equation 5.1 or 5.6, empirical relationships for the elastic stiffness or wave velocities are usually considering the primary influencing factors void ratio, e, and mean effective stress, p', and only seldomly the stress anisotropy. In the following the influence of an anisotropic stress state on the shear wave velocity is analysed based on the v_s measurements during the undrained shearing phase of the tests on Hostun sand.

Four significant stages of these tests were considered in the analysis, which are related to the effective stress path (Figure 5.7): the initial stage (isotropic consolidation stress), the instability point (deviatoric stress reaches a local maximum before it drops again), the phase transformation point (change from contractive to dilative volumetric response) and the final stage (at large strain). These stages are indicated with straight lines in Figure 5.8b, c and d, showing the effective stress paths measured for the initial mean effective stresses of $p'_0 = 100$, 200 and 300 kPa, respectively, for the specimens with different relative

Table 5.2: Determined fitting parameters with the void ratio function 5.3 (Jamiolkowski et al., 1991) for specimens of Hostun sand prepared using the AP method: (a) Equation 5.1 for $G_{\max}$ in MPa, (b) Equation 5.6 for v_s in m/s.

(a)

p' [kPa]	k [MPa]	x [-]	A [-]	n_x [-]
50	40.7	1.62		
100	55.8	1.59		
200	75.6	1.65		
300	92.9	1.54		
Average	-	1.60	0.56	0.441

(b)

p' [kPa]	k [MPa]	x [-]	K [-]	n_x [-]
50	163.1	0.57		
100	190.2	0.58		
200	221.7	0.61		
300	245.7	0.56		
Average	-	0.58	1.90	0.247

densities. The $v_{s,vh}$ measurements taken at the stress states along these lines were used to study the effect of the stress anisotropy on the shear wave velocity. It must be noted that the phase transformation point varies with varying relative density (Wichtmann, 2016). The straight lines in Figure 5.8 indicate schematically the stress stages where the analyzed data were obtained.

The analysis of the shear wave velocity at the four different stages is presented in Figure 5.9. All of the measurements are normalized with the void ratio function $f(e) = e^{-x}$ using $x = 0.581$, and are plotted against the normalized mean effective stress, p'/p_a. Figure 5.9a shows the result for the wave velocity measured after the isotropic consolidation. It can be seen that the stress exponent $n = 0.247$ for the shear wave velocity obtained for that stage is about half of the one for the stiffness shown in Figure 5.3, which matches the relation between velocity and stiffness. However, the stress exponents obtained for the other stages are obviously different. The stress exponent increases from the isotropic state A ($n = 0.247$, Figure 5.9a) to the instability point B ($n = 0.317$, Figure 5.9b), drops to the phase transformation point C ($n = 0.263$, Figure 5.9c) and increases again up to the

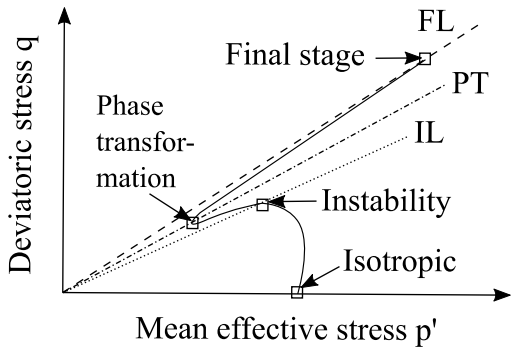

Figure 5.7: Four characteristic points of the effective stress path: isotropic consolidation, instability point, phase transformation point, final stage

final stage ($n = 0.263$, Figure 5.9d). The comparison in Figure 5.10 confirms differences in the normalized shear wave velocity $v_{s,vh}/f(e)$ at the four different stages when plotted versus normalized mean effective stress p'/p_a. It seems that the effect of stress anisotropy should be taken into consideration in the prediction of the small-strain shear stiffness or shear wave velocity, respectively.

Therefore, a function of the stress ratio, q/p', was introduced in the empirical equation to describe the effect of stress anisotropy on shear wave velocity, as can be seen in Equation 5.7:

$$v_s = B\ p_a\ f(e) \left(\frac{p'}{p_a}\right)^n \left(1 + \frac{q}{p'}\right)^m \qquad \text{with} : f(e) = e^{-x} \tag{5.7}$$

At the final step, the exponent m describing the dependence of the shear wave velocity on the stress ratio q/p' in Equation 5.7 was obtained from a fitting of the experimental data. For that purpose the normalized shear wave velocities in the form $\frac{v_s}{e^{-x}\,(p'/p_a)^n}$ with $x = 0.58$ and $n = 0.247$ for all stages shown in Figure 5.9 were plotted versus the stress ratio q/p', as shown in Figure 5.11. An exponent $m = 0.103$ was obtained from the fitting. In Figure 5.11, most data points are distributed in a zone close to the fitting line, confirming the suitability of Equation 5.7.

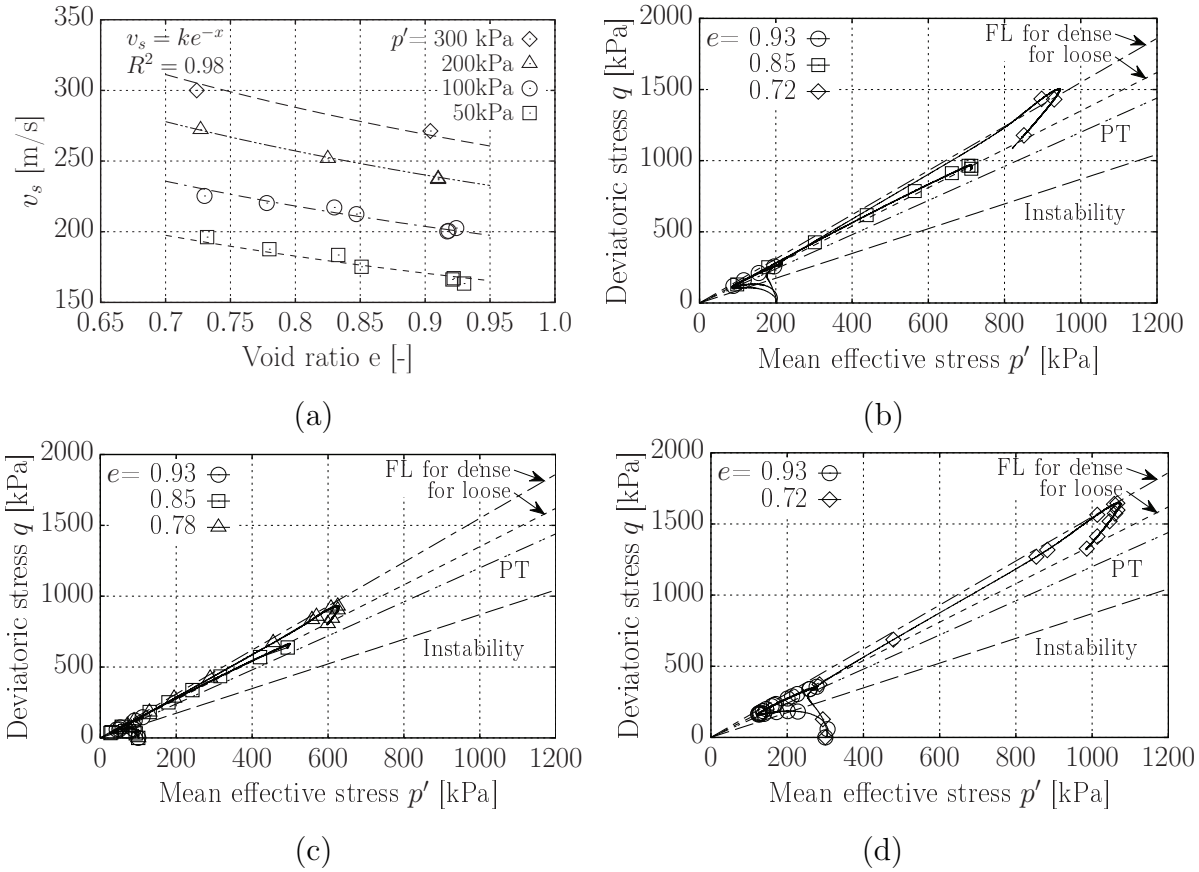

Figure 5.8: Results obtained from triaxial compression tests under undrained conditions. (a) Determination of fitting parameter of the void ratio function, $f(e)$, based on the v_s measurements under isotropic stress states of 50, 100, 200, 300 kPa. And effective stress paths of the tests conducted on the specimens prepared at various void ratios ($0.72 \leq e \leq 0.93$) at the initial mean effective stress, p'_0, of: (b) 100 kPa, (c) 200 kPa, (d) 300 kPa. The dashed lines show the stress ratio at which the shear wave velocities measured were used to study the effect of stress anisotropy on shear wave velocity.

5.3 Effect of grain shape and gradation

In this section the data of the test series on the three materials with significantly different grain shape, i.e. crushed glass, Rhine sand and round glass beads, documented in Section 4.3, are further analysed.

To predict the maximum moduli, $G_{\max} = G_{vh}$ and $E_{\max} = E_v$ for both isotropic and anisotropic stress states, Equation 5.1 was extended in the following way, as can be seen in Equations 5.8 and 5.9:

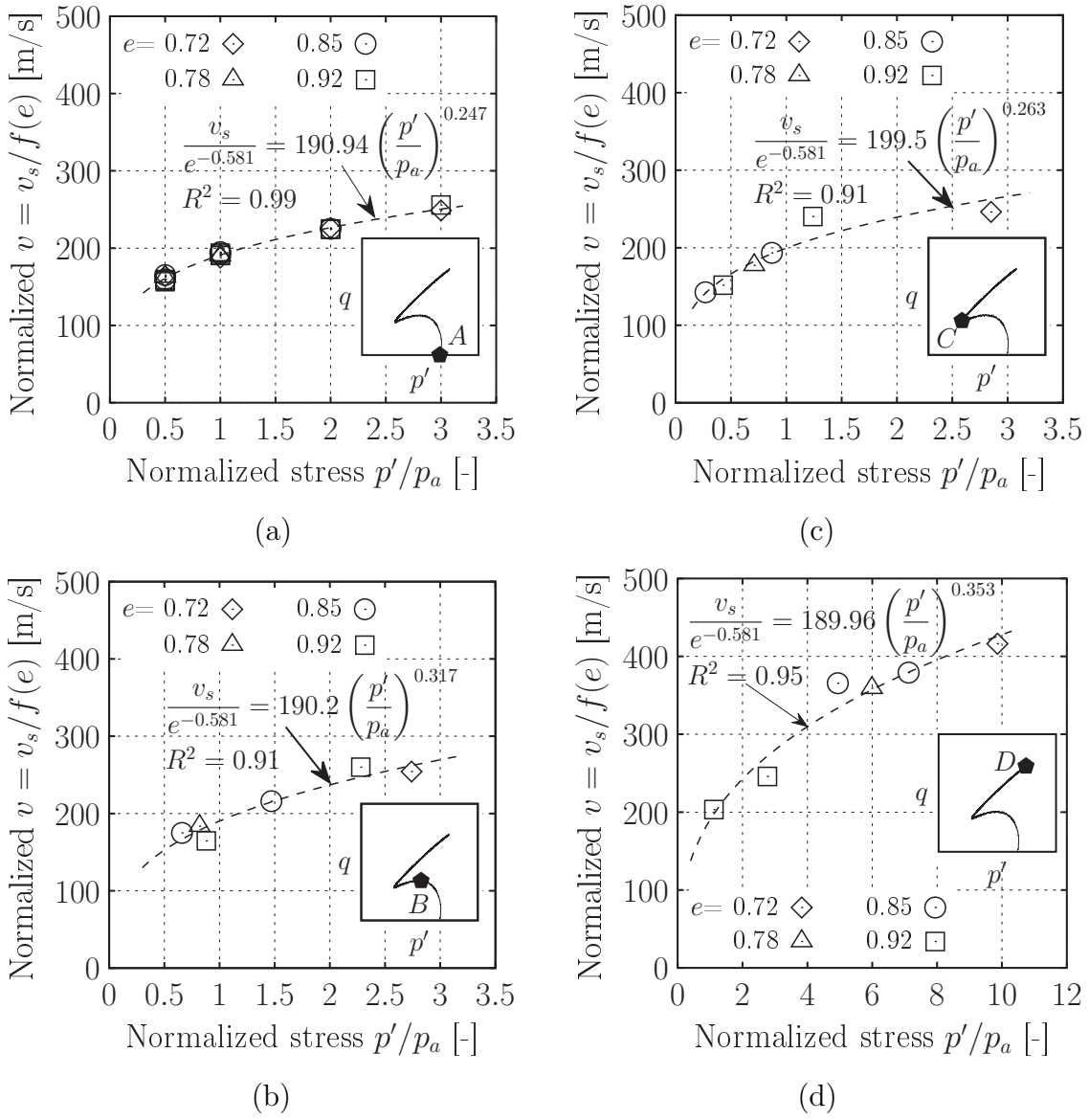

Figure 5.9: Normalized shear wave velocity $v_{s,vh}/f(e)$ versus normalized mean effective stress p'/p_a at four different stages during the undrained shearing phase: (a) after isotropic consolidation, (b) at the instability point, (c) at phase transformation, and (d) at the final stage of the tests ($\varepsilon_1 \approx 24\%$). The dashed lines were fitted in form of $v_s/e^{-x} = B\,(p'/p_a)^n$.

$$G_{\max} = A_G\ p_a\ \frac{(X_G - e)^2}{1+e} \left(\frac{p'}{p_a}\right)^{n_G} \left(1 + \frac{q}{p'}\right)^{m_G} \tag{5.8}$$

$$E_{\max} = A_E\ p_a\ \frac{(X_E - e)^2}{1+e} \left(\frac{p'}{p_a}\right)^{n_E} \left(1 + \frac{q}{p'}\right)^{m_E} \tag{5.9}$$

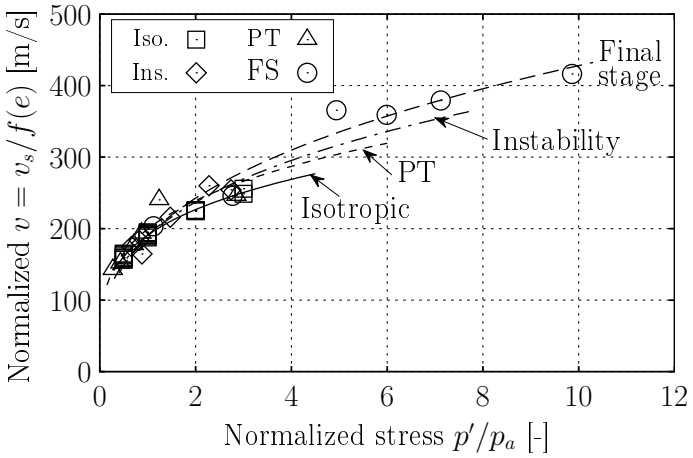

Figure 5.10: Comparison of normalized shear wave velocity $v_{s,vh}/f(e)$ versus normalized mean effective stress p'/p_a at the four different stages.

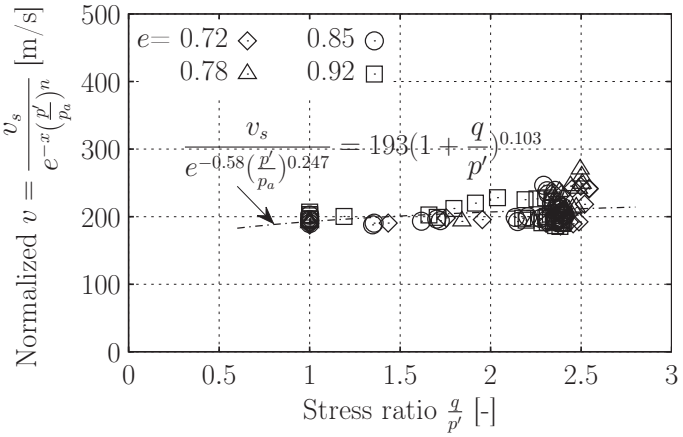

Figure 5.11: Normalized shear wave velocity, $\frac{v_s}{e^{-x(p'/p_a)^n}}$, versus stress ratio, q/p'. The fitting line follows the relationship $\frac{v_s}{e^{-x(p'/p_a)^n}} = B\,(1+q/p')^m$

Poisson's ratio can be obtained from $\nu = \frac{E_{\max}}{2G_{\max}} - 1$.

The fitting parameters A_G, X_G, n_G and m_G for $G_{\max}$, as well as A_E, X_E, n_E and m_E for $E_{\max}$ were determined for the well-graded mixtures of the three different materials with $C_u = 5$ in a similar way as described for the Hostun sand in the previous sections. The parameters are summarized in Table 5.3. The dependence of the fitting parameters on grain shape, described by regularity ρ, is presented in Figure 5.12. A decrease in A_G and an increase in A_E with increasing regularity, ρ, is evident in Figure 5.12a and b. The fitting parameter x_G of the void ratio function slightly increases with ρ (Figure 5.9c) while x_E slightly decreases (Figure 5.12d). Both the exponents n_G and n_E for the influence

Table 5.3: Summary of the fitting parameters of Equations 5.8 and 5.9 for the three granular materials with different grain shape

Material	Regularity	For G_{max}				For E_{max}			
	ρ	A_G	X_G	n_G	m_G	A_E	X_E	n_E	m_E
	[-]	[-]	[-]	[-]	[-]	[-]	[-]	[-]	[-]
Crushed glass	0.45	0.282	2.77	0.45	0.15	0.352	3.67	0.46	0.13
Rhine sand	0.60	0.203	3.08	0.51	0.28	0.560	3.12	0.52	0.23
Round glass	0.90	0.221	2.83	0.60	0.17	0.581	2.81	0.58	0.21

of isotropic stress and the stress anisotropy exponents m_G and m_E show a tendency to increase with ρ, which is, however, less pronounced for the m values (Figure 5.12e and f). In can be further noted that the parameters X of the void ratio function and the stress exponents n and m have similar magnitudes for G_{max} and E_{max}.

Finally, the prediction quality of the extended empirical equations 5.8 and 5.9 was inspected. Figure 5.13 shows the comparison of the measured and predicted values for G_{max}, E_{max} and Poisson's ratio ν for the three materials adopted in this study. It can be seen that all of the data points fall into a narrow zone around the line $y = x$, confirming the good prediction quality.

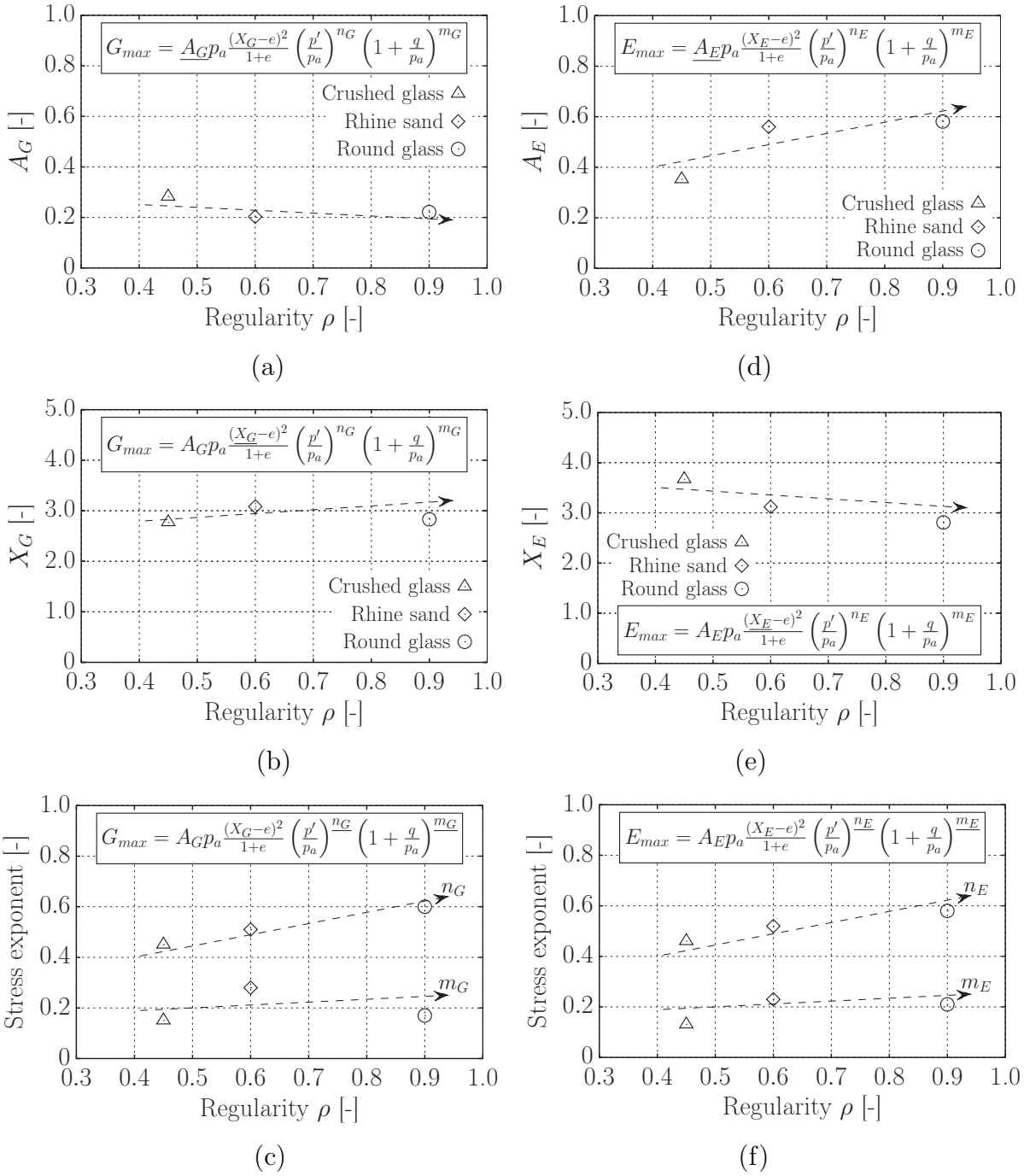

Figure 5.12: Fitting parameters of Equations 5.8 and 5.9 plotted against grain shape parameter regularity, ρ. For $G_{\max}$: (a) material constant A_G (b) constant of the void ratio function X_G (c) stress exponents n_G and m_G; For $E_{\max}$: (d) material constant A_E, (e) constant of the void ratio function X_E, (f) stress exponents n_E and m_E.

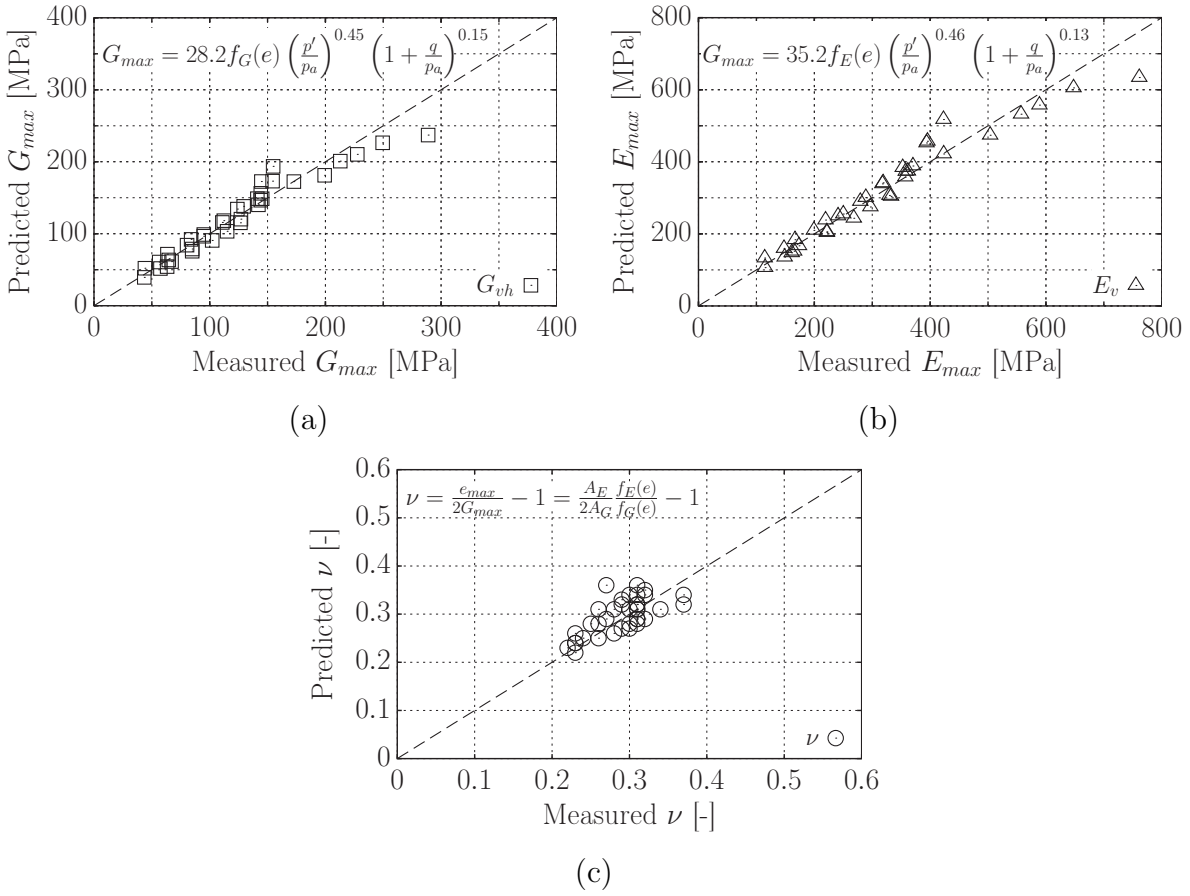

Figure 5.13: Comparison between the measured and predicted values for: (a) Shear modulus, $G_{\max}$, (b) Young's modulus, $E_{\max}$, (c) Poisson's ratio, ν.

6 Conclusions and outlook

6.1 Conclusions

Elastic characteristics of soils are a fundamental component of constitutive models, emphasizing its importance in soil mechanics and deformation analyses. At low strain amplitudes ($< 0.001\%$), no energy is lost during loading and unloading, and stiffness takes its maximum value, known as small-strain stiffness. Small-strain stiffness evolves with changes in density, stress state, loading history, soil fabric, and particle characteristics. Experimental studies have highlighted the critical role of grain shape (characterized by form, roundness, and roughness) and particle size distribution in determining the small-strain stiffness of granular soils.

To investigate these relationships in greater depth, this thesis detailed the development of advanced experimental techniques and presented findings on the small-strain characteristics of granular materials. Specifically, it described the incorporation of piezoelectric elements into a triaxial device, as well as the experimental results obtained. The piezoelectric elements - bender elements for shear waves and compression elements for compression waves - were installed in both vertical and lateral directions within the triaxial device. The successful modification and application of the device are described, and its validation is detailed. Approximately 40 specimens were tested using the modified triaxial device to investigate the impact of key variables, including sample preparation technique, stress state, particle shape, and grain size distribution, as well as their mutual interaction, on the elastic stiffness of clean granular materials. The main findings of this study are summarized in the following.

6.1.1 Instrumentation of triaxial device

Small-strain stiffness is best measured with techniques that minimize disturbance to the soil's structure, preserving its intrinsic fabric. While traditional static methods using high-resolution displacement sensors provide accurate results, they are often labor-intensive

and require sophisticated equipment. In contrast, laboratory geophysics methods, which rely on the propagation speed of low-amplitude elastic waves, have emerged as efficient alternatives. Using piezoelectric elements embedded in testing apparatuses, these methods allow for precise, non-destructive, and repeatable stiffness measurements, eliminating the need for complex setups. The wave propagation technique, using piezoelectric elements, was adopted in this study to evaluate the stiffness of the tested granular soils at the small-strain level. Pairs of bender/compression elements were designed and manufactured to be installed in the top and bottom caps. The elements were employed to measure wave velocities along direct vertical wave paths between opposite faces of the sample (v_{vh} and v_p), which were used to calculate shear modulus G_{vh} and Young's modulus E_v.

Furthermore, two additional pairs of bender elements were installed on the lateral sides of the sample, directly on the membrane. These lateral elements were specifically designed to ensure that the boundary conditions of the sample closely resemble those of a standard triaxial device, while avoiding any added rigidity to the sides of the sample. This design allows for lateral wave velocity measurements during standard triaxial tests and facilitates the monitoring of fabric changes in the sample throughout triaxial testing under drained or undrained conditions. The lateral elements were used to measure v_{hv} and v_{hh}, which were then used to calculate shear moduli G_{hv} and G_{hh}.

Additionally, in some experiments, wave velocities were measured along inclined paths between bender elements ($v_{s\theta}$) on adjacent faces to deduce the full set of anisotropic elastic parameters. In principle, this implies some redundancy in the measurements, but this was reduced by the undesired compression/shear wave interaction.

The elements were connected with waterproof cables to an electric measuring system that comprises of a computer with the software LabVIEW, two amplifiers, and a data logger. A time domain procedure was used for the interpretation of the received signals in order to estimate arrival times and hence the corresponding wave velocities. The traveling time was measured using the first deflection method, as adopted in previous studies.

A series of trial tests were conducted to determine the appropriate waveform, frequency, and amplitude required to obtain high-quality signals using the designed elements. The delay time between the elements was determined by keeping the sender and receiver in direct contact, and this delay was subtracted from the measured traveling time. The results also showed that a sinusoidal waveform could be adopted for all tests. For the initial calibration of the system, aluminum and plastic samples were used. From the experiments, the stiffness of aluminum and plastic was determined and validated against known material properties. These experiments confirmed the performance and accuracy

of the developed elements. Additionally, experiments were conducted on Hostun sand to compare the results obtained from the newly designed device with those from previous studies. Earlier research on Hostun sand included tests using a resonant column device for isotropic and anisotropic loading at Ruhr Universität Bochum, as well as wave velocity measurements in various directions using a true triaxial device equipped with bender elements in experiments conducted at Bristol University.

All these comparisons validated the performance and reliability of the newly developed device.

6.1.2 Effect of sample preparation method

About 13 triaxial tests were conducted to evaluate the effect of the sample preparation method on the inherent anisotropy of the clean Hostun sand. The specimens were prepared using the Air Pluviation (AP) and Moist Tamping (MT) methods, incorporating different initial water contents (5, 10 and 15%). The shear modulus was measured using the bender element technique after consolidation under isotropic stress states and at an axial strain of 24% during shearing in a drained triaxial compression test. The comparison of results from specimens prepared using these different methods revealed notable insights into the effect of sample preparation at both small and large strain levels:

- At small strain level

  As evident from the experimental results, the method of sample preparation significantly influences the initial fabric of the specimens. The analysis showed that the deviation in normalized shear wave velocity ($v_{s_{ij}}/v_{s_{vh}}$) in samples prepared using the MT method is greater than that in samples prepared using the AP method. This indicates that the inherent anisotropy in samples prepared using the AP method is lower than that in samples prepared using the MT method.

  The measured maximum shear modulus (G_{vh}) in specimens prepared using the AP and MT methods revealed notable differences. Loose specimens prepared using the AP method exhibited a higher maximum shear modulus compared to those prepared using the MT method, possibly due to the presence of macropores in loose specimens prepared by the MT method. In contrast, dense specimens prepared using the AP method showed a lower maximum shear modulus than those compacted using the MT method. This behavior is attributed to the energy applied during sample preparation and the resulting contact conditions between particles. However, the

effect of sample preparation on the maximum shear modulus G_{vh} was found to be less significant compared to the influence of void ratio and effective confining stress.

- At large strain level

  For axial strains of around 24%, the measured shear wave velocities were found to depend on the mean effective stress, p', regardless of the sample preparation method and the void ratio. The triaxial test results also confirmed that the effect of sample preparation on the critical state line (CSL) is negligible, and a unique curve can be defined as the CSL, independent of the sample preparation method.

6.1.3 Effect of anisotropic stress states

Experiments were also conducted using the modified device to evaluate the effect of stress state under drained and undrained conditions on the shear wave velocities ($v_{s_{ij}}$) and maximum shear stiffness (G_{ij}) in various directions. The wave velocity measurements were conducted during conventional compression triaxial tests on Hostun sand prepared using the AP method.

The results revealed a stiffness isotropy under isotropic stress states so that G_{vh}, G_{hv} and G_{hh} are almost equal in magnitude. For the specimens subjected to stress anisotropy, it was found that $G_{vh} \neq G_{hv} \neq G_{hh}$ and also the increase of stress ratio leads to an increase of stiffness anisotropy. Thus, for the investigation of the behavior of granular materials subjected to stress anisotropy, quantification of the stiffness in one direction (e.g., G_{vh} as commonly obtained in laboratory tests) is not enough to provide complete data for constitutive modeling.

However, some features of the observed response were inconsistent with the theory of cross-anisotropic elasticity: The shear waves v_{vh} and v_{hv} did not always have the same velocities, and thus $G_{vh} \neq G_{hv}$. The same was also observed in some previous studies referenced in the thesis, which give hints that the differences reduce with decreasing particle size. Assuming strain rate independence (and calculating G_{vh} from the average of the v_{vh} and v_{hv} velocities) made it possible to determine full sets of cross-anisotropic elastic constants by combining high-resolution triaxial and multidirectional bender element tests.

The experimental results indicated that in loose specimens under undrained conditions, $G_{\max}$ decreases until the phase transformation point is reached and then increases along the dilation path. In contrast, under drained conditions, $G_{\max}$ continuously increases with increasing mean effective stress.

To investigate the effect of the stress anisotropy on the cross anisotropy of the elastic stiffness of the specimens, wave velocities were measured in the horizontal, vertical, and inclined directions for a polar representation of wave velocity across the cross-section of the sample. The polar representation of wave velocities (and consequently the shear modulus) under anisotropic stress states in specimens under drained and undrained conditions revealed distinct behaviors. Under undrained conditions, the wave velocities in all directions ($v_{s\theta}$) were approximately equal and increased slightly with increasing vertical stress until $\sigma'_1/\sigma'_3 = 3$. However, under drained conditions, the wave velocities in the vertical direction were larger than those in the horizontal direction. For a loose specimen ($e = 0.9$) under a stress ratio of $\sigma'_1/\sigma'_3 = 3$, the ratio v_{vh}/v_{hv} was found to be approximately 1.3. The polar representation of wave velocities across the sample cross-section forms a vertical ellipse, demonstrating that v_{vh} is greater than v_{hv}. Additionally, under anisotropic drained compression, the degree of anisotropy depends on the adopted stress ratio. The ratios G_{vh}/G_{hh} increase with an increase of the compression stress ratio, which is due to the increase in the normal contact forces in the direction of larger stress (σ'_1). By a further increase of the vertical stress, σ'_1, G_{vh} in loose specimens increases due to the compaction of the sample, while it decreases in dense samples due to dilation. However, the results revealed that the shear wave velocities of initially dense and loose specimens are almost equal at the critical state.

6.1.4 Combined effect of grain shape and grading

Three materials with significantly different grain shapes - angular crushed glass (regularity = 0.4), sub-angular Rhine sand (regularity = 0.6), and round glass beads (regularity = 0.9) - were used for this study. They were mixed with two different grain size distribution curves, having the same mean grain size but different uniformity coefficients of $C_u = 1.25$ and 5. Grain shape parameters were quantified using images of individual grains captured by a high-resolution microscope and analysed through various image-processing techniques. Air-pluviated triaxial samples with varying densities were tested under isotropic stress states at different mean effective stresses, as well as under anisotropic stress states with different deviatoric stresses.

Using the piezoelectric elements, shear and compression wave velocities were measured across different orientations. Based on the experimental data, the combined influence of grain shape and grading on $G_{\max}$, $E_{\max}$, and Poisson's ratio (ν) was analyzed. The results showed that for all tested grain shapes and gradations stiffness measured along different directions increases with increasing p' and decreasing void ratio e.

For all tested materials, the magnitude of G_{hh} is the least while the G_{vh} is the largest; G_{hv} lies in between. An increase in stress anisotropy results in higher normal contact forces, which lead to a larger G_{vh} compared to G_{hv}. However, the shear forces are relatively much smaller than the normal forces, which explains why G_{hh} is the smallest. The results also showed a decrease in G_{hh} with increasing vertical stress (σ_1') during the anisotropic loading phase, which can be due to the buckling of force chains as vertical stress increases, from a micromechanical perspective.

Furthermore, maximum G_{ij} and $E_{\max}$ are generally larger for the uniformly graded materials ($C_u = 1.25$) compared to the well-graded materials ($C_u = 5$).

The results for anisotropic stress states showed that in sand with medium density (D_r=45%) under anisotropic loading, the stiffness of samples with rounded particles is higher than that of samples with angular particles. The results also revealed that Poisson's ratio increases slightly with increasing void ratio, while the effect of mean effective stress and particle shape on Poisson's ratio is negligible.

Empirical equations were also developed in the space of q, p', and e to estimate $G_{\max}$, $E_{\max}$, and Poisson's ratio. The constant parameters of the developed equations were correlated to particle shape descriptors. The regression analysis further revealed that the exponent describing the dependence on p' in the equations is larger than the exponent for the dependence on the deviatoric stress ratio q/p', confirming the dominant effect of mean effective stress on maximum moduli compared to shear stress.

6.2 Future research

This section outlines future research to deepen the understanding of the effects of various parameters on the small-strain stiffness of geomaterials.

- Inter-particle friction

  Shear wave velocity v_s depends on the inter-particle coefficient of friction, which is an intrinsic particle characteristic. Friction has been proposed as the primary mechanism through which shear waves transmit between particles. This hypothesis could be tested by examining specimens composed of spherical particles with identical size and mineral composition, but varying inter-particle friction coefficient via variations in surface roughness.

- Effect of fluid viscosity on maximum moduli

The viscosity of the fluid within the pore space may influence the small-strain stiffness and wave propagation characteristics. Future studies could investigate the extent to which fluid viscosity impacts G_{ij}, $E_{\max}$, in partially saturated or fully saturated samples.

- Temperature effects on maximum moduli

  Temperature variations could have a combined effect on the mechanical behavior of geomaterials and particle interactions. While the experiments in this study were conducted under a constant laboratory temperature (approximately 21°C), future research could evaluate how different temperatures influence maximum moduli and their interaction with particle characteristics such as shape, roughness, and inter-particle friction.

- Particle shape and contact mechanics

  Advanced imaging and computational techniques (e.g., X-ray CT scanning and discrete element modeling) could be used to investigate the role of complex particle shapes on contact mechanics and their contribution to small-strain stiffness. Exploring non-spherical particles with varying aspect ratios and angularities could further enhance understanding.

- Influence of fines content

  The presence of fines significantly alters the behavior of granular materials by filling voids and modifying particle contacts. Future studies could explore how varying fines content influences G_{ij}, $E_{\max}$, and Poisson's ratio under isotropic, anisotropic, and cyclic loading conditions.

- Freezing and thawing effects

  Cycles of freezing and thawing can modify the microstructure of geomaterials, including changes in particle contacts, pore distribution, and stiffness. Investigating the effects of freezing and thawing on small-strain stiffness, particularly for soils with varying fines content, could provide insights into the performance of geomaterials in cold regions.

By addressing these topics, future research can provide a more comprehensive understanding of the interplay between particle characteristics, environmental conditions, and the small-strain response of geomaterials, contributing to improved predictive models for geotechnical applications.

Bibliography

Abdoun, T. & Dobry, R. (2002), 'Evaluation of pile foundation response to lateral spreading', *Soil Dynamics and Earthquake Engineering* **22**(9), 1051–1058.

Altuhafi, F. N., Coop, M. R. & Georgiannou, V. N. (2016), 'Effect of particle shape on the mechanical behavior of natural sands', *Journal of Geotechnical and Geoenvironmental Engineering* **142**(12), 04016071.

Andersen, K. (2009), 'Bearing capacity under cyclic loading - offshore, along the coast, and on land. The 21st Bjerrum Lecture presented in Oslo, 23 November 2007', *Canadian Geotechnical Journal* **46**(5), 513–535.

Aris, M., Benahmed, N. & Bonelli, S. (2012), 'Experimental geomechanics: a laboratory study on the behaviour of granular material using bender elements', *European Journal of Environmental and Civil Engineering* **16**(1), 97–110.

Athanasopoulos, G. A. & Richart, F. E. (1983), 'Correlation between G_0 and τ_{max} for kaolinite clay', *Journal of Geotechnical Engineering* **109**(5), 719–723.

Atkinson, J. H. (2000), 'Non-linear soil stiffness in routine design', *Géotechnique* **50**(5), 487–508.

Azeiteiro, R. J. N., Coelho, P. A. L. F., Taborda, D. M. G. & Grazina, J. C. D. (2017), 'Critical state-based interpretation of the monotonic behavior of Hostun sand', *Journal of Geotechnical and Geoenvironmental Engineering* **143**(5), 1–14.

Been, K. & Jefferies, M. (1985), 'A state parameter for sands', *Géotechnique* **35**, 99–112.

Bellotti, R., Jamiolkowski, M., Lo Presti, D. C. F. & O'Neill, D. A. (1996), 'Anisotropy of small strain stiffness in Ticino sand', *Géotechnique* **46**(1), 115–131.

Benahmed, N. (2001), Mechanical behaviour of a sand under monotonic and cyclic loading: application to liquefaction and cyclic mobility phenomena (in French), PhD thesis.

Biot, M. A. (1956*a*), 'Theory of propagation of elastic waves in a fluid-saturated porous solid. I. Low-frequency range', *The Journal of the Acoustical Society of America* **28**(2), 168–178.

Biot, M. A. (1956*b*), 'Theory of propagation of elastic waves in a fluid-saturated porous solid. II. Higher frequency range', *The Journal of the Acoustical Society of America* **28**(2), 179–191.

Biot, M. A. (1962), 'Mechanics of deformation and acoustic propagation in porous media', *Journal of Applied Physics* **33**(4), 1482–1498.

Bowden, F. P. & Tabor, D. (1964), *The friction and lubrication of solids*, Clarendon Press.

Brandt, H. (1955), 'A study of the speed of sound in porous granular media', *Journal of Applied Mechanics* **22**(4), 479–486.

Bui, M. (2009), Influence of some particle characteristics on the small strain response of granular materials, PhD thesis, University of Southampton.

Cascante, G. & Santamarina, J. C. (1996), 'Interparticle contact behavior and wave propagation', *Journal of Geotechnical Engineering* **122**(10), 831–839.

Cho, G.-C., Dodds, J. & Santamarina, J. C. (2006), 'Particle shape effects on packing density, stiffness, and strength: natural and crushed sands', *Journal of Geotechnical and Geoenvironmental Engineering* **132**(5), 591–602.

Desrues, J. & Mokni, M. (2007), 'Drained and undrained biaxial test dataon Hostun RF sand'.

Doanh, T., Ibraim, E. & Matiotti, R. (1997), 'Undrained instability of very loose Hostun sand in triaxial compression and extension. Part 1: experimental observations', *Mechanics of Cohesive-Frictional Materials* **2**(1), 47–70.

Drnevich, V. P. (1978), *Resonant-column testing - problems and solutions*, ASTM, pp. 384–398.

Duffy, J. (1959), 'A differential stress-strain relation for the hexagonal close-packed array of elastic spheres', *Journal of Applied Mechanics* **26**(1), 88–94.

Duffy, J. & Mindlin, R. D. (1957), 'Stress-strain relations and vibrations of a granular medium', *Journal of Applied Mechanics* **24**(4), 585–593.

Dyvik, R. & Madshus, C. (1985), 'Lab measurements of G_{max} using bender elements', *Proceedings of the ASCE Annual Convention on Advances in the Art of Testing Soils under Cyclic Conditions* pp. 186–196.

Ezaoui, A. & Di Benedetto, H. (2009), 'Experimental measurements of the global anisotropic elastic behaviour of dry Hostun sand during triaxial tests, and effect of sample preparation', *Géotechnique* **59**(7), 621–635.

Ferreira, T. & Rasband, W. (2012), *ImageJ User Guide*, IJ 1.46r edn.

Field, W. (1963), Towards the statistical definition of a granular mass, *in* 'Proceeding of the 4th Australia - New Zealand conference on Soil Mechanics', pp. 143–148.

Fioravante, V. (2000), 'Anisotropy of small strain stiffness of Ticino and Kenya sands from seismic wave propagation measured in triaxial testing', *Soils and Foundations* **40**(4), 129–142.

Flavigny, É., Desrues, J. & Palayer, B. (1990), Note technique - le sable d'Hostun RF, *in* 'Revue Française de Géotechnique'.

Frossard, E. (1979), 'Effect of sand grain shape on interparticle friction; indirect measurements by Rowe's stress dilatancy theory', *Géotechnique* **29**(3), 341–350.

Gajo, A., Fedel, A. & Mongiovi, L. (1997), 'Experimental analysis of the effects of fluid-solid coupling on the velocity of elastic waves in saturated porous media', *Géotechnique* **47**(5), 993–1008.

Gassmann, F. (1951), 'Elastic waves throuogh a packing of spheres', *Geophysics* **16**(4), 673–685.

Ghionna, V. & Porcino, D. (2006), 'Liquefaction resistance of undisturbed and reconstituted samples of a natural coarse sand from undrained cyclic triaxial tests', *Journal of Geotechnical and Geoenvironmental Engineering* **132**(2), 194–201.

Goudarzy, M. (2015), 'Micro and macro mechanical assessment of small and intermediate strain properties of granular materials', PhD thesis, Publications of the Chair of Foundation Engineering, Soil and Rock Mechanics, Ruhr-University Bochum, Issue No. 56.

Goudarzy, M., König, D. & Schanz, T. (2018), 'Small and intermediate strain properties of sands containing fines', *Soil Dynamics and Earthquake Engineering* **110**, 110–120.

Goudarzy, M., König, D. & Schanz, T. (2016a), 'Small strain stiffness of granular materials containing fines', *Soils and Foundations* **56**(5), 756–764.

Goudarzy, M., Magnanimo, V., König, D. & Schanz, T. (2020), 'Anisotropic stress state and small strain stiffness in granular materials: RC experiments and DEM simulations', *Meccanica* **55**, 1869–1883.

Goudarzy, M., Rahemi, N.and Rahman, M. & Schanz, T. (2017), 'Predicting the maximum shear modulus of sands containing nonplastic fines', *Journal of Geotechnical and Geoenvironmental Engineering* **143**(9).

Goudarzy, M., Rahman, M. M., König, D. & Schanz, T. (2016b), 'Influence of non-plastic fines content on maximum shear modulus of granular materials', *Soils and Foundations* **56**(6), 973–983.

Goudarzy, M. & Wichtmann, T. (2019), Influence of particle characteristics on the dynamic characteristics of granular materials, *in* 'Fachsektionstage Geotechnik, Würzburg, Germany'.

Graton, L. C. & Fraser, H. J. (1935), 'Systematic packing of spheres: with particular relation to porosity and permeability', *The Journal of Geology* **43**(8, Part 1), 785–909.

Gray, W. (1968), *The packing of solid particles*, Champman and Hall Ltd.

Gu, X., Yang, J., Huang, M. & Gao, G. (2015), 'Bender element tests in dry and saturated sand: Signal interpretation and result comparison', *Soils and Foundations* **55**(5), 951–962.

Guo, Y. & Yang, J. (2017), Use of shear wave velocity to evaluate in-situ state of silty sands, *in* 'Proceedings of the 19th International conference on Soil Mechanics and Geotechnical Engineering', pp. 603–606.

Hardin, B. O. & Black, W. L. (1966), 'Sand stiffness under various triaxial stresses', *Journal of the Soil Mechanics and Foundations Division* **92**(2), 27–42.

Hardin, B. O. & Black, W. L. (1968), 'Vibration modulus of normally consolidated clay', *Journal of the Soils Mechanics and Foundation Division* **94**(SM2), 353–369.

Hardin, B. O. & Blandford, G. E. (1989), 'Elasticity of particulate materials', *JJournal of Geotechnical Engineering* **115**(6), 788–805.

Hardin, B. O. & Kalinski, M. E. (2005), 'Estimating the shear modulus of gravelly soils', *Journal of Geotechnical and Geoenvironmental Engineering* **131**(7), 867–875.

Hardin, B. O. & Richart, F. E. (1963), 'Elastic wave velocities in granular soils', *Journal of the Soil Mechanics and Foundations Division* **89**(SM1), 33–65.

Hoque, E. & Tatsuoka, F. (2004), 'Effects of stress ratio on small-strain stiffness during triaxial shearing', *Géotechnique* **54**(7), 429–506.

Horn, H. M. & Deere, D. U. (1962), 'Frictional characteristics of minerals', *Géotechnique* **12**(4), 319–335.

Hryciw, R. D., Zheng, J. & Shetler, K. (2016), 'Particle roundness and sphericity from images of assemblies by chart estimates and computer methods', *Journal of Geotechnical and Geoenvironmental Engineering* **142**(9).

Ishibashi, I. & Agarwal, T. K. (1991), Multi-directional wave velocity by piezoelectric crystals, *in* S. K. Bhatia & G. W. Blaney, eds, 'Proceeding of Recent Advances in Instrumentation Data Acquisition and Testing in Soil Dynamics, ASCE', American Society of Civil Engineers, New York, pp. 102–117.

Iwasaki, T. & Tatsuoka, F. (1977), 'Effects of grain size and grading on dynamic shear moduli of sands', *Soils and Foundations* **17**(3), 19–35.

Jamiolkowski, M., Lancellotta, R. & Lo Presti, D. (1995), Remarks on the stiffness at small strains of six Italian clays, *in* S. Satoru, M. Toshiyuki & M. Seichi, eds, 'Pre-failure deformation of geomaterials: Proceedings of the First International Conference on Pre-failure Deformation Characteristics of Geomaterials, Sapporo, Japan', Rotterdam: Balkema, pp. 817–836.

Jamiolkowski, M., Leroueil, S. & LoPresti, D. C. F. (1991), Design parameters from theory to practice, *in* 'Proc. Geo-Coast '91', Yokohama, Japan, pp. 1–41.

Johnson, K. L. (1985), *Contact Mechanics*, Cambridge University Press.

Juneja, A. & Raghunandan, M. (2010), Effect of sample preparation on strength of sands, *in* 'Proceeding of the Indian Geotechnical Conference'.

Koerner, R. M. (1970), 'Effect of particle characteristics on soil strength', *Journal of the Soil Mechanics and Foundations Division* **96**(4), 1221–1234.

Kokusho, T., Yoshida, Y. & Esashi, Y. (1982), 'Dynamic properties of soft clay for wide strain range', *Soils and Foundations* **22**(4), 1–18.

Konrad, J. M. (1993), 'Undrained response of loosely compacted sands during monotonic and cyclic compression tests', *Géotechnique* **43**(1), 69–89.

Krumbein, J. M. & Sloss, L. L. (1963), *Stratigraphy and sedimentation*, Freeman and Company, San Francisco.

Kuerbis, R. & Vaid, Y. (1988), 'Sand sample preperation - the slurry deposition method', *Soils and Foundations* **28**(4), 107–118.

Kumara, J., Hayano, K. & Ogiwara, K. (2012), 'Image analysis techniques on evaluation of particle size distribution of gravel', *International Journal of GEOMATE* **3**(1), 290–297.

Kuwano, R. (1999), The stiffness and yielding anisotropy of sand, PhD thesis, University of Texas, Austin.

Lee, J.-S. & Santamarina, J. C. (2005), 'Bender elements: performance and signal interpretation', *Journal of Geotechnical and Geoenvironmental Engineering* **131**(9), 1063–1070.

Lee, K. M. & Rowe, R. K. (1989), 'Deformations caused by surface loading and tunnelling: the role of elastic anisotropy', *Géotechnique* **39**(1), 125–140.

Leong, E., Yeo, S. & Rahardjo, H. (2005), 'Measuring shear wave velocity using bender elements', *Geotechnical Testing Journal* **28**(5), 488–498.

Li, X. S. & Wang, Y. (1998), 'Linear representation of steady-state line for sand', *Journal of Geotechnical and Geoenvironmental Engineering* **124**(12), 1215–1217.

Liao, C. L., Chan, T. C., Suiker, A. S. J. & Chang, C. S. (2000), 'Pressure-dependent elastic moduli of granular assemblies', *International Journal for Numerical and Analytical Methods in Geomechanics* **24**(3), 265–279.

Liu, X. & Yang, J. (2018), 'Shear wave velocity in sand: effect of grain shape', *Géotechnique* **68**(8), 742–748.

Liu, X., Zou, D., Liu, J., Zhou, C. & Zheng, B. (2020), 'Experimental study to evaluate the effect of particle size on the small strain shear modulus of coarse-grained soils', *Measurement* **163**, 107954.

Lo Presti, D. C. F. & O'Neill, D. A. (1991), Laboratory investigation of small strain modulus anisotropy in sand, *in* A.-B. Huang, ed., 'Calibration Chamber Testing', Elsevier Science Publishing, pp. 213–224.

Lo Presti, D., Pedroni, S., Cavallaro, A., Jamiolkowski, M. & Pallara, O. (1997), 'Shear modulus and damping of soils', *Géotechnique* **47**(3), 603–617.

Love, A. E. H. (1944), *A treatise on the mathematical theory of elasticity*, Dover Books on Engineering Series, Dover Publications, New York.

Magnanimo, V., Ragione, L. L., Jenkins, J. T., Wang, P. & Makse, H. A. (2008), 'Characterizing the shear and bulk moduli of an idealized granular material', *EPL (Europhysics Letters)* **81**(3), 34006.

Marcuson, W. & Wahls, H. (1972), 'Time effects on dynamic shear modulus of clays', *Journal of the Soil Mechanics and Foundations Division* **98**(12), 1359–1373.

Menq, F. M. & Stokoe, K. H. (2003), Linear dynamic properties of sandy and gravelly soils from large-scale resonant tests, *in* H. Di Benedetto, H. Geoffroy, T. Doanh & C. Sauzèat, eds, 'Deformation Characteristics of Geomaterials', pp. 63–71.

Mindlin, R. D. & Deresiewicz, H. (1953), 'Elastic spheres in contact under varying oblique forces', *Journal of Applied Mechanics* **20**(3), 327–344.

Mitchell, J. K. & Soga, K. (2005), *Fundamentals of soil behavior*, John Wiley & Sons.

Miura, S. & Toki, S. (1982), 'A sample preparation method and its effect on static and cyclic deformation-strength properties of sand', *Soils and Foundations* **22**(1), 61–77.

Mulilis, J. P., Seed, H. B., Chan, C., Mitchell, J. & Arulanandan, K. (1977), 'Effects of sample preparation on sand liquefaction', *Journal of the Geotechnical Engineering Division, ASCE* **103**(2), 91–108.

Ng, C. W. W., Xu, J. & Yung, S. Y. (2009), 'Effects of wetting-drying and stress ratio on anisotropic stiffness of an unsaturated soil at very small strains', *Canadian Geotechnical Journal* **46**, 1062–1076.

Ng, T.-T. & Petrakis, E. (1996), 'Small-strain response of random arrays of spheres using discrete element method', *Journal of Engineering Mechanics* **122**(3), 239–244.

Oda, M. (1972), 'Initial fabrics and their relations to mechanical properties of granular materials', *Soils and Foundations* **12**(1), 17–36.

Oda, M. (1977), 'Co-ordination number and its relation to shear strength of granular material', *Soils and Foundations* **37**(3), 29–42.

Payan, M., Khoshghalb, A., Senetakis, K. & Khalili, N. (2016a), 'Small-strain stiffness of sand subjected to stress anisotropy', *Soil Dynamics and Earthquake Engineering* **88**, 143–151.

Payan, M., Senetakis, K., Khoshghalb, A. & Khalili, N. (2016b), 'Effect of gradation and particle shape on small-strain Young's modulus and Poisson's ratio of sands', *International Journal of Geomechanics* pp. 1–14.

Pennington, D. S., Nash, D. F. T. & Lings, M. L. (1997), 'Anisotropy of G_0 shear stiffness in Gault Clay', *Géotechnique* **47**(3), 391–398.

Pennington, D. S., Nash, D. & Lings, M. L. (2001), 'Horizontally mounted bender elements for measuring anisotropic shear moduli in triaxial clay specimens', *Geotechnical Testing Journal* **24**(2), 133–144.

Petrakis, E. & Dobry, R. (1987), Micromechanical modeling of granular soil at small strain by arrays of elastic spheres, Technical report, Departmentof civil engineering Rensselaer Polytechnic Institute.

Petrakis, E., Dobry, R. & Ng, T. T. (1988), Small strain response of random arrays of elasticspheres using a nonlinear distinct element procedure, Technical report, Department of Civil Engineering, Rensselaer Polytechnic Institute.

Pincus, H. J., Lo Presti, D., Pallara, O., Lancellotta, R., Armandi, M. & Maniscalco, R. (1993), 'Monotonic and cyclic loading behavior of two sands at small strains', *Geotechnical Testing Journal* **16**(4), 409–424.

Powers, M. C. (1953), 'A new roundness scale for sedimentary particles', *Journal of Sedimentary Petrology* **23**(2), 117–119.

Procter, D. C. & Barton, R. R. (1974), 'Measurements of the angle of interparticle friction', *Géotechnique* **24**(4), 581–604.

Qiu, T. & Fox, P. J. (2008), 'Effective soil density for propagation of small strain shear waves in saturated soil', *Journal of Geotechnical and Geoenvironmental Engineering* **134**(12), 1815–1819.

Radjai, F. (1999), 'Multicontact dynamics of granular systems', *Computer Physics Communications* **121-122**, 294–298. Proceedings of the Europhysics Conference on Computational Physics CCP 1998.

Randolph, M., Dolwin, J. & Beck, R. (1994), 'Design of driven piles in sand', *Géotechnique* **44**(3), 427–448.

Roesler, S. K. (1979), 'Anisotropic shear modulus due to stress anisotropy', *Journal of the Geotechnical Engineering Division* **105**(7), 871–880.

Roscoe, K. H., Schofield, A. N. & Wroth, C. P. (1958), 'On the yielding of soils', *Géotechnique* **8**(1), 22–53.

Rothenburg, L. & Bathurst, R. J. (1989), 'Analytical study of induced anisotropy in idealized granular materials', *Géotechnique* **39**(4), 601–614.

Sadek, T., Lings, M., Dihoru, L. & Wood, D. M. (2007), 'Wave transmission in Hostun sand: multiaxial experiments', *Rivista Italiana Geotechnica* **41**(2), 69–84.

Sahaphol, T. & Miura, S. (2005), 'Shear moduli of volcanic soils', *Soil Dynamics and Earthquake Engineering* **25**, 157–165.

Salgado, R., Bandini, P. & Karim, A. (2000), 'Shear strength and stiffness of silty sand', *Journal of Geotechnical and Geoenvironmental Engineering* **126**(5), 451–462.

Santamarina, J. C. & Cascante, G. (1996), 'Stress anisotropy and wave propagation: A micromechanical view', *Canadian Geotechnical Journal* **33**, 770–782.

Sarkar, D. (2022), 'Influence of particle characteristics on the behaviour of granular materials under static, cyclic and dynamic loading', PhD thesis, Publications of the Chair of Soil Mechanics, Foundation Engineering and Environmental Geotechnics, Ruhr-University Bochum, Issue No. 75.

Sarkar, D., Goudarzy, M., König, D. & Wichtmann, T. (2020), 'Influence of particle shape and size on the threshold fines content and the limit index void ratios of sands containing non-plastic fines', *Soils and Foundations* **60**(3), 621–633.

Sarkar, D., Goudarzy, M. & Wichtmann, T. (2022), 'Inspection of various grain morphology parameters based on wave velocity measurements on three different granular materials', *Soil Dynamics and Earthquake Engineering* **153**(107071).

Sarkar, D., Goudarzy, M. & Wichtmann, T. (2024), 'Influence of particle size on the small-strain stiffness in granular soils: Experimental observations and micromechanical interpretation', *Géotechnique* **74**(9), 920–934.

Schanz, T. & Vermeer, P. A. (1996), 'Angles of friction and dilatancy of sand', *Géotechnique* **46**(1), 145–151.

Sen, P. N., Scala, C. & Cohen, M. H. (1981), 'A self-similar model for sedimentary rocks with application to the dielectric constant of fused glass beads', *Geophysics* **46**(5), 781–795.

Senetakis, K., Anastasiadis, A. & Pitilakis, K. (2012), 'The small-strain shear modulus and damping ratio of quartz and volcanic sands', *Geotechnical Testing Journal* **35**.

Shi, J., Haegeman, W. & Cnudde, V. (2021), 'Anisotropic small-strain stiffness of calcareous sand affected by sample preparation, particle characteristic and gradation', *Géotechnique* **71**(4), 305–319.

Shibuya, S., Hwang, S. C. & Mitachi, T. (1997), 'Elastic shear modulus of soft clays from shear wave velocity measurement', *Géotechnique* **47**(3), 593–601.

Shibuya, S. & Tanaka, H. (1996), 'Estimate of elastic shear modulus in holocene soil deposits', *Soils and Foundations* **36**(4), 45–55.

Shirley, D. J. & Hampton, L. D. (1978), 'Shear-wave measurement in laboratory sediments', *Journal of the Acoustical Society of America* **63**(2), 607–613.

Skinner, A. E. (1969), 'A note on the influence of interparticle friction on the shearing strength of a random assembly of spherical particles', *Géotechnique* **19**(1), 150–157.

Smith, W. O., Foote, P. D. & Busang, P. F. (1929), 'Packing of homogeneous spheres', *Phys. Rev.* **34**(9), 1271–1274.

Stark, T. D. & Eid, H. T. (1998), 'Performance of three-dimensional slope stability methods in practice', *Journal of the Soil Mechanics and Foundation Division, ASCE* **124**(11), 1049–1060.

Stokoe, K. H., Lee, J. N.-K. & Lee, S. H.-H. (1991), Characterization of soil in calibration chambers with seismic waves, *in* A.-B. Huang, ed., 'Calibration Chamber Testing', Elsevier Science Publishing, pp. 363–376.

Stoll, R. D. & Bryan, G. M. (1970), 'Wave attenuation in saturated sediments', *The Journal of the Acoustical Society of America* **47**(5B), 1440–1447.

Sze, H. Y. & Yang, J. (2014), 'Failure modes of sand in undrained cyclic loading: impact of sample preparation', *Journal of Geotechnical and Geoenvironmental Engineering* **140**(1), 152–169.

Tatsuoka, F., Iwasaki, T., Yoshida, S., Fukushima, S. & Sudo, H. (1979), 'Shear modulus and damping by drained tests on clean sand specimens reconstituted by various methods', *Soils and Foundations* **19**(1), 39–54.

Tatsuoka, F., Ochi, K., Fujii, S. & Okamoto, M. (1986), 'Cyclic undrained triaxial and torsional shear strength of sands for different sample preparation methods', *Soils and Foundations* **26**(3), 23–41.

Terzaghi, K., Peck, R. & Mesri, G. (1996), *Soil Mechanics in Engineering Practice (3rd edition)*, New York; Wiley.

Verdugo, R. & Ishihara, K. (1996), 'The steady state of sandy soils', *Soils and Foundations* **32**(2), 81–91.

Wadell, H. (1932), 'Volume, shape and roundness of rock particles', *The Journal of Geology* **40**(5), 443–451.

Walton, K. (1987), 'The effective elastic moduli of a random packing of spheres', *Journal of the Mechanics and Physics of Solids* **35**(2), 213–226.

Wang, Y. H. & Mok, C. M. B. (2008), 'Mechanisms of small-strain shear-modulus anisotropy in soils', *Journal of Geotechnical and Geoenvironmental Engineering* **134**(10), 1516–1530.

Wichtmann, T. (2016), 'Soil behaviour under cyclic loading - experimental observations, constitutive description and applications', Habilitation thesis, Publications of the Institute of Soil Mechanics and Rock Mechanics, Karlsruhe Institute of Technology, Issue No. 181.

Wichtmann, T., Navarrete Hernández, M. & Triantafyllidis, T. (2015), 'On the influence of a non-cohesive content of fines on the small strain stiffness of quartz sand', *Soil Dynamics and Earthquake Engineering* **69**(2), 103–114.

Wichtmann, T. & Triantafyllidis, T. (2004*a*), 'Influence of a cyclic and dynamic loading history on dynamic properties of dry sand, part I: Cyclic and dynamic torsional prestraining', *Soil Dynamics and Earthquake Engineering* **24**(2), 127–147.

Wichtmann, T. & Triantafyllidis, T. (2004*b*), 'Influence of a cyclic and dynamic loading history on dynamic properties of dry sand, part II: cyclic axial preloading', *Soil Dynamics and Earthquake Engineering* **24**(11), 789–803.

Wichtmann, T. & Triantafyllidis, T. (2009), 'Influence of the grain-size distribution curve of quartz sand on the small strain shear modulus G_{max}', *Journal of Geotechnical and Geoenvironmental Engineering* **135**(10), 1404–1418.

Wichtmann, T. & Triantafyllidis, T. (2010), 'On the influence of the grain size distribution curve on P-wave velocity, constrained elastic modulus M_{max} and Poisson's ratio of quartz sands', *Soil Dynamics and Earthquake Engineering* **30**(8), 757–766.

Wichtmann, T. & Triantafyllidis, T. (2013), 'Small-strain constrained elastic modulus of clean quartz sand with various grain size distribution', *Soil Dynamics and Earthquake Engineering* **55**, 130–139.

Wong, J. K. H., Wong, S. Y. & Wong, K. Y. (2021), 'Extended model of shear modulus reduction for cohesive soils', *Acta Geotechnica* **17**, 2347–2363.

Yamashita, S., Kawaguchi, T., Nakata, Y., Mikami, T., Fujiwara, T. & Shibuya, S. (2009), 'Interpretation of international parallel test on the measurement of G_{max} using bender elements', *Soils and Foundations* **49**(4), 631–650.

Yanagisawa, E. (1983), Influence of void ratio and stress condition on the dynamic shear modulus of granular media, *in* M. Shahinpoor, ed., 'Advances in the Mechanics and the Flow of Granular Materials', Vol. 2, Trans Tech Publications, pp. 947–960.

Yang, J. & Gu, X. (2013), 'Shear stiffness of granular material at small strains: does it depend on grain size?', *Géotechnique* **63**(2), 165–179.

Yang, J. & Liu, X. (2016), 'Shear wave velocity and stiffness of sand: the role of non-plastic fines', *Géotechnique* **66**(6), 500–514.

Yang, Z. X., Li, X. S. & Yang, J. (2008), 'Quantifying and modelling fabric anisotropy of granular soils', *Géotechnique* **58**(4), 237–248.

Yimsiri, S. (2001), Pre-failure deformation characteristics of soils: Anisotropy and soil fabric, PhD thesis, University of Cambridge.

Yimsiri, S. & Soga, K. (2002), 'Application of micromechanics model to study anisotropy of soils at small strains', *Soils and Foundations* **42**(5), 15–26.

Yu, P. & Richart, F. E. (1984), 'Stress ratio effects on shear modulus of dry sands', *Journal of Geotechnical Engineering* **110**(3), 331–345.

Zeng, X. & Ni, B. (1998), 'Application of bender elements in measuring G_{max} of sand under K_0 condition', *Geotechnical Testing Journal, ASTM* **21**(3), 251–263.

Zeng, X. & Ni, B. (1999), 'Stress-induced anisotropic G_{max} of sands and its measurement', *Journal of Geotechnical and Geoenvironmental Engineering* **125**(9), 741–749.

Zhao, Y., Mahmood, N. & Coffman, R. A. (2020), 'Soil fabric and anisotropy as observed using bender elements during consolidation', *International Journal of Geomechanics* **20**(4).

Zheng, J. & Hryciw, R. D. (2015), 'Traditional soil particle sphericity, roundness and surface roughness by computational geometry', *Géotechnique* **65**(6), 494–506.

Zhou, Y. G. & Chen, Y. M. (2005), 'Influence of seismic cyclic loading history on small strain shear modulus of saturated sands', *Soil Dynamics and Earthquake Engineering* **25**(5), 341–353.

Schriftenreihe des Instituts für Grundbau, Wasserwesen und Verkehrswesen der Ruhr-Universität Bochum

Herausgeber: H.L. Jessberger

1 (1979) **Hans Ludwig Jessberger**
Grundbau und Bodenmechanik an der Ruhr-Universität Bochum

2 (1978) **Joachim Klein**
Nichtlineares Kriechen von künstlich gefrorenem Emschermergel

3 (1979) **Heinz-Joachim Gödecke**
Die Dynamische Intensivverdichtung wenig wasserdurchlässiger Böden

4 (1979) **Poul V. Lade**
Three Dimensional Stress-Strain Behaviour and Modeling of Soils

5 (1979) **Roland Pusch**
Creep of soils

6 (1979) **Norbert Diekmann**
Zeitabhängiges, nichtlineares Spannungs-Verformungsverhalten von gefrorenem Schluff unter triaxialer Belastung

7 (1979) **Rudolf Dörr**
Zeitabhängiges Setzungsverhalten von Gründungen in Schnee, Firn und Eis der Antarktis am Beispiel der deutschen Georg-von-Neumayer- und Filchner-Station

8 (1984) **Ulrich Güttler**
Beurteilung des Steifigkeits- und Nachverdichtungsverhaltens von ungebundenen Mineralstoffen

9 (1986) **Peter Jordan**
Einfluss der Belastungsfrequenz und der partiellen Entwässerungs-möglichkeiten auf die Verflüssigung von Feinsand

10 (1986) **Eugen Makowski**
Modellierung der künstlichen Bodenvereisung im grundwasserdurchströmten Untergrund mit der Methode der finiten Elemente

11 (1986) **Reinhard A. Beine**
Verdichtungswirkung der Fallmasse auf Lastausbreitung in nichtbindigem Boden bei der Dynamischen Intensivverdichtung

12 (1986) **Wolfgang Ebel**
Einfluss des Spannungspfades auf das Spannungs-Verformungsverhalten von gefrorenem Schluff im Hinblick auf die Berechnung von Gefrierschächten

13 (1987) **Uwe Stoffers**
Berechnungen und Zentrifugen-Modellversuche zur Verformungsabhängigkeit der Ausbaubeanspruchung von Tunnelausbauten in Lockergestein

14 (1988) **Gerhard Thiel**
Steifigkeit und Dämpfung von wassergesättigtem Feinsand unter Erdbebenbelastung

15 (1991) **Mahmud Thaher**
Tragverhalten von Pfahl-Platten-Gründungen im bindigen Baugrund,
Berechnungsmodelle und Zentrifugen-Modellversuche

Schriftenreihe des Instituts für Grundbau der Ruhr-Universität Bochum

Herausgeber: H.L. Jessberger

16 (1992) **Rainer Scherbeck**
Geotechnisches Verhalten mineralischer Deponieabdichtungsschichten
bei ungleichförmiger Verformungswirkung

17 (1992) **Martin M. Bizialiele**
Torsional Cyclic Loading Response of a Single Pile in Sand

18 (1993) **Michael Kotthaus**
Zum Tragverhalten von horizontal belasteten Pfahlreihen aus langen Pfählen in Sand

19 (1993) **Ulrich Mann**
Stofftransport durch mineralische Deponieabdichtungen:
Versuchsmethodik und Berechnungsverfahren

20 (1992) **Festschrift anlässlich des 60. Geburtstages von**
Prof. Dr.-Ing. H. L. Jessberger
20 Jahre Grundbau und Bodenmechanik an der Ruhr-Universität Bochum

21 (1993) **Stephan Demmert**
Analyse des Emissionsverhaltens einer Kombinationsabdichtung im Rahmen der
Risikobetrachtung von Abfalldeponien

22 (1994) **Diethard König**
Beanspruchung von Tunnel- und Schachtausbauten in kohäsionslosem Lockergestein
unter Berücksichtigung der Verformung im Boden

23 (1995) **Thomas Neteler**
Bewertungsmodell für die nutzungsbezogene Auswahl von Verfahren zur Altlastensanierung

24 (1995) **Ralph Kockel**
Scherfestigkeit von Mischabfall im Hinblick auf die Standsicherheit von Deponien

25 (1996) **Jan Laue**
Zur Setzung von Flachfundamenten auf Sand unter wiederholten Lastereignissen

26 (1996) **Gunnar Heibrock**
Zur Rissbildung durch Austrocknung in mineralischen Abdichtungsschichten
an der Basis von Deponien

27 (1996) **Thomas Siemer**
Zentrifugen-Modellversuche zur dynamischen Wechselwirkung zwischen Bauwerken
und Baugrund infolge stoßartiger Belastung

28 (1996) **Viswanadham V. S. Bhamidipati**
Geosynthetic Reinforced Mineral Sealing Layers of Landfills

29 (1997) **Frank Trappmann**
Abschätzung von technischem Risiko und Energiebedarf bei Sanierungsmaßnahmen für Altlasten

30 (1997) **André Schürmann**
Zum Erddruck auf unverankerte flexible Verbauwände

31 (1997) **Jessberger, H. L. (Herausgeber)**
Environment Geotechnics, Report of ISSMGE Technical Committee TC 5 on Environmental Geotechnics

Schriftenreihe des Instituts für Grundbau und Bodenmechanik der Ruhr-Universität Bochum

Herausgeber: Th. Triantafyllidis

32 (2000) **Triantafyllidis, Th. (Herausgeber)**
Boden unter fast zyklischer Belastung: Erfahrung und Forschungsergebnisse (Workshop)

33 (2002) **Christof Gehle**
Bruch- und Scherverhalten von Gesteinstrennflächen mit dazwischenliegenden Materialbrücken

34 (2003) **Andrzej Niemunis**
Extended hypoplastic models for soils

35 (2004) **Christiane Hof**
Über das Verpressankertragverhalten unter kalklösendem Kohlensäureangriff

36 (2004) **René Schäfer**
Einfluss der Herstellungsmethode auf das Verformungsverhalten von Schlitzwänden in weichen bindigen Böden

37 (2005) **Henning Wolf**
Zur Scherfugenbänderung granularer Materialien unter Extensionsbeanspruchung

38 (2005) **Torsten Wichtmann**
Explicit accumulation model for non-cohesive soils under cyclic loading

39 (2008) **Christoph M. Loreck**
Die Entwicklung des Frischbetondruckes bei der Herstellung von Schlitzwänden

40 (2008) **Igor Arsic**
Über die Bettung von Rohrleitungen in Flüssigböden

41 (2009) **Anna Arwanitaki**
Über das Kontaktverhalten zwischen einer Zweiphasenschlitzwand und nichtbindigen Böden

Schriftenreihe des Lehrstuhls für Grundbau, Boden- und Felsmechanik der Ruhr-Universität Bochum

Herausgeber: T. Schanz

42 (2009) **Yvonne Lins**
Hydro-Mechanical Properties of Partially Saturated Sand

43 (2010) **Tom Schanz (Herausgeber)**
Geotechnische Herausforderungen beim Umbau des Emscher-Systems
Beiträge zum RuhrGeo Tag 2010

44 (2010) **Jamal Alabdullah**
Testing Unsaturated Soil for Plane Strain Conditions: A New Double-Wall Biaxial Device

45 (2011) **Lars Röchter**
Systeme paralleler Scherbänder unter Extension im ebenen Verformungszustand

46 (2011) **Yasir Al-Badran**
Volumetric Yielding Behavior of Unsaturated Fine-Grained Soils

47 (2011) **Usque ad finem**
Selected research papers

48 (2012) **Muhammad Ibrar Khan**
Hydraulic Conductivity of Moderate and Highly Dense Expansive Clays

49 (2014) **Long Nguyen-Tuan**
Coupled Thermo-Hydro-Mechanical Analysis: Experimental and Back Analysis

50 (2014) **Tom Schanz (Herausgeber)**
Ende des Steinkohlenbergbaus im Ruhrrevier: Realität und Perspektiven für die Geotechnik
Beiträge zum RuhrGeo Tag 2014

51 (2014) **Usque ad finem**
Selected research papers

52 (2014) **Houman Soleimani Fard**
Study on the Hydro-Mechanical Behavior of Fiber Reinforced Fine Grained Soils,
with Application to the Preservation of Historical Monuments

53 (2014) **Wiebke Baille**
Hydro-Mechanical Behaviour of Clays - Significance of Mineralogy

54 (2014) **Qasim Abdulkarem Jassim Al-Obaidi**
Hydro-Mechanical Behavior of Collapsible Soils

55 (2015) **Veselin Zarev**
Model Identification for the Adaption of Numerical Simulation Models -
Application to Mechanized Shield Tunneling

56 (2015) **Meisam Goudarzy**
Micro and Macro Mechanical Assessment of Small and Intermediate Strain
Properties of Granular Material

57 (2016) **Oliver Detert**
Analyse einer selbstregulierenden interaktiven Membrangründung für Schüttkörper auf geringtragfähigen Böden

58 (2016) **Yang Yang**
Analyses of Heat Transfer and Temperature-induced Behaviour in Geotechnics

59 (2016) **Alborz Pourzargar**
Application of suction stress concept to partially saturated compacted soils

60 (2017) **Hanna Haase**
Multiscale Analysis of Clay-Polymer Composites for Geoenvironmental Applications

61 (2017) **Kavan Khaledi**
Constitutive modeling of rock salt with application to energy storage caverns

62 (2017) **Nina Silvia Müthing**
On the consolidation behaviour of fine-grained soils under cyclic loading

63 (2017) **Elham Mahmoudi**
Probabilistic analysis of a rock salt cavern with application to energy storage systems

64 (2017) **Negar Rahemi**
Evaluation of liquefaction behavior of sandy soils using critical state soil mechanics and instability concept

65 (2018) **Chenyang Zhao**
Numerical Modeling of Mechanized Tunnel Excavation:
Effects of Sub-systems and Advanced Process Simulation

66 (2018) **Tom Schanz (Herausgeber)**
Innovationen im Spezialtiefbau und in der Umweltgeotechnik
Beiträge zum RuhrGeo Tag 2018

67 (2019) **Linzhi Lang**
Hydro-Mechanical Behaviour of Bentonite-Based Materials Used for Disposal of Radioactive Wastes

68 (2019) **Usama Al-Anbaki**
Hydraulic Interaction of Soil and Nonwoven Geotextiles under Unsaturated Conditions

69 (2019) **Abhishek Rawat**
Coupled Hydro-mechanical Behavior of a Compacted Bentonite-Sand Mixture: Experimental and Numerical Investigations

Schriftenreihe des Lehrstuhls für Bodenmechanik, Grundbau und Umweltgeotechnik der Ruhr-Universität Bochum

Herausgeber: T. Wichtmann

70 (2019) **Mahmoud Qarmout**
Tunnel face stability using Kinematical Element Method (KEM)

71 (2021) **Raoul Hölter**
Optimal Experimental Design in Geotechnical Engineering

72 (2022) **Wolfgang Lieske**
Impact of polymer constitution on the hydro-mechanical behaviour of modified bentonite for the application in geotechnical and geoenvironmental engineering

73 (2022) **Patrick Staubach**
Contributions to the numerical modelling of pile installation processes and high-cyclic loading of soils

74 (2022) **Lingyun Li**
On the hydromechanical behaviour of loess and its effect on slope stability under rainfall infiltration

75 (2022) **Debdeep Sarkar**
Influence of particle characteristics on the behaviour of granular materials under static, cyclic and dynamic loading

76 (2023) **Torsten Wichtmann (Herausgeber)**
Umbau des Emscher-Systems - Geotechnische Erfahrungen
Beiträge zum RuhrGeo Tag 2023

77 (2023) **Abbas Farhat**
Fluidization and erosion of cemented granular materials. Experimental characterization and micromechanical simulation

78 (2023) **Andrea Geppetti**
Experimental and numerical investigations on the behaviour of tailing storage facilities under seismic loading

79 (2023) **Mohammad Hassan Sanayei**
Micromechanical modelling for the analysis of piping erosion in cemented soils for suction-assisted offshore foundations

80 (2024) **Christoph Schmüdderich**
Contributions to the stability assessment of slopes subjected to seismic loading

81 (2024) **Thomas Barciaga**
Constitutive modeling of natural clay with application to mechanized tunneling

82 (2024) **Cristian Rodriguez**
Contributions to the modelling of large deformations of soils: A particle-based approach

83 (2025) **Florian Christ**
Experimental investigations on the hydro-mechanical behaviour of clay shales for tunnelling relevant boundary conditions

84 (2025) **Alireza Jebeli**
On the influence of a heterogeneous pore structure on collapse behavior of sandy soils

85 (2025) **Maximilian Schoen**
Numerical analysis of tunnel excavation in swellable clay shales

86 (2025) **Qian Gu**
On the effects of grain shape, gradation, fabric and stress state on the small-strain stiffness of granular soils